Kite Farm Simulation

Assessing the impact of flight paths for multiple-unit airborne wind energy systems

Holly Johnson

Technische Universiteit Delft

TU Delft Delft University of Technology

airborne wind energy KITEPOWER

Kite Farm Simulation

Assessing the impact of flight paths for multiple-unit airborne wind energy systems

by

Holly Johnson

in partial fulfillment of the requirements for the degree of

Master of Science
in Sustainable Energy Technology

at the Delft University of Technology,
to be defended publicly on Monday August 19, 2019 at 2:30 PM.

Thesis committee:	Dr. -Ing. R. Schmehl,	TU Delft, supervisor, chair
	Dr. Ir. M. B. Zaayer,	TU Delft
	Prof. Dr. Ir. J. W. van Wingerden,	TU Delft
	Ir. P. Faggiani,	Kitepower, daily supervisor

This thesis is confidential and cannot be made public until August 19, 2021.

Abstract

As airborne wind energy is a relatively new field, much of the current research is rapidly progressing towards the development of larger commercial systems with larger airborne components. Farms of airborne wind energy systems can provide higher power generation than a single kite system and offer a potential solution to issues that single kite systems exhibit with continuous power production. As research on multiple kite systems is currently quite limited, an in depth analysis will be conducted with the use of the Kitepower single kite system simulation. Starting from Kitepower's single kite flight model, the flight path was improved from a 2D approximation to a 3D function which better represents experimentally flown paths. A kite farm simulation was then created, utilizing a unique flight path for each kite. To determine the optimal farm layout and system flight parameters, numerous simulations were conducted to maximize power output and minimize spacing between units, therefore maximizing the power density. This was done by altering the flight path parameters of each kite or by including a phase shift. The instantaneous power was also considered, and it was determined that any system without a phase shift would require storage, adding system costs and creating an intermittent power production. However, phase shifted systems showed typically lower power densities than those without a phase shift. Although the phase shifted systems typically require a greater spacing between ground units, they can operate independent of any energy input, creating a technological and economical benefit. Additionally, it was concluded that wind perpendicular systems generally produce higher power densities, and wind aligned systems often have a power density of less than half of wind perpendicular systems. Additionally, systems with similar flight envelops often performed well, but several azimuth and elevation shifts also produced good results. Compared to previous research in kite farm simulations, the results of this study concluded that closer spacing of ground stations would be possible within a reasonable factor of safety, showing promise for kite farm systems. Within the scope of the simulations from this analysis, the kite farms reached power density values similar to or larger than that of wind turbine farms, showing a great benefit over traditional wind farms. For future work, implementing a real-time farm control system would be beneficial for wind farm optimization, and essential for overall safety in implemented systems. It is assumed that with this, kite farm density can increase even further, making it more competitive with current energy generation methods, and more efficient for implementation in remote areas as well.

Acknowledgements

I'd like to thank my daily supervisor Pietro Faggiani and my academic supervisor Roland Schmehl who supported me throughout my work and helped shape the project into what it is. I'd also like to thank Mark Schelbergen who worked with me on several aspects of the project and helped me work through the existing Python scripts. I'd like to thank my peers at Kitepower for their help and many coffee breaks, which helped me power through my project. I'd also like to thank my friends and family who supported my during the time of my thesis, academically and personally, who I could rely on through thick and thin.

Holly Johnson
Delft, August 2019

Contents

List of Figures

List of Tables

List of Symbols

z	Height	[m]
r	Tether length	[m]
β	Elevation angle	[rad]
ϕ	Azimuth angle	[rad]
θ	Theta angle	[rad]
v_w	Wind speed	[m/s]
$v_{w,ref}$	Reference wind speed	[m/s]
h	Height of measured wind speed	[m]
h_{ref}	Reference height	[m]
z_0	Aerodynamic roughness	[-]
ρ_w	Air density at height h	[kg/m^3]
ρ_0	Standard atmospheric air density	[kg/m^3]
H_p	Scale height	[m]
Δt	Time step	[s]
ΔT	Non-dimensional time step	[-]
t*	Traction phase duration	[s]
r_{min}	Minimum tether length	[m]
r_{max}	Maximum tether length	[m]
v_a	Apparent wind velocity	[m/s]
v_k	Kite velocity	[m/s]
χ	Course angle	[rad]
λ	Tangential velocity factor	[-]
κ	Kinematic ratio	[-]
f	Reeling factor	[-]
L	Aerodynamic lift	[N]
D	Aerodynamic drag	[N]
F_t	Tether force	[N]
F_a	Aerodynamic force	[N]
F_g	Gravitational force	[N]
m	Mass	[kg]
S	Kite projected surface area	[m^2]
A	Kite surface area	[m^2]
C_L	Lift coefficient	[-]
C_D	Drag coefficient	[-]
C_R	Aerodynamic ratio	[-]

P_w	Dynamic air pressure	[Pa]
P	Power	[W]
ζ	Power harvesting factor	[-]
E	Energy	[J]
A_ϕ	Phi Lissajous parameter	[-]
A_θ	Theta Lissajous parameter	[-]
C	Phase shift	[t]
$d\beta$	Elevation change	[rad/s]
dϕ	Azimuth change	[rad/s]
s	Position time step	[-]
δs	Position time step change	[1/s]
δL	Distance along the Lissajous figure	[-]
$\dot{\chi}$	Turn rate	[rad/s]
G	Turn rate characteristic	[rad/s]
δ	Steering input	[m]
d	Distance between ground stations	[m]
υ_1	Half flight envelope	[rad]
N_c	Number of wind aligned columns	[-]

1

Introduction

The worldwide energy demand has been steadily increasing over the past few decades, and is expected to continue to do so in the future. The mass fossil fuel use which currently produces a significant potion of the energy supply contributes a large amount of GHG emissions and has also been linked to further environmental issues such as poor air quality or climate change [1]. After a few years of nearly constant global CO_2 emissions, in 2017 there was a 2% increase in CO_2 as well as a 2.1% growth of overall energy use [2]. As shown in Figure 1.1, European and North American energy demand is projected to decrease over time, while countries such as India and China are projected to have significant energy demand increases which greatly surpass any decrease from other countries. This is mostly expected due to growing populations and urbanization, but significant strides in energy reduction or efficiency improvements must be made to simply lower the overall demand [1].

Figure 1.1: Worldwide energy demand values [3]

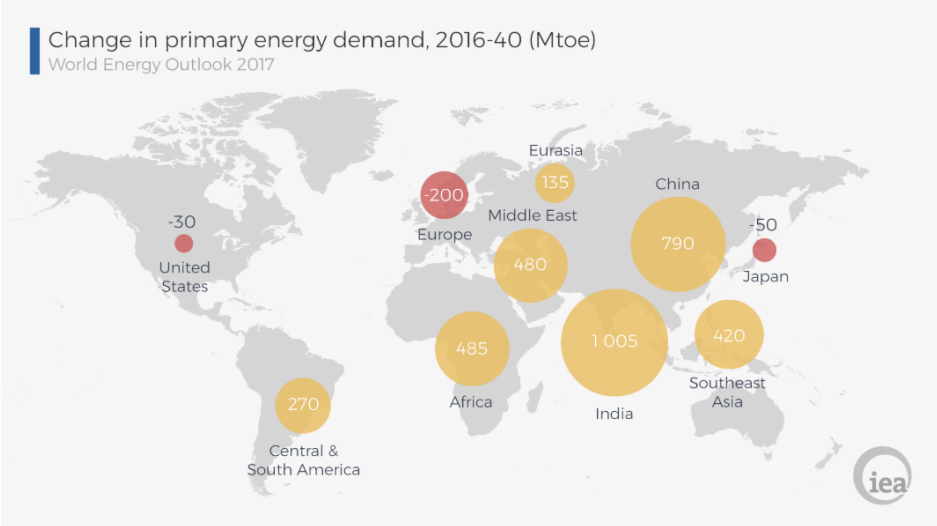

With the growing global energy demand and a heavy worldwide reliance on coal and natural gas, greenhouse gas (GHG) emissions such as $C0_2$ are on the rise. While coal use is starting to decline, natural gas and oil use is still increasing, contributing to increasingly high GHG levels. [1] Renewable energy generation methods produce less harmful emissions and are rising in efficiency and economic benefit. Wind power is currently one of the most economic renewable energy generation technologies, closely rivaled by large scale solar PV installations [4]. However, new research in Airborne Wind Energy (AWE) has proven the potential of AWE systems, with higher power production possible over smaller areas, decreased environmental impact, and increased mobility when compared to traditional wind turbines [5].

Although environmentally treaties and targets such as the Paris Agreement are being created by many highly polluting countries, the rate at which non-renewable energy is being consumed globally is not sustainable for lowering GHG emissions in the short and long term [6]. A transition towards more renewable energy generation is crucial for decreasing these emissions while still meeting the massive worldwide energy demand. Renewable energy technologies have been growing in popularity and efficiency, while the costs continue to decrease as well, and wind energy is one renewable generation option "that is in principle large enough to satisfy all of humanity's energy needs" [5].

While some renewable energy generation resources could theoretically meet the global energy demand, issues arise with specific locations which do not have ample solar or wind resources and would need imported energy. Additionally, even in sunny and windy locations, energy storage is often essential to meet energy demands when resources are not high, such as during the night time for solar energy generation. The addition of storage certainly increases costs, but also increases the capacity factor, allowing completely off-grid system operation with high enough generation and storage capacity. Wind energy specifically, with the development of large scale wind farms, has started to become more economically competitive for some locations,as shown in Figure 1.2 [4]. Figure 1.2 also illustrates the benefit of solar installations in Germany compared to conventional generation prices. This shows the increasing value of renewable energy generation, as also highlighted in [7], which suggests that renewable energy prices are becoming increasingly competitive with gas and coal energy costs in the United States as well. Additionally, [7] shows that tax incentives make these technologies particularly interesting economically, showing the lowest Levelized Cost of Energy (LCOE) values for onshore wind, solar PV, and geothermal energy, even when compared to coal and natural gas.

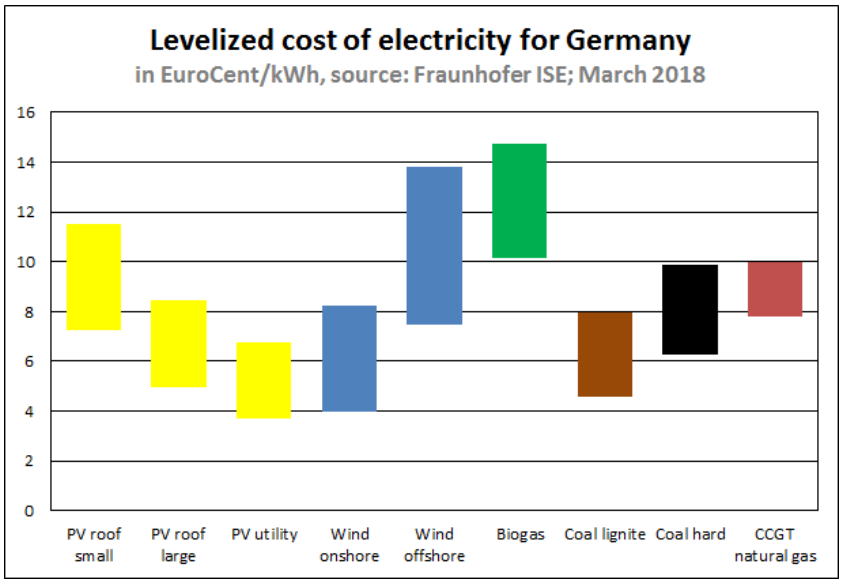

Figure 1.2: Energy Generation Methods LCOE [4]

Since wind energy is a widespread resource and has increasingly competitive costs, it is an area of great interest to myself. There is much research still to be done in the field, and there are several emerging wind energy technologies that differ from traditional wind energy generation [8]. Wind energy is conventionally focused on wind turbines, but AWE systems have started gaining momentum, as several companies and research groups have been created in the past few decades [5]. Airborne wind energy typically features a flexible or rigid airborne system attached to a tether to generate electric energy from a turbine or mechanical energy by pulling the tether. The technology is still in the research and development phase since no commercially available product is on the market yet, but test concepts have proved that AWE is a viable renewable energy generation technology. Small scale power generation has been demonstrated, even up to a rated power of 600 kW with larger scale systems such as Makani's, which can provide energy for 300 households [9]. A 600 kW system is also equivalent to a small scale (44m rotor diameter) commercial wind turbine [10].

As previously mentioned, adding energy storage to a Kitepower system would improve overall system efficiency, allowing energy use in times when the AWE unit is not deployed or generating enough

energy to meet demand. This makes AWE systems ideal for remote locations where a grid-connection would be costly to install, or when other renewable generation technology would be too difficult to transport and implement, such as traditional wind turbines. An AWE system is simple and quick to install, as it can be transported in a single shipping container and can start operation well within an hour of arrival to the generation location. This ease of mobility and setup allows for simple implementation in temporary sites for festivals or campgrounds. Wind energy is also typically ideal for locations with high wind resources and few large, physical barriers, such as in coastal areas. In regions with high grid energy pricing, AWE systems can also be quite economically competitive [11]. Turning single kite systems into a kite farm could potentially improve generation capacity, land utilization, and economics. An analysis in this area will show the potential of larger scale AWE systems, and identify how these systems operate in comparison to main stream renewable energy technology.

2

Literature Review

An extensive literature review on current AWE technology, as well as traditional wind technology and additional renewable energy technology has been conducted. The history and current research of the AWE field is detailed in the first section, with a description of the Kitepower AWE system in the following section. The final section provides an overview of the project, identifying the research questions and specific areas of interest.

2.1. History of Airborne Wind Energy

Airborne wind energy was initially conceptualized by Miles Loyd in the 1970s, where he formulated the fundamental equations for ”crosswind Kitepower” [5]. Since then, several types of AWE technologies have emerged and been studied. The main benefits of the technology are low material costs and ease of setup, especially when compared to traditional wind turbine technology. This is mainly due to fewer required components and the ability to reach higher altitudes than with traditional wind turbines. However, AWE systems are still relatively new with limited implemented concepts, so there is still ample room for research and development. Single AWE units are nearing commercial availability, and one unit has been implemented in Alaska, but kite systems have not received as much attention as traditional wind turbines yet, providing an opportunity for further research [12]. Some research has already yielded results of the economic benefit of kite farms compared to single kites. In [13] it was calculated that a kite farm could decrease the LCOE from €106/MWh for a single 250 m^2 kite to €96/MWh as an effect of scaling up. Another publication suggests AWE costs of €100 - €150/MWh to be possible for single kite systems with a wing area of approximately 200 m^2 [14]. Ampyx Power is currently working on the design of a 2 MW off-shore rigid wing aircraft farm, with LCOE estimates around €137/MWh [15]. However, it was also suggested that economic improvements up to €70/MWh could also be made after 2023 in the European market due to future research [16]. Additionally, current kite systems typically operate with kites much smaller than 200 m^2, but with advancements, kite systems of these size are theoretically possible. The difference between these LCOE estimates show that each kite farm system is affected by the selected components and system type. For example, the offshore system requires costly floating bases, which consume about half of the system costs [15]. Implementing a similar system onshore may yield a lower power output due to reduced wind energy, but would significantly cut installation costs. These effects will be analyzed in the system optimization, providing a sensitivity analysis on the effect of component costs. However, the main Kitepower system will still be used as the basis of the wind farm analysis, since experimental data is available for validation.

With the current industry, there are two main types of AWE systems that are utilized: on-board generation and ground-based generation. The on-board generation systems have a turbine and motor on the airborne component, which instantaneously generate energy and transmit it through the tether, which must conduct electricity well while also providing appropriate material strength in tension. The airborne component either is stationary or flying in an optimized path to provide high speed wind to the turbine at high altitudes. Since the moving airborne components can fly at high rotational speeds, a gearbox can be omitted on the airborne component, decreasing the drag. The negative side of this generation mode is the increased drag from the on-board turbine, which is why Loyd termed this

generation type as ”drag mode” [5]. The alternative generation mode utilizes the mechanical pull of the airborne component, connected via tether, to power a motor on the ground. This system operates in reel in and reel out cycles which consume and generate power, respectively. For this reason, this mode is also referred to as pumping mode. However, the reel out phase generates much more power than is required for the reel in phase, allowing a net positive generation. These ground based generation systems often fly in crosswind patterns to maximize apparent wind velocity, or the wind speed felt at the kite [17]. Additionally, some AWE systems do not implement cross-wind flight motions, but simply reel in and out at a constant angle with respect to the ground. These systems require less complex control and are generally simpler. Another unique AWE concept is the lighter than air system which stays afloat by utilizing a low density gas such as Helium in an inflated airborne structure. The airborne component can either rotate to generate energy, or utilize a stationary turbine, such as with the implemented concept in Alaska. The rotating system is controlled by its rotational velocity, utilizing the Magnus effect to increase lift and pull the tether outwards to generate mechanical energy. These systems do, however, have a relatively large weight, making it quite difficult to fly in crosswind patterns [5]. These systems also must also be quite large in order to generate power outputs similar to that of a winged system. Omnidea’s rotating lighter than air system is shown below in Figure 2.1.

Figure 2.1: Lighter than air system [18]

Another important design choice is the selection of a flexible or rigid wing system. Rigid wing systems can produce more lift and therefore more power. Consequentially, they also produce larger tether forces and need stronger or thicker tethers, which can increase weight or drag [5]. Flexible or ”soft” kites produce lower lift and tether forces, and therefore lower power, but they are lightweight and less costly. Flexible kites are also more likely to survive a crash with less damage than a rigid wing. Since tether strength can often be a limiting factor in AWE system design, the kite type is an important consideration. High tether tension, resulting from high wind speeds, results in decreased energy production since the airborne component must be depowered, as can be seen in Figure 2.2, which was derived for a 100 m^2 flexible wing kite [13]. Unlike wind turbines which produce a constant power after the rated wind speed, AWE systems should be designed specifically for each location with the average wind speeds taken into consideration.

Since the weight and area of the tether affect the drag as the airborne system flies through the air, it is ideal to minimize the tether mass and diameter. Additionally, having less of the tether reeled out, or flying at a lower height, decreases the amount the tether in use, and therefore decreases the tether mass and drag. Consequently, this also limits the airborne component height, restricting it to lower wind speeds. Additionally, with on-board generation systems, tether conductivity must be considered when selecting a material, which often decreases the overall material strength [5]. One concept to minimize the effects of tether drag is a multiple wing system, where several kites use the same main tether but branch off to provide some distance for each kite to operate. This concept requires precise kite control to avoid kite collisions, especially during takeoff and landing, and therefore is not currently a popular type of AWE system [5].

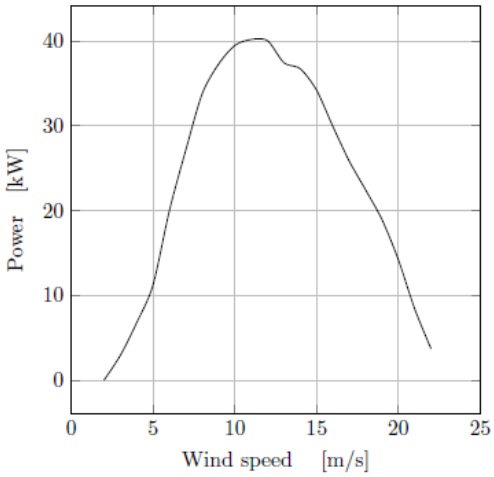

Figure 2.2: Kite system power curve [13]

Concepts for vehicle propulsion from airborne components were also once utilized, but these devices proved difficult to control manually, so they did not grow greatly in popularity. Similarly, a few ship propulsion systems were created from the addition of a kite, with the intention of lowering the necessity of fuel for propulsion. Nowadays, the largest commercial AWE system is designed to assist with shipping vessels, and a traction power of 2 MW has been reported from a single kite system from SkySails. This system solely produces electricity for the ship, but a large potential market exists for ship propulsion with kites as well [5].

Most modern flexible wing AWE systems, such as Kitepower's, operate in three phases: traction, transition, and retraction, which are illustrated in Figure 2.3. The main power generation occurs during traction, or reel-out, where the airborne component typically flies in a figure-eight pattern (not shown in Figure 2.3) from the minimum tether length to the maximum length at a near constant elevation angle. The tether is under great tension from high speed cross-wind kite flight, which results from a high lift to drag ratio. Once the tether is reeled out to the maximum length, the fully powered kite is then depowered, decreasing the lift and allowing the retraction phase, or reel in phase, to start. During retraction, the kite flies in the opposite direction as it does in traction. It flies towards zenith with an increasing elevation angle, and the ground based system quickly reels in the tether as it flies closer towards the ground station. This phase requires significantly less energy than is generated in traction, so there is a net positive energy generation. Once the minimum tether length is approximately reached at the end of the traction phase, the transition phase is then utilized to maintain a nearly constant tether length and to return the kite to the traction elevation angle. The kite is again fully powered in the transition phase, and traction starts again once the correct elevation angle is reached [5].

AWE systems are flown at altitudes that are typically much higher than the hub heights of traditional wind turbines, allowing for generally higher wind speeds. Larger wind turbines have hub heights reaching almost 200 meters, while AWE systems fly several hundred meters high, up to heights around 1 km [20]. Figure 2.4 shows an AWE system in use in contrast to traditional wind turbines and it is clearly seen that AWE systems utilize a higher altitude. The typical figure-eight flight path during energy generation can also be seen with this long-exposure capture. However, since AWE systems are not as thoroughly developed, the efficiency evaluation metrics must be altered to appropriately match the technology. AWE systems have a much larger swept airspace, so the effective power production and wake effects are calculated in a significantly different way. In several past analyses, kite wakes were assumed negligible due to the large swept airspace, however further analysis should be conducted to confirm this [13] [21].

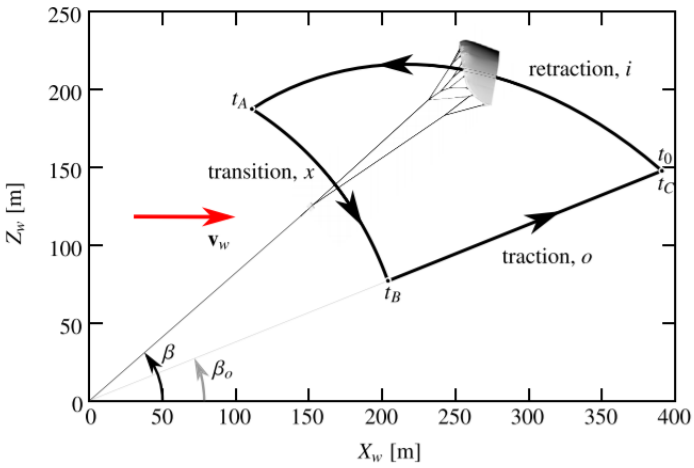

Figure 2.3: Airborne Wind Energy phases [19]

Figure 2.4: Airborne Wind Energy System [18]

2.2. The Kitepower System

Since 2016 Kitepower has been developing and testing flexible kite systems, aiming towards utilizing larger kite systems. Kitepower emerged from the TU Delft AWE systems research group, which also continues to study AWE topics such as kite modeling and control. Kitepower's current system utilizes a flexible, leading-edge inflatable (LEI) kite, which is typically used by kite surfers, making it widely commercially available. The tether is made of Dyneema, a high strength yet flexible material, which allows the system to withstand high forces from high wind speeds. A ground-based generation unit is used, with a peak power of 180 kW, and a nominal power of 100 kW. The system features an airborne Kite Control Unit (KCU) which dictates the flight path as a function of pre-defined guidance inputs or measured data, such as wind speed, tether tension, or tether length. The kite can fly in an altitude range of 70-450 km and has an yearly power output of 450 MWh [22]. The entire system during operation is illustrated in Figure 2.5.

Figure 2.5: Kitepower flexible wing system [18]

Kitepower has previously developed a module to simulate the 2D flight path of a selected kite with reasonable accuracy. This idealized flight path represents the kite path over time in all phases, but the figure-eight movements in the traction phase are omitted for simplicity. A GUI allows several system and operational parameters to be changed easily, such as kite area or maximum tether length, providing a quick simulated flight path over time for any flexible wing system. This code is used as the base of the module which was modified to include the figure-eight traction motion to allow for a more accurate flight path, and therefore kite farm analysis.

Currently an experimental single kite system has been developed and tested, but in the future, a kite farm is of interest, as it can produce more power and potentially provide a more consistent level of power, which is better for a grid connected system. A kite farm could act in the same way as a wind turbine farm, potentially providing energy to a grid as a medium to large-scale power plant. Additionally, small scale kite farms could be used locally, providing energy to homes or to temporary and remote areas. It is also expected that the economics of larger farm systems will improve as a factor or scaling up.

There is currently little research on kite farms, since AWE is still a growing field, and few AWE systems are actually implemented. Many companies are still in the development phases with single kite systems, but AMPYX power, in collaboration with several other companies, has been conducting research on a floating AWE concept with a rigid wing system. The 'Sea-Air-Farm' project has proven to be highly possible and economically competitive, and could provide MW scale energy production [23]. Similarly, Makani Technologies has proposed an offshore AWE farm in northern Europe, showing promise and interest in developing AWE farm technologies [24]. While these systems are focused on rigid wing systems for larger scale energy production, flexible wing system farms offer opportunities for a smaller scale, more flexible market. Additional research and testing for kite farms would advance the possibilities of AWE systems, making them a larger player in the energy market.

2.3. Project Outline

At Kitepower there was one previous thesis on kite farm configuration and optimization, which will be used as the basis for this thesis. This thesis by Faggiani, [13], performed an evaluation of electrical and mechanical components of the system as well an analysis of the kite farm spacing, but the aim of this thesis is to focus mainly upon improving the simulated single kite flight path and evaluating the optimal spacing for a kite farm with varying operational parameters. In [13], the idealized 2D flight path (as described in the section 2.2) was utilized, but the inclusion of the figure-eight motion in the traction phase of the flight path will yield a more accurate analysis for spacing of a kite farm. This cross-wind motion could result in a crash between kites or entanglement of tethers if not accounted for, which would cause safety risks and high repair costs. In the previous thesis, it is assumed that each kite's operational flight envelope, or the space in which the kite flies during operation, could not overlap, which could result in larger kite spacing distances than actually required. In this analysis, the operational envelopes and additional operational parameters will be modified and evaluated to analyze the risk of collision with decreased spacing between kites in addition to the impact on power production and farm power density. Decreasing the spacing between kites will increase the power density, but will also increase the risk of collision, so an in-depth analysis is required to further evaluate the benefit of

a kite farm system over a single kite system.

The results of this project will be utilized to evaluate the potential technical and economic viability of kite farm system in future research at Kitepower. A kite farm with a high power density and low LCOE would provide incentive for additional research and development in this area. Since single kite AWE systems produce relatively low power when compared to a single wind turbine, a kite farm would be suitable for larger scale energy production, especially if it is more economically beneficial.

The main research question, with two sub-questions, is:

What effect does a kite's flight path have on a kite farm system's power production?

- How does the addition of the figure-eight traction path impact model accuracy when compared to the 2D idealized flight path?
- How do shifted flight paths impact the required spacing between ground station units, average power production, and power levelization?

For this analysis, the modified 3D flight path will be developed based upon the 2D model in Chapter 4, which will then be utilized as an input for the kite farm module. This path will be verified with experimental data and evaluated for accuracy. It is expected that the updated flight path will also improve modeling accuracy, mainly because there is additional spatial resolution, and the flight path model should be similar to a typical experimentally flown path. Once a suitable path is developed, a new module will be developed to utilize the simulated path for several kite systems, as described in Chapter 5. Each kite will utilize the same flight path module to create a unique path from its ground station point that will potentially feature phase shifts (where the kites operate asynchronously) or staggered operational envelopes. Initially, a two kite system will be modeled, followed by a three kite triangular layout. A case study on both system types will be conducted to evaluate the effects of all input parameters individually, and then to find the optimal system configuration of each. Since the orientation of the wind strongly effects the minimum spacing requirements, the worst and best case scenarios will be utilized to see the upper and lower performance limits. The worst case scenario corresponds to a system of kites which are all aligned with the wind direction (wind aligned), whereas the best case scenario features kites in a row that are all perpendicular to the wind direction (wind perpendicular). A high probability of non-collision is required for a kite system, as it will ensure safety and optimal operation. Secondary to the system's safe operation is the power generation and stabilization. One benefit of a kite farm over a single kite is the ability to stabilize power output if kites are operated with a phase shift. This is a significant benefit if the system is to be connected to a grid, since it will produce a more stable output, as typical utility scale generation methods do. It is also important in decreasing the need for storage, since an individual kite system will need a battery to operate, as it requires power during the retraction phase. With a kite farm, this energy can be directly supplied from other kites which are producing power in the traction phase. This will be addressed in each case, in Chapters 6 and 7, and will serve as a starting point for future system development and optimization.

3

AWE Theory and Modeling Methods

The theory and methods utilized in this analysis are outlined throughout this chapter. Methods from [13] were applied and modified for the current model. This analysis uses a quasi-steady model, so it is assumed that at each time step there is a force equilibrium at the kite. A single point mass is used to represent all airborne mass. The mass of the kite, airborne components, and tether are taken into consideration, as well as the lift and drag coefficients of the kite and tether. In this analysis, a straight, inelastic tether is also assumed and the effects of inertia are neglected. Accounting for tether sag and/or inertia in the simulation would increase computational complexity significantly, and it was deemed sufficient for this analysis to use ideal assumptions, since they would produce reasonable results. In the first section, the reference coordinate system is outlined, which is followed by two sections which provide an in depth description of the methods and equations used to develop the kite path model. The second section identifies the basic, relevant AWE equations, while the third section addresses how the equations are implemented in the computational model.

3.1. Reference coordinate systems

The reference coordinate system, as typically used for AWE systems, is shown in Figure 3.1, which represents the kite path in both spherical and Cartesian coordinates. The kite position is located at the end of the radial vector, r, in the figure, which is defined by the polar coordinates (r,θ,ϕ). The tether is ideally approximated by the radial distance, but does not show any sag which might be present in reality,and would therefore increase the tether length. Here the angles θ and ϕ represent the polar and azimuth angles, respectively. Not shown in the illustration is the visualization of the elevation angle, β, which is the complementary angle of θ, or the angle which the tether makes with respect to the ground. The positive z axis is also referred to as zenith, as it is an angle which points directly upwards, and is sometimes the target set point during the retraction phase. With this orientation, the wind velocity is parallel to the x-axis, going from the origin towards the positive x-axis. As also seen in Figure 3.1, the aerodynamic force, F_a, is in line with the radial vector and is the result of the addition of the lift and drag force vectors, L and D [5]. The apparent wind speed vector, v_a, is parallel to the drag vector by definition and consists of a radial and tangential component. The tangential direction, denoted by τ, is perpendicular to the radial direction.

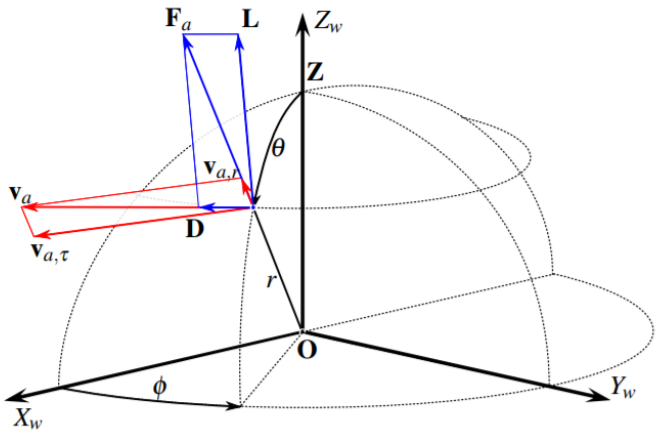

Figure 3.1: Reference coordinate system [19]

Polar coordinates are predominantly used since many AWE calculations are based in polar coordinates. However, when needed, the Cartesian coordinates derived as shown below.

$$x = r\cos(\beta)\cos(\phi) \tag{3.1}$$
$$y = r\cos(\beta)\sin(\phi) \tag{3.2}$$
$$z = r\sin(\beta) \tag{3.3}$$

For the layout of the kite farm, a different type of coordinate system is utilized. A 2D configuration is used to specify the base points of each kite, simplifying the analysis. For this Cartesian coordinate system, the rows of kites lay along the x-axis, and columns of kites lay along the y-axis. This is illustrated below in Figure 3.2. Each kite then has its own 3D coordinate system to define the kite flight path, which is tied into one global 3D coordinate system to evaluate for collisions.

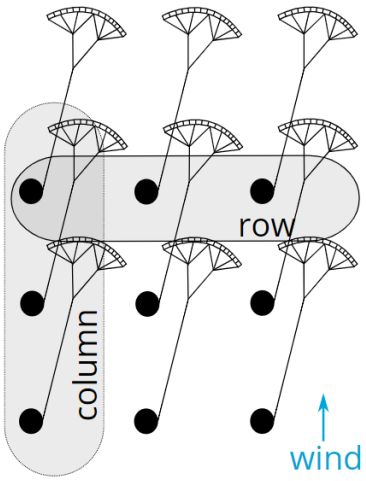

Figure 3.2: Kite farm layout [25]

3.2. Mathematical background

Keeping in line with the mathematical methods of [13], a single kite quasi-steady flight simulation model was utilized and developed as described below.

The environmental conditions were modeled with the methods of [26] and [19] for wind speed and air density calculations respectively. Here, as with previous analyses, the Log Law, Equations 3.4, is

utilized since it can extrapolate wind speeds fairly accurately within 200 meters of altitude, which is the typical height range for the current Kitepower system [13]. This allows for a maximum tether length of 400 meters with an elevation angle of 30°, which is a reasonable operating condition for the Kitepower system. At higher altitudes, the Power law is sometimes a better approximation, but the wind speed data derived from the Log law has been compared to historical wind data at the test location, and confirmed to be an accurate representation of the wind speed. In future experiments it would be highly beneficial to have experimental wind speed data at the kite height throughout operation, as it would improve simulation verification. But, this is difficult to implement in reality, so the Log Law is used as an acceptable approximation. Since the kite is almost constantly changing altitude, it is important to update the wind speed with reasonable accuracy to calculate additional variables of the system. The air density is utilized in aerodynamic calculations, and can be utilized to find the air pressure at the same height. Equation 3.5 shows the method used to calculate this value.

$$v_w(h) = v_{w,ref}\frac{\ln(\frac{h}{z_0})}{\ln(\frac{h_{ref}}{z_0})} \tag{3.4}$$

$$\rho_w(h) = \rho_0^{\frac{-h}{Hp}} \tag{3.5}$$

where v_w is the wind speed, $v_{w,ref}$ is the wind speed at the reference height, h is the height of the kite, h_{ref} is the reference height where wind speed measurements are taken, z_0 is the aerodynamic roughness (dependent upon the environment), ρ_w is the air density at the height h, ρ_0 is the standard atmospheric air density, and H_p is the scale height for density. A constant reference wind speed is assumed since once complete cycle takes less than a few minutes, and it is not expected for the wind to change significantly over time. The wind speed at the kite is, however, updated at each time step to account for any change in wind speed that occurs with a change in kite altitude.

The time step utilized in the flight path simulation, Δt, is calculated from the non-dimensional time step, ΔT, and the traction phase time, t^* [19]. The non-dimensional time step is selected as a constant value, which is 0.1 seconds for this analysis.

$$\Delta t = \Delta T t^* \tag{3.6}$$

$$t^* = \frac{(r_{max} - r_{min})}{v_{w,ref}} \tag{3.7}$$

where r_{max} and r_{min} the maximum and minimum tether reel out lengths. With Kitepower's 25 m^2 kite system , the minimum and maximum tether lengths are typically 200 and 400 meters, respectively. Additionally, the reference wind speed is measured at 6 meters high for this analysis.

An in depth summary of all the utilized calculations can be seen in [19], deriving the apparent wind velocity equation, the total drag (including tether drag), the normalized tether force, and eventually the power output of the kite system. This derivation starts from a basic AWE equation for the apparent wind speed, which describes the wind speed felt at the kite itself. Equation 3.8 shows this relationship, which can also be broken down into its polar coordinates in the radial, elevation angle, and azimuth angle directions as described in [13] and shown in the equations below. The kite speed is represented as v_k, and consists of a radial and tangential component ($v_{k,r}$ and $v_{k,\tau}$). This speed can be measured directly from kite sensors during testing. The course angle, χ, represents the orientation of the kite.

$$v_a = v_w - v_k \tag{3.8}$$

$$v_{a,r} = v_w \sin\theta\cos\phi - v_{k,r} \tag{3.9}$$

$$v_{a,\theta} = v_w \cos\theta\cos\phi - v_{k,\tau}\cos\chi \tag{3.10}$$

$$v_{a,\phi} = -v_w \sin\phi - v_{k,\tau}\sin\chi \tag{3.11}$$

Several dimensionless ratios exists to more simply characterize AWE flight equations. The tangential velocity factor, λ, is defined in Equation 3.12. This ratio shows the relation of the tangential kite speed to the wind velocity, highlighting how quickly the kite is flying compared to the ambient wind speed

[19]. Similarly, the kinematic ratio, κ, is defined as the ratio of the tangential apparent velocity to the radial apparent velocity. This indicates a greater kite speed in either the radial or tangential direction. Another significant ratio is the reeling factor, f, calculated as shown in Equation 3.14, which indicates how quickly the tether is being reeled inwards or outwards. A positive value indicates that the kite is in the traction phase, while a negative value represents retraction. Ideally, the reeling factor is 0 during the transition phase, but this is sometimes not the case if the tether force grows to be too high, and the tether must then be reeled out slightly to lessen the tether force. These ratios define important characteristics of kite flight at each time step, and give insight into the direction, speed, and phase throughout the cycle.

$$\lambda = \frac{v_{k,\tau}}{v_w} \tag{3.12}$$

$$\kappa = \frac{v_{a,\tau}}{v_{a,r}} \tag{3.13}$$

$$f = \frac{v_{k,r}}{v_w} \tag{3.14}$$

Equations 3.9-3.11 can be rearranged as shown below to include the reeling speed and tangential velocity factor [13].

$$v_{a,r} = (\sin(\theta)\cos(\phi) - f)v_w \tag{3.15}$$

$$v_{a,\theta} = (\cos(\theta)\cos(\phi) - \lambda\cos(\chi))v_w \tag{3.16}$$

$$v_{a,\phi} = (-\sin(\phi) - \lambda\sin(\chi))v_w \tag{3.17}$$

The magnitude of the apparent wind vector can be calculated from the radial and tangential components as shown below. Using geometrically similar triangles from Figure 3.1, it can be derived that the lift to drag ratio, L/D, is similar to the tangential apparent velocity over the radial tangential velocity, as described in Equation 3.19. This is also equal to the kinematic ratio. However, this only holds true if mass is neglected in the analysis, since a gravitational force vector will alter the direction of the apparent force vector [5]. The dimensionless apparent wind speed, also for mass-less analyses, can then be calculated with Equation 3.20, by combining the previous two equations and also substituting in Equation 3.15.

$$v_a = \sqrt{v_{a,r}^2 + v_{a,\tau}^2} \tag{3.18}$$

$$\frac{v_{a,\tau}}{v_{a,r}} = \frac{L}{D} \tag{3.19}$$

$$\frac{v_a}{v_w} = (\sin\theta\cos\phi - f)\sqrt{1 + \left(\frac{L}{D}\right)^2} \tag{3.20}$$

Similarly, using the dimensionless ratios and equation substitutions as described in [5], the tangential velocity factor can be updated as seen in Equation 3.21. This new equation is based on the variables a and b defined below, which utilize the apparent wind velocity components and the tangential velocity ratio equation.

$$\lambda = a + \sqrt{a^2 + b^2 - 1 + \left(\frac{L}{D}\right)^2 (b - f)^2} \tag{3.21}$$

$$a = \cos(\theta)\cos(\phi)\cos(\chi) - \sin(\phi)\sin(\chi) \tag{3.22}$$

$$b = \sin(\theta)\cos(\phi) \tag{3.23}$$

To ultimately calculate the power produced by the kite system, a force balance is required at each time step after parameters such as kite position and velocity are updated. The main forces acting at

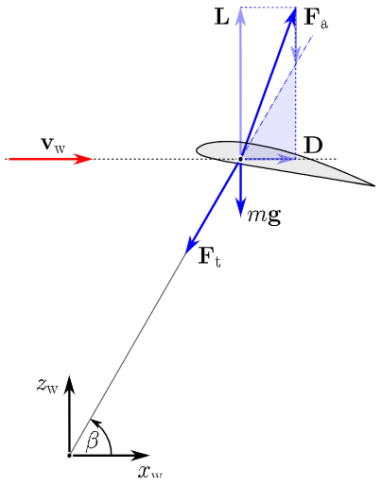

Figure 3.3: Forces acting on the kite [25]

the kite are the aerodynamic force, the tether force (F_t), and gravity (F_g or mg) as illustrated in Figure 3.3 which shows a side view of a kite system, where the kite is represented as an airfoil.

From the above figure, a force balance can be calculated as shown below. At all time steps throughout the analysis, it can be assumed that all forces sum to zero. In future work, inertial forces could be included to further increase the model's accuracy, but they are omitted in this work since the angular velocities during turning maneuvers are relatively small [19]. In this force balance, the aerodynamic and gravitational forces can be calculated, and therefore the tether force can also be solved for.

$$\sum F = F_a + F_g + F_t = 0 \tag{3.24}$$

A force balance on the tether is shown in Figure 3.4. It can be seen that the tether weight is accounted for in the center of the tether to account for the mass along the entire tether. Additionally, it is shown that the tether is not completely in the radial direction, represented by the dashed line, but meets at the same end points as a linear tether approximation would. Additionally, the tether force at the kite, F_t, and at the ground station, $F_{t,g}$, are illustrated. These two forces follow the curvature of the tether, and are not completely in line with the radial direction because gravitational forces are accounted for. To account for the non-radial tether vector, the gravitational and tether fore vectors are shifted to align the tether vector completely in the radial direction. This is done by adding the gravitational force from the tether to the kite gravitational force, which shifts the gravitational vector to not only act in the downwards direction, but also slightly towards the ground station, in the negative x direction. This simplifies calculations and allows the tether to be treated as completely straight.

As previously mentioned, the lift and drag vectors can be summed to calculate the aerodynamic force vector. These vectors are calculated as shown below where C_L and C_D are the lift and drag coefficients, respectively, and S represents the kite's projected surface area. Here, the tether drag is accounted for in the total drag coefficient, using the methods of [19]. The equations can become variables of the dynamic air pressure, P_w, instead of air density by substituting Equation 3.27 into the lift and drag equations, since air pressure can be measured directly during flight tests [27].

$$L = \frac{1}{2}\rho_w S C_L v_a^2 \tag{3.25}$$

$$D = \frac{1}{2}\rho_w S C_D v_a^2 \tag{3.26}$$

$$P_w = \frac{1}{2}\rho_w v_w^2 \tag{3.27}$$

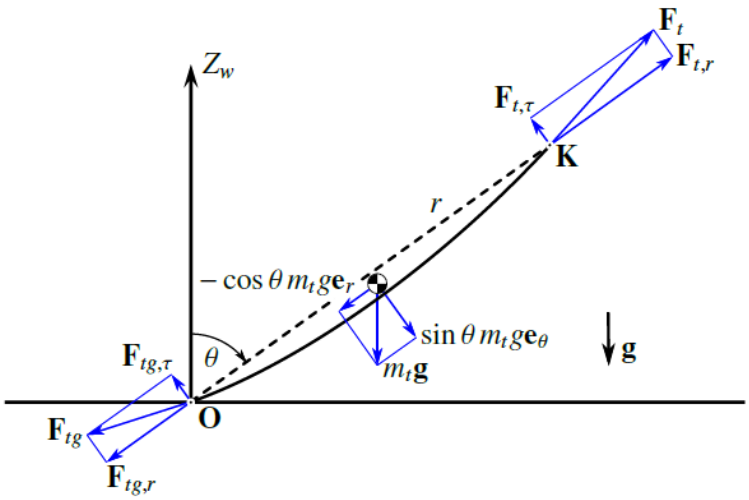

Figure 3.4: Forces acting on the tether [19]

The aerodynamic force can be calculated from the lift and drag vectors, along with Equation 3.20, to produce Equation 3.28. The resultant coefficient, C_R, is calculated from the kite lift and drag coefficients as seen below.

$$F_a = P_w S C_R (1 + \kappa^2)(\sin\theta\cos\phi - f)^2 \tag{3.28}$$

$$C_R = \sqrt{C_L^2 + C_{D,total}^2} \tag{3.29}$$

The gravitational force vector can be represented as shown by the equations below. Since the force acts entirely in the downward direction, there is no magnitude in the phi direction. Figure 3.3 shows the force balance for a single operating kite which accounts for mass. This involves the inclusion of a gravitational force vector which is not present in Figure 3.1. It can be seen that the accounting for the mass of the system shifts the aerodynamic force vector upwards to account for the weight of the system. The aerodynamic force vector is, therefore, no longer parallel to the tether force vector. In the equations below, the mass of the airborne tether, m_t, is accounted for fully in the radial direction and only partially in the theta direction, as described in [13].

$$F_{g,r} = -(m + m_t) g \cos\theta \tag{3.30}$$

$$F_{g,\theta} = (m + \frac{m_t}{2}) g \sin\theta \tag{3.31}$$

Substituting in the calculated force values into Equation 3.24, allows the tether force to be calculated. The maximum tether force, determined by its material properties, can limit the performance of the system. Since there can only be so much tension in the tether before it breaks, the lift of the kite must be monitored and controlled to maintain a reasonable aerodynamic force which will not increase the tether force too significantly. High winds and lift can lead to high tether forces, which could snap the tether if the kite is not depowered, or if lift is not decreased by lowering the angle of attack. However, unless the wind speeds are significantly high, this is typically not an issue of great importance, and the proceeding calculations have no restrictions [5]. When accounting for mass effects, the lift to drag ratio can be calculated as shown in Equation 3.32. The lift to drag ratio can also be referred to as the glide ratio, G. This equation can be used to iteratively calculate the kinematic ratio, which is not yet calculated at this point, but is needed for the aerodynamic force calculation. If mass is neglected, the kinematic ratio can be represented simply as the lift to drag ratio, but while including mass effects, Equation 3.32 should be utilized instead. Mass is included in this analysis since it has been proven in previous analyses that accounting for mass provides a better flight path simulation and does not significantly increase computational time [19].

$$\frac{L}{D} = \sqrt{\left(\frac{F_a v_a}{\mathrm{F_a v_a}}\right)^2 - 1} \tag{3.32}$$

With a known κ value, the aerodynamic force can be calculated. The gravitational force vector can be calculated from the kite's position and current airborne mass. The position and velocity vectors are updated at each time step, which ultimately allows the tether force to be calculated as well. Finally, the power of a single kite system is calculated as shown. [5]

$$P = F_t f v_w \tag{3.33}$$

Another evaluation metric for AWE systems is the power harvesting factor, which represents the power harvested from wind by the AWE system. It is defined with Equation 3.34, which is the ratio of the generated system power, P, to the wind power of a similar area, P_w. The wind power is defined as seen below. This metric allows AWE generation to be more easily compared between different AWE system types. The harvesting factor allows for a simple comparison to wind turbine generation by multiplying the power harvesting factor with the Betz limit. This compares the required area for the different generation types which would yield the same power, so it is useful to compare the power densities [5].

$$\zeta = \frac{P}{P_w} \tag{3.34}$$

$$P_w = \frac{1}{2}\rho A v_w^3 \tag{3.35}$$

The energy generation or utilization is calculated from the product of power and time as shown below. The time is updated with the previously described time step, and the results are checked at each time step to ensure they are within operational limits, or if the next phase should be started.

$$E = P\Delta t \tag{3.36}$$

3.3. Computational implementation

In the single kite flight path simulation, the equations from the previous section are implemented, along with position and velocity updates for each time step. Initially, the simulated path begins with the retraction phase, and runs through the transition and traction phases to model one complete cycle. Initial values are specified to set the operational and system parameters which dictate the flight path such as the kite area, traction force, retraction force, lift/drag coefficients, and several other variables. These simulated variables do, however, slightly differ from the parameters of flight tests, since the path simulation module utilizes a different path planning method than with the real-time flight controller of experimental flight, but they can be modified to better match experimental paths. The retraction and traction force values are defined as F_{in} and F_{out} and specify the optimal tether force during retraction and traction, respectively. With too little tether force, typically during retraction, there will be a large amount of tether sag, which could lead to entanglement issues. As previously described, if the tether force is too large, there is a risk of the tether breaking, which could cause safety issues as well as system damage. The kite area, A_{kite}, is the total surface area of the kite, and the initial polar coordinates at the beginning of the retraction phase are defined by r_{min}, β_0, ϕ_0, which also serve as input variables to the flight path simulation. In this simulation, the ground station is not represented due to time constraints, but it is assumed that the system components can be selected to meet the reeling speed requirements as determined by the simulation. If this is not the case, there may be performance compromises to lower production costs or simplify component production. However, with no ground station in the simulation, there are no limits on the change in reeling speed, as there would be with a motor or generator. This leads to some inaccuracies in the transition phase simulation, causing a high change in reeling speed, which provides a large change in instantaneous power, as is seen in the results of the case study and will be discussed later.

Based on the input variables, calculations are made to initialize all variables at the kite's starting position. For each time step, all variables are updated, including position and velocity updates. First the

wind speed is interpolated at the kite's height, and additional environmental variables are calculated such as air density and air pressure at kite height. The initial kite position is defined by the maximum tether length, as well as the initial elevation and azimuth angles, β_0 and ϕ_0 respectively. The course angle is more relevant in traction calculations, since the other phases are assumed to have constant course angles. The traction course angles are used to assess the accuracy of the simulated path when compared to experimental data, since the simulated path should not have the kite turning more quickly than it physically can.

A unique function of the flight path module is run for each phase, indicating the target position which should be met before the next phase is started. The simulation starts with the retraction phase, which ends when the minimum tether length is reached. The transition phase is completed when the set elevation angle is achieved, and traction ends when the maximum tether length is reached. At the end of the traction phase, or after one complete cycle, the total generated power is calculated. The traction and transition phases from the previously created code was kept the same, since the focus is on increasing fidelity in the traction phase.

For all phases, the set tether force requirement, F_t, is utilized to initially calculate values iteratively until the flight characteristics are represented well for each time step. The tether force in the elevation and azimuth angle directions is 0 because the tether force has been adjusted to only provide a force in the radial direction, as described in the previous section. The Kitepower system is based on an ideally constant tether force for each phase, which produces a more consistent power output, and this vector at the kite is actually negative because the direction of the tether force is in the negative x- and z- directions, as illustrated in Figure 3.3. Using this set tether force assumes no gravitational effects at first, approximating the tether force as equivalent to the aerodynamic force, and the glide ratio as equivalent to the kinematic ratio. Since mass should ultimately be accounted for, these are taken as starting points for an iteration of the kinematic ratio until the glide ratio reaches the ratio of the defined lift and drag coefficients. When the calculated kinematic ratio produces a glide ratio similar to the ideal value, this is taken as the final kinematic ratio, and utilized to calculate additional parameters.

With the tether force defined as the specified maximum or minimum tether force, for traction or retraction, the reeling factor is also initially approximated with Equation 3.37. This equation is derived by first neglecting the effects of gravity, and therefore assuming the tether force magnitude to be equal to that of the aerodynamic force. The lift to drag ratio can then also be assumed to be equivalent to the kinematic ratio, so these values are also substituted in. Equation 3.28 is then rearranged to yield Equation 3.37. The reeling factor is updated with every iteration.

$$f = \cos(\beta)\cos(\phi) - \sqrt{\frac{F_t}{P_w S C_R (1 + \left(\frac{L}{D}\right)^2)}} \tag{3.37}$$

If no pre-defined tether force is specified, the reeling factor is set to 0, so the tether length should be constant as with the transition phase. Again, the tether force at the kite in the theta and phi directions is assumed to be 0 since the initial, approximated tether force acts just in the radial direction. The required tether force at the kite is then calculated as shown below for each iteration. Reeling during the transition phase should only occur if the tether force is too high or low. Otherwise, the main goal is to efficiently decrease the elevation angle without much change in tether length.

$$F_t = -P_w(\cos(\phi)\cos(\beta))^2(1 + \left(\frac{L}{D}\right)^2) \tag{3.38}$$

The gravitational forces on the kite are then computed in the radial and theta directions, since there is no effect of gravity in the phi direction, as seen in Figure 3.3. Equations 3.30 and 3.31 are utilized to calculate these forces. These forces are calculated before the kinematic ratio iterations, as the ratio has no effect on these force vectors.

With the gravitational force vectors known and an approximate tether force, the aerodynamic force vector can then be calculated. As seen in Equation 3.28, the aerodynamic force is dependent upon the kinematic ratio. An iterative process is used at each time step to calculate the kinematic ratio and update several variables, such as the aerodynamic force, which is updated with Equation 3.39, which is similar to Equation 3.28, but utilizes the kinematic ratio in place of the lift to drag ratio. The

aerodynamic force is then then broken down into polar coordinates with the following equations, but there is no magnitude in the phi direction, as can be seen in Figure 3.3 Additionally, since the only forces acting on the kite in the theta direction are the aerodynamic and gravitational forces, their magnitudes in these directions must be equal and opposite, yielding Equation 3.40. To calculate the remaining radial aerodynamic force component, basic trigonometry leads to Equation 3.41.

$$F_a = C_R P_w S(1+\kappa^2)(\sin(\theta)\cos(\phi) - f^2) \tag{3.39}$$

$$F_{a,\theta} = -F_{g,\theta} \tag{3.40}$$

$$F_{a,r} = \sqrt{F_a^2 - F_{a,\theta}^2} \tag{3.41}$$

The tangential velocity factor is similarly updated, using Equation 3.21 with the kinematic ratio in place of the lift to drag ratio as seen below.

$$\lambda = a + \sqrt{a^2 + b^2 - 1 + \kappa^2(b-f)^2} \tag{3.42}$$

With this calculated tangential velocity factor and kinematic ratio, the apparent wind velocity magnitude can be calculated from rearranging Equation 3.20, and utilizing the kinematic ratio in place of the lift to drag ratio, producing Equation 3.43. The apparent wind vector is then calculated in polar coordinates as a function of the tangential velocity factor, reeling factor, wind speed, and polar coordinates, with Equations 3.9 - 3.11.

$$v_a = v_w(\sin(\theta)\cos(\phi) - f)\sqrt{1+\kappa^2} \tag{3.43}$$

Since the kinematic ratio is equivalent to the lift to drag ratio if mass is neglected, and this analysis includes mass effects, the approximation is insufficient for this analysis as it would cause inaccuracies. The target glide ratio is the ratio of the lift coefficient and the drag coefficient. For each phase, these values are nearly constant, specified as an input for the system and a function of tether length. The goal is to select a kinematic ratio which represents the aerodynamic properties, specifically the glide ratio, of the kite accurately. A new glide ratio is calculated during each iteration using Equation 3.32, and if the difference between the two values are within a certain error value, 0.001 in this analysis, the corresponding κ is utilized for that time step to update additional variables. The lift and drag coefficients are provided as input variables and are experimentally derived for the selected kite. In traction and transition, the kite is powered and has similar coefficients, while the kite is de-powered in the retraction phase and has a significantly lower lift coefficient. The kinematic ratio is updated with Equation 3.44, to estimate a new value if the produced glide ratio was insufficient in the previous iteration. [19]

$$\kappa_{new} = \kappa\left(\frac{G}{G_{new}}\right)^{0.5} \tag{3.44}$$

With a selected kinematic ratio and glide ratio for the current time step, several parameters are updated again with a force balance. The aerodynamic force vectors are ultimately calculated as shown below, utilizing the other calculated force values. The magnitude is calculated from the vector components, as shown in Equation 3.48.

$$F_{a,r} = -F_t - F_{g,r} \tag{3.45}$$

$$F_{a,\theta} = -F_{g,\theta} \tag{3.46}$$

$$F_{a,\phi} = -F_{g,\phi} \tag{3.47}$$

$$F_a = \sqrt{F_{a,r}^2 + F_{a,\theta}^2 + F_{a,\phi}^2} \tag{3.48}$$

The final reeling factor is then updated as a function of the aerodynamic force and kinematic ratio by rearranging Equation 3.28. If the calculated reeling factor exceeds operational limits, producing too much or too little force, it is adjusted properly to be within operational limits. This equation is almost identical to Equation 3.37, but the aerodynamic force is used instead of the tether force, and

the kinematic ratio is used in place of the lift to drag ratio, as should be done when including mass in the model [5].

$$f = \cos(\beta)\cos(\phi) - \sqrt{\frac{F_a}{P_w S C_R (1+\kappa^2)}} \tag{3.49}$$

The tether forces at the kite are then recalculated to produce realistic values, since the tether force does not stay constant in reality. With the tether force completely in the radial direction, the final tether force can be calculated with Equation 3.50. The radial component is equivalent to the tether force magnitude since the force in the theta and phi directions is zero. The calculated tether force is then utilized in a force balance of the tether to calculate the tether forces at the ground station, and ultimately the generated power.

$$F_t = F_{a,r} + F_{g,r} \tag{3.50}$$

The tether forces at the ground station are then calculated in polar coordinates as shown below, using the methods of [13]. In the radial direction, there is only the tether force and the radial component of the gravitational force on the tether. In the theta direction, there is a lesser gravitational force from the tether weight. There is also a force component from the tether movement. In the phi direction there is no force from gravity, but a single force from the tether motion. The resultant magnitude of these vectors is used to calculate power generation, as shown in Equation 3.33.

$$F_{g,r} = F_t - m_t g \cos\theta \tag{3.51}$$

$$F_{g,\theta} = 0.5 g m_t \sin\theta + \frac{1}{16} C_{D,t} D_t r \rho v_a^2 \frac{v_{a,\theta}}{\sqrt{v_{a,\theta}^2 + v_{a,\phi}^2}} \tag{3.52}$$

$$F_{g,\phi} = \frac{1}{16} C_{D,t} D_t r \rho v_a^2 \frac{v_{a,\phi}}{\sqrt{v_{a,\theta}^2 + v_{a,\phi}^2}} \tag{3.53}$$

For all three phases, the following equations are utilized to update velocity values. Rearranging Equation 3.14 allows the the radial kite velocity or reeling speed to be calculated with a known reeling factor, as shown with Equation 3.54. The tangential kite velocity can be similarly solved for if the tangential velocity factor is known by rearranging Equation 3.12, as shown in Equation 3.55. The total kite velocity is then calculated from its two components, the radial and tangential kite speed components, which depend on the wind speed, reeling factor, and tangential velocity factor. The kite tether length is then updated as such with Equation 3.57 [5].

$$v_{k,r} = v_w f \tag{3.54}$$

$$v_{k,\tau} = v_w \lambda \tag{3.55}$$

$$v_k = \sqrt{(v_w f)^2 + (v_w \lambda)^2} \tag{3.56}$$

$$r = r + v_{k,r} \Delta t \tag{3.57}$$

For the retraction and transition phases, the position calculations are simpler than with traction because the course angle is assumed constant and no complex pattern is flown. For these phases, it can still be assumed that the flight path is 2D, as with the previous computational model. During retraction, the course angle is completely upwards, at 180°, and for the transition phase the course angle is downwards at 0°. The azimuth angle is also assumed to be constant, which is dependent upon the initial azimuth angle, specified as an input. The elevation speed, and therefore the elevation angle, does, however, change in both the retraction and transition phase. The updated elevation values for retraction and transition are updated with Equation 3.59, using Equation 3.58 to calculate the elevation speed, using methods from [5].

$$v_\beta = \frac{v_w \lambda \cos(\chi)}{r} \tag{3.58}$$

$$\beta = \beta + v_\beta \Delta t \tag{3.59}$$

Since the traction phase follows a more complex flight path, different computational methods must be used. Additional equations are utilized to update the tether length as well as the elevation, azimuth, and course angles at each time step. The previous calculations provide a base center path, which serves as the ”center point” of the figure-eight flight path for the traction phase. To add in the curving figure-eight path, Lissajous curves were used to provide a pre-defined path shape as a guideline for the flight path updates. The following Lissajous curves were utilized to produce the figure-eight movements of the traction flight path. These curves produce a figure-eight curve with a width of 2*A_ϕ and a height of 2*A_θ [28].

$$y = A_\phi \sin(s + C) \tag{3.60}$$

$$z = A_\theta \sin(2s) \tag{3.61}$$

where C represents a phase shift and s is a dimensionless ”positional time step” that represents the position along one figure-eight curve. For this variable, a value of 0, π, or 2π would be at the center point of the figure-eight.

The elevation and azimuth angles for the traction phase are updated with Equations 3.62 and 3.63, respectively. A_ϕ represents the width of half the figure-eight curve. Similarly, A_θ defines half of the figure-eight curve height. The derivatives of the elevation and azimuth angle update equations with respect to s are shown in Equations 3.64 and 3.65.

$$\beta = \beta_0 + A_\theta \sin(2s) \tag{3.62}$$

$$\phi = \phi_0 + A_\phi \sin(s + C) \tag{3.63}$$

$$d\beta = 2A_\theta \cos(2s) \tag{3.64}$$

$$d\phi = A_\phi \cos(s + C) \tag{3.65}$$

To update the variable s, the methods of [28] are utilized. The arc length equation is rearranged to solve for the change in s for one time step, ds, as shown in Equation 3.66. The unit-less distance along the Lissajous figure for one time step, ΔL, or the distance traveled in traction during one time step, can be approximated by Equation 3.67 since the time step is relatively small. This provides a linear approximation of the actual curved path by using the tangential kite velocity can be assumed negligible for this analysis, but could be improved for further analyses. The ”position step” can then be updated with Equation 3.68.

$$\Delta s = \frac{\Delta L}{\sqrt{(d\beta)^2 + (d\phi)^2}} \tag{3.66}$$

$$\Delta L = \frac{v_\tau \Delta t}{r} \tag{3.67}$$

$$s = s + \Delta s \tag{3.68}$$

The course angle during traction is updated with the newly calculated polar position coordinates using Equation 3.69. These angles are then utilized to evaluate the possibility of the simulated flight path, as the turning rate is compared to values from experimental data, which will be elaborated upon further in the following chapters.

$$\chi = \tan^{-1}\left(\frac{A_\theta \cos(2s)}{A_\phi \cos(s + C)}\right) \tag{3.69}$$

From here, the power value of the time step is generated, using Equation 3.27, and the simulation continues with the next time step until the end of the cycle condition is reached.

3.4. Simulation overview

Based upon the outlined equations, a single kite flight simulation code was previously developed at Kitepower to calculate the power and energy from a single kite as a function of numerous input parameters. This code provides a simulated 2D flight path over time for one full cycle, with speed and force updates at each time step. The code also utilizes pre-defined target points which indicate the path's direction and stopping point in each phase. The updated 3D path module utilizes similar functions for the retraction and transition phases, since these paths are simple and the previous simulation output was suitable for this analysis. Ideally, there is no significant movement in the phi direction during these two phases, so the traction phase is more important to analyze for kite collisions. However, in actual flight tests, the azimuth angle in retraction and transition can deviate from the ideal angle greatly, and this should be addressed in future path simulation improvements. Alternatively, flight control strategies could be altered to follow more of an ideal path in these phases.

For the traction phase, the kite path code was modified to define the traction path with Lissajous curves as described in the previous section. In the updated code, a pre-defined figure-eight path is incorporated into the traction path to provide a more realistic 3D flight path, which will allow for a higher fidelity kite farm spacing analysis. The output from the single kite module serves as an input for the newly developed kite farm module, which will calculate the power of the entire farm, as well as the certainty of non-collision. All of the computational modules utilized in this analysis are outlined below in Figure 3.5. The light grey boxes represent input files, which define the characteristics of the environment, kite system, or kite farm. The simulated kite path module provides the main input to the farm modules. The pre-defined flight path becomes a function of time in the single simulated kite path module, which is used to model the path of each kite in the kite farm model. The newly created modules include the farm layout and kite farm simulation modules. The farm layout is a function of input variables, and visualizes the ground station of each kite in the specified orientation, taking consideration of the wind direction. The kite farm simulation then runs the single kite simulation for each kite, and utilizes a unique flight envelope for each kite as well as a phase shift if specified. The output of this module is the total farm power, kite farm density, and certainty of non-collision between kites.

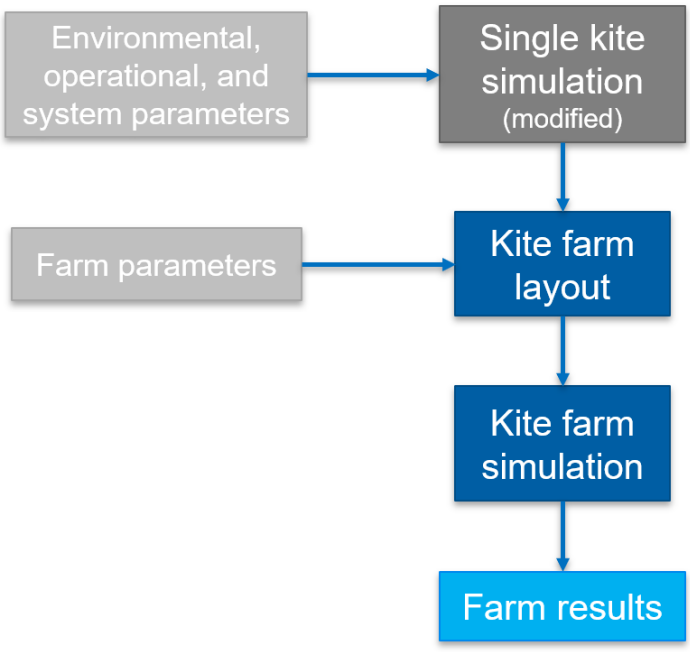

Figure 3.5: Computational method overview

4

Flight Path Development

Using the methods described in the prior chapter, and utilizing the previously created 2D simulated path model, improvements were made to develop the 3D simulated flight path. The 2D and 3D simulated paths will be compared to evaluate the effect of including the figure-eight curves in traction, and then the 3D simulated flight path will be compared to experimental data to ensure the accuracy of the model. Initially, the turn rate of the kite will be analyzed to determine if the simulated path exceeds realistic operating conditions by turning too quickly. Then, the simulated flight path will be directly compared to experimental flight cycles to visually compare the paths. Additionally, the flight paths will be visualized over time to identify any inconsistencies, since this is essential for evaluating or predicting the distance between kites in a kite farm accurately.

4.1. Simulated path comparison

The previously created Kitepower path simulation models the kite flight path without the figure-eight movement in traction, as shown in Figure 4.1. This simple path was selected to simplify calculations and decrease computational time. In this figure, the traction phase flight is represented with constant elevation and azimuth angles, which approximates the center of the figure-eight that would actually be flown. This approximation estimates the traction phase duration reasonably well for single kite applications, but should include the realistic 3D traction path for a more accurate assessment of kite farm spacing. The single kite path simulation begins with the retraction phase and calculates the kite velocity at each time step, which then updates the position of the kite as well.

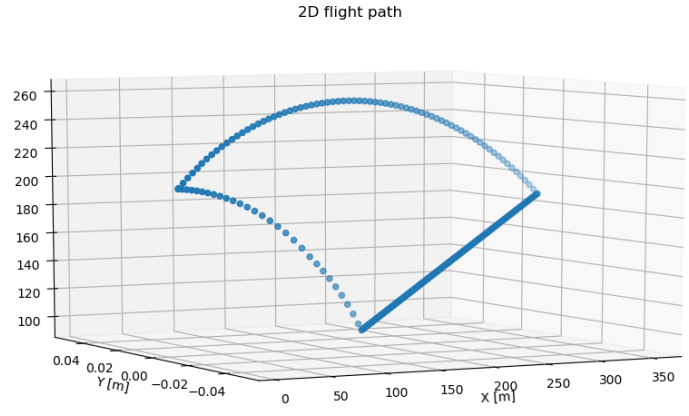

Figure 4.1: Idealized 2D flight path

The 3D flight path code incorporates the figure-eight motion during traction, with the methods from the previous chapter, and more accurately models the flight path. This path can be seen in Figure 4.2, which shows the simulation of a complete cycle, and it can easily be seen that the path is greatly

different in the traction phase. The figure-eight movement of the path is significant for kite farm optimization, as the exact kite location is essential in determining the probability of a collision between kites. If kite farm is dense and there is a phase shift between kites, the probability of collision increases, so the flight path should not be modeled in an idealized way. Not accounting for the traction phase motion could result in a higher kite farm density than should actually be implemented, increasing the possibility of collision. For example, with two adjacent kites aligned with the wind direction, a phase shift could place the upwind kite in traction near the downwind kite in the end of it's reel-out phase. If the downwind kite is still in reel-in or transition, it is more likely to collide with the upwind kite, as they are in close air spaces. For this reason, in-line kites typically should not have a significant phase shift [13].

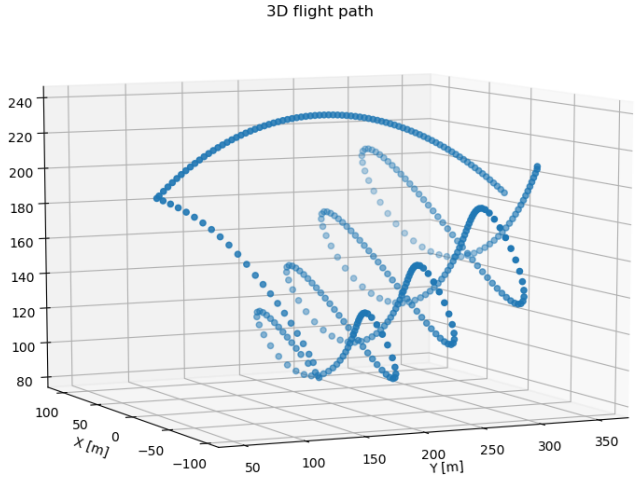

Figure 4.2: 3D Flight Path

Data from several flight testing events was utilized to get a wider scope of operational conditions and the impact on the flight path for the same system. An overview of the operational conditions of each flight even is shown in Table 4.1, in which the m^2 kite system was used. All three flight tests flew different flight paths, yet had relatively similar cycle durations, with only Flight Test C deviating slightly more than the others. This can be attributed to a slightly shorter range of the minimum and maximum tether lengths. Flight test A was selected for further comparison with the simulated flight path because it generated clear data patterns which best followed ideal flight performance. Although Flight test C provided significantly more flight cycles than the other testing events, much of the data was difficult to interpret. There were clear cyclical outputs but the tether force values varied greatly over time, making it difficult to identify system operating points which the simulation heavily relies on to produce a simulated flight path. The operational conditions for Flight test A were utilized as input for the path simulation, and the two paths are compared in Section 4.3. It should be noted, however, that a short retraction time is more desirable, since this requires less time providing energy to the system. While Flight test A features a long retraction time, it still provided the best data to analyze and provided the most consistent flight patterns, making it a reasonable choice to represent with the path simulation. From this data set, input parameters for the 3D flight path simulation were derived. These values are shown in Table 4.2, and it can be seen that not all values are similar. In the retraction phase, a much lower force limit is used to match the path spatially and temporally. The traction tether force is slightly lower than the flight test limit, since with the simulation, the defined tether force is quickly reached and stabilized, whereas in the flight test, it is not so ideal. The maximum velocity, v_{max}, or maximum reeling velocity, is dependent upon the constraints of the selected components, so this was considered a variable which would be initially selected for optimal performance, and readjusted if needed depending on component limitations. The maximum velocity greatly impacted the alignment of the figure-eight maneuvers with the experimental data, and a value of 13 m/s was found to produce the closest simulated flight path. The speed ratio, which is defined as the ratio of the maximum reeling speed to the minimum reeling speed, was found to slightly impact the path accuracy as well, specifically with the single cycle duration. To best fit the experimental data, a value of 5.5 was selected, providing

a minimum reeling speed of 2.36 m/s. The force values were selected because they produce similar simulated tether force values as compared to the experimental force values for similar flight paths.

Table 4.1: Simulated path comparisons

	Flight test A	**Flight test B**	**Flight test C**
Total cycles	15	17	64
F_{out} [kg]	7500	4000	3500
F_{in} [kg]	2000	1000	1000
r_{min} [m]	200	150	250
r_{max} [m]	400	300	325
β_{out} [°]	30	34	24
Avg. retraction duration [s]	71.34	24.50	30.64
Avg. cycle duration [s]	144.92	146.59	117.82

Table 4.2: Simulation Input Parameters based upon Flight test A

Input	**Value**
F_{in}	987 N
F_{out}	6,631 N
r_{min}	200 m
r_{max}	400 m
β_0	30°
ϕ_0	0°
Speed ratio	5.5
v_{max}	13 m/s

The differences between Flight test A, the 2D simulated path, and the 3D simulated path are detailed in Table 4.3. With the simulated paths, the introduction of the 3D traction phase caused the total cycle duration to increase by 16 seconds, which is closer to the average cycle duration from all three experimental flight tests. This shows an improvement over the 2D path, but also shows a decrease in both the average mechanical and electrical power, which suggests more realistic values since simulated flight cycles often overestimate the power output [13]. This could be a result of the long traction duration for this flight path, or could suggest an area of future improvements for the traction phase simulation. From the 2D to 3D simulated path, the retraction duration actually decreased, while the transition time slightly decreased. The 2D path underestimates the traction phase duration, while the 3D path overestimates this duration. The differences between the two paths highlight that the 3D path is overall heading towards a more accurate representation of the actual flight data, but some improvements could still be made with additional modifications. The duration data from the flight test seems to be quite different from the simulated path for at least one phase, but this could be the result of unclear flight test results or the deviation from an ideal path. Since there is no identifier in the test data to indicate when each phase is starting, this has to be manually defined from the flight path visualization and depower values, so the flight test duration values are estimates and could be improved in the future. Additionally, in experimental flights, the retraction phase is often flown in a sideways arc shape, increasing and then decreasing the azimuth angle throughout the phase. This increases retraction time and could account for the large difference between experimental duration and simulated duration. This is also a good maneuver to fly in a small kite farm systems to utilize a more ideal azimuth in the traction phase, but to create space for another kite while it is retracting. This maneuver, however, should likely only be done if there are no additional kites in the direction in which the arc is flown. But, this is difficult to implement in the flight path simulation as it would

require a restructuring of the retraction phase code and would add significant computational time to farm simulations since the number of azimuth path analyses would more than double. The total cycle duration time of Flight test A is an average of all 15 regular cycles, but the individual phase duration values are based off one representative cycle, so more more error is introduced and this should be re-visited in the future for simulation path verification. This was due to time constraints and the requirement to manually identify the sections, making it a lengthy process to conduct for all 15 cycles. The fact that the 3D path simulation has a total cycle duration closer to the flight test data than that of the 2D path is promising, showing progress in the right direction. Additionally, since temporal accuracy is more important for kite farm spacing than the accuracy of the power, the 3D path can be seen as a great improvement. While there is still room for future improvement in the simulated path, the deviation is much less than that of the 2D path, and the 3D path should be able to provide results within reasonable accuracy. As for the power density values, since the 3D path slightly underestimates the power, the power density values can be seen as conservative. Using the 2D path would provide an overestimate, which could lead to a low capacity factor if a system were designed for a larger power output.

Table 4.3: Simulated path comparisons

	2D path	**3D path**	**Flight test A**
Retraction duration [s]	27.86	36.29	71.34
Transition duration [s]	6.44	5.47	8.48
Traction duration [s]	59.33	79.80	65.10
Total cycle duration [s]	93.63	121.55	144.92
Avg. Mech. Power [kW]	8.30	7.51	8.12
Avg. Elect. Power [kW]	7.04	6.32	6.90

4.2. Turn Rate Analysis

The first measure of simulation verification was to evaluate the rate of change of the course angle, which is known as the course rate or turn rate. This defines how quickly a kite of a certain size can turn while in normal operation, and can be useful in further kite farm analysis to evaluate collision avoidance in more extreme situations.

Several experimental data files were available from Kitepower's previous flight testing events, providing position and velocity data over several hours of kite operation, for multiple kite sizes and environmental conditions. For several tests, a pitot tube was implemented on the kite to directly measure the apparent wind speed. With this data, more realistic kite laws can be developed to better model the kite path. Calculations were made to evaluate turn rates of actual flight conditions, to confirm if the simulation results were realistic. Each kite's maximum turn rate value is limited by the size and shape of the kite. Larger kites tend to have lower maximum turn rates since they are more difficult to maneuver due to larger masses and therefore larger mass moments of inertia [29]. Evaluating for the average turn rate during traction, specifically in times of turning, will allow for an approximation of the typical turn rate for each kite size for the Kitepower system. This will, in turn, allow for an interpolation of the average kite turn rate for larger sized kites, which will be beneficial for future kite modeling. However, turn rate values should be confirmed with experimental data for each individual kite.

Average kite turn rate values were derived by separating the traction flight patterns, and identifying the regions where the kite was turning, or at the curved edges of the figure-eight pattern. Outside of these regions, the turn rate is nearly zero and should be excluded. In an ideal turn, the turn rate would be constant throughout the whole turn, and would be a similar value for each turn. As this is not the case in actual flight tests, the average of all turn rates was taken to be the single average turn rate for one flight test. To separate the sections of the cycle where the kite was turning, the depower and steering input values were utilized. The kite is at maximum depower setting during the retraction phase, so it operates at a significantly lower depower value in transition and traction. The lowest depower value can be assumed to represent the traction phase, so it was used to isolate the phase of interest. Additionally, during right and left turns during traction, the steering input is set to a constant value for the duration of the turn, which was used to identify the regions where the turn

rate law can be applied. This was performed for several flight test data sets, of similar kite sizes, to provide one average turn rate for the Kitepower system with a 25 m^2 kite. The turn rate was only an analyzed in the traction phase because that is typically where the highest kite speeds are achieved, and therefore also the highest turn rates. This analysis can be applied to the retraction and retraction phases as well, but the course angles are ideally constant in these phases, so the maximum kite turn rate is mostly irrelevant in these phases.

The turn rate, $\dot{\chi}$, is characterized with Equation 4.1 from [5], as a function of the steering input, δ, apparent wind speed, and the variable G, an experimentally determined kite characteristic. Here, the steering input is the distance which the steering tape moves from the center in order to steer the kite towards the left or right. In [30], the G value for Kitepower's 25 m^2 kite during traction was 0.220 rad/s. This was calculated using experimental flight data and the equation below. In [29], a G value of 0.295 rad/s is calculated from experimental flight data of a 14 m^2 kite in traction. This kite, however, had a slightly different system configuration than Kitepower's, since it utilized 3 steering lines connected to the ground station, where Kitepower's system has only one main tether. This could introduce some slight differences in the G values. In an ideal turn, there will be no side slip on the edge of the kite, and the kite will maintain a constant radius from the central turning point, creating a perfect arc without changing the kite's aerodynamic coefficients [29]. However, in reality, this does not always occur, so it is expected to have some variance in the average turn rate data.

$$\dot{\chi} = G v_a \delta \tag{4.1}$$

Two main data sets were analyzed to calculate the average turn rate during traction for Kitepower's 25 m^2 kite. These flight tests featured relatively accurate apparent wind speed measurements from pitot tube readings, which were not present in other data sets, allowing for a simple and direct application of Equation 4.1. While the apparent wind velocity can be calculated from the interpolated wind speed at the kite height and the kite velocity, the interpolated wind velocity has a high margin for error since wind speed is constantly changing. When the wind speed is only measured 6 meters above the ground, and the wind speed at the kite is calculated, this introduces more room for error, so a direct apparent wind speed measurement is preferred.

After the turning data was selected, it was additionally separated by left and right turning movements to see any difference in patterns on each side of the figure-eight. Following Equation 4.1, the apparent wind velocity multiplied by the steering input was plotted against the turn rate to find an average G value for each data set. However, the data had large variations, with relatively high deviations from ideal behavior, so much of the relevant data set was removed. Due to limited temporal resolution and large changes between collected data points, high turn rates were often calculated for some time steps, when in reality, the turn rate would not have been so large. A small time step, of approximately 0.10 seconds, and a large change in course angle could result in a turn rate of greater than 2π radians per second, which would mean the kite would do one complete revolution in one second. Since this is unreasonable, a conservative upper limit of 3 radians per second was applied, and any data with a value higher than this was excluded. Additionally, small delta values were excluded as well, because a turn is set to occur at high steering input values, so a delta of 0 would indicate almost no turn. In the future, applying a filter to smooth the experimentally collected data would allow for better post processing. This would remove large spikes in the data, and provide improved data.

For the first flight test data set, the data was manipulated to isolate the traction phase, and then the turning sections were identified. The turn rate was calculated as the change in the course angle over time for the entire flight test. The values during turning time periods were then analyzed as shown in the graph below to calculate the G value, which was calculated to be 0.757 rad/s, which is much higher than previous values from other analyses. However, it is expected that the large spikes in the data have led to a significantly higher G value than the other publications have found. Additionally, differing flight paths and conditions could lead to different values as well. The average kite speed in traction for the first data set was approximately 21 m/s, with an average turn rate of 0.98 rad/s. For the second data set, with a much lower traction force values, the average kite speed during traction was 20 m/s, and the average turn rate was 1.08 rad/s. Since the two average turn rates are similar, it can be assumed that these values are relatively accurate. The complete turn rate results from the first data set are seen in Figure 4.3, which identifies left and right turns, and draws a trend line from all turn rates. The absolute value of the slope of the line is the value of the parameter G.

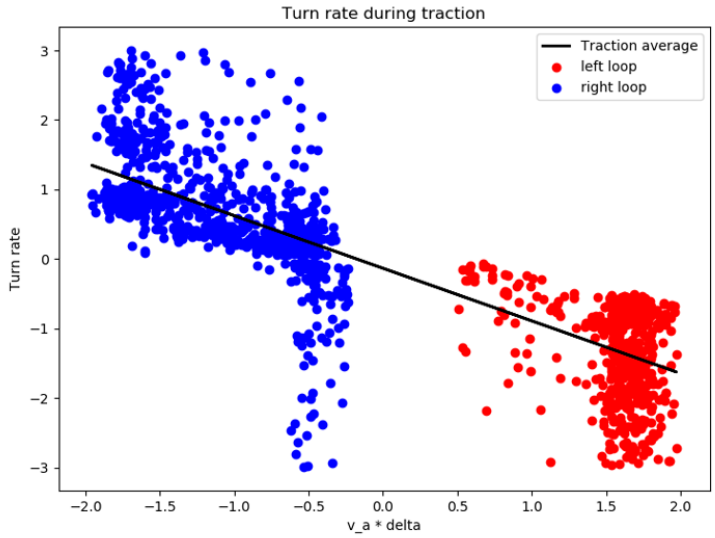

Figure 4.3: Turn rate results

The turn rates through the simulated flight path were calculated in the same way as with the experimental data. After the simulated path was completed, each turn rate within the traction phase was evaluated with the upper limit as calculated with the experimental flight data. In this case, the average turn rate was utilized as a maximum limit, with a factor to allow for some higher turn rates within reason. The maximum turn rate from the experimental data was not used as a limit because extremely large turn rate values were calculated from the flight test data, and an average turn rate would provide a more accurate value. The simulated flight path produced a maximum turn rate of 1.47 rad/s, which occurred during the turning sections of the traction phase, which seems to be reasonable and does not exceed the average turn rate from the test data by too much. As with the test data results, the turn rate is not completely constant throughout each turn in the simulation, but varies throughout the turn. Ultimately, it can be concluded that the simulated data fits within experimentally tested turn rate limits, and is sufficient for kite farm modeling.

Since the kite is fully powered in normal traction operation, kite turning and maneuverability becomes quite important. If an incident occurs during traction, the kite can be depowered to turn more quickly, which would be important for analyzing higher risk kite collision avoidance, such as with closely spaced farm systems that rely heavily on controls. But in this case, the average G value and turn rate from experimental data of each kite type will suffice, since it provides a realistic average turn rate approximation for farm simulations.

4.3. Simulated path verification

To evaluate the accuracy of the shape of the simulated flight path, as well as position over time, the simulated flight path was compared to several cycles from the experimental test flights. Cycles which resembled steady state flight were selected from each data set to compare against the simulated single cycle path. The simulated flight path could initially be tuned with amplitude factors to modify the width and height of the figure-eight shape, but it became apparent that a phase shift in the Lissajous equation was also necessary to more closely model the flight path and account for the ”droop” caused by gravity effects and a different control algorithm, as seen in Figure 4.4a which shows part of an experimental traction phase. Because of gravitational effects the kite also flies more quickly downwards and more slowly upwards. A phase shift in the Lissajous curves modifies the ideal figure-eight shape to more closely model the actual flight path, as can be seen in Figure 4.4, which compares a single Lissajous curve without and with a phase shift. Due to the phase shift, the kite will also fly more quickly when moving downwards, and slower when moving against gravity.

Since experimental data for the 25 m^2 Kitepower kite system was the most abundant, this was the main focus of in analyzing the match between the experimental and simulated paths. With the first

Figure 4.4: Lissajous phase shift effect

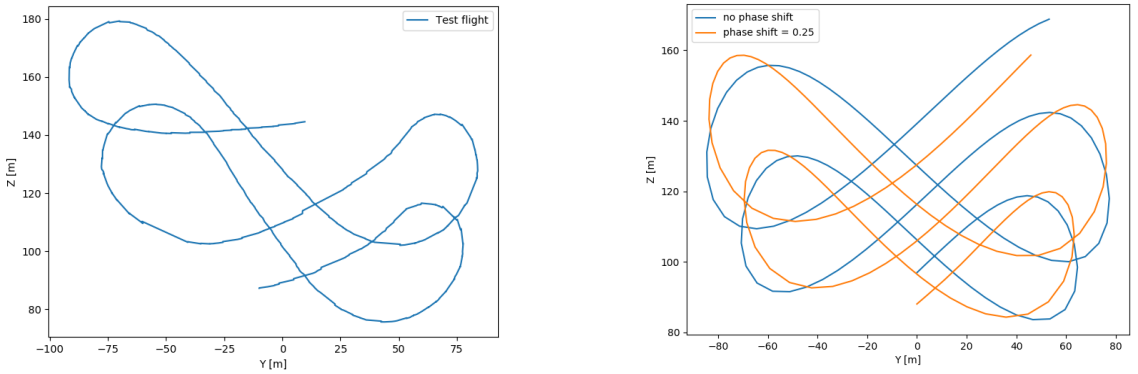

(a) Experimental flight traction maneuvers

(b) Simulated flight traction maneuvers

flight test data set, four full cycles were extracted from the data for comparison since they most closely represented ideal flight, meaning there were no large deviations from the intended path and they flew several figure-eight maneuvers. Ultimately a phase shift of 0.25 radians was selected, as it fit the experimental data best. Additionally, the Lissajous parameters $A_\phi$and A_θ were selected as 0.34 and 0.10 respectively. These correspond to the height and width (in the phi and theta directions) of the figure-eight and show that the figure-eight will be approximately 3 times wider than it is tall. The phase shift indicates a shifted shape, with the tops of the figure-eight shapes curving more sharply than at the bottom. This also introduces fewer time steps in the downwards movements, which corresponds to the acceleration of the kite due to gravity. However, since the kite does not fly an ideal path in reality, the Lissajous curve representation has limitations. The figures below show the simulated path compared to experimental flight paths, and it can be seen that some experimental paths are better represented by the simulated path than others. Figures 4.5 and 4.6 show experimental data sets which most closely follow the simulated path, while Figures 4.7 and 4.8 less closely follow the simulated path. The cycle number identified in each figure title refers to the cycle number in the experimental test. There were a total of 18 cycles identified for this data set, but only a few exhibited ideal or steady state behavior, so the best four cycles were utilized. Additionally, the maximum speed and speed ratio values were modified to better fit the simulated path to each experimental path.

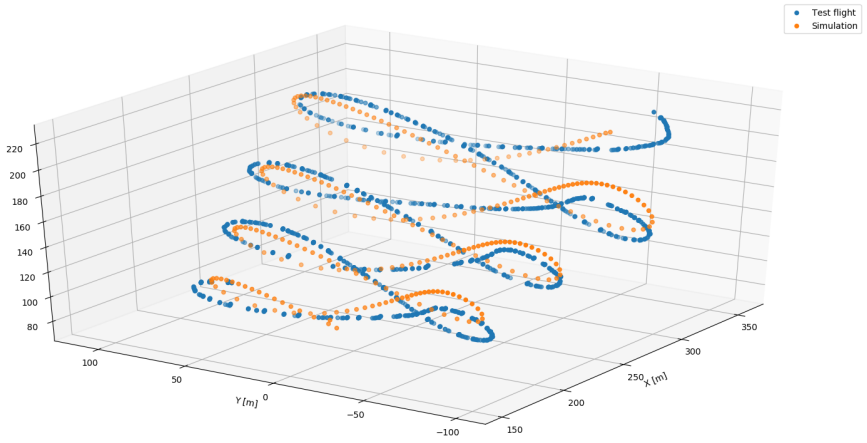

Figure 4.5: Experimental flight cycle 1 comparison

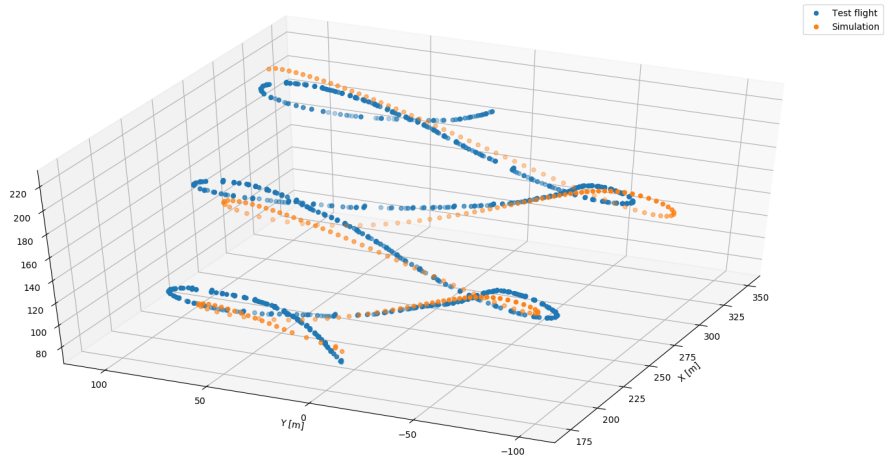

Figure 4.6: Experimental flight cycle 12 comparison

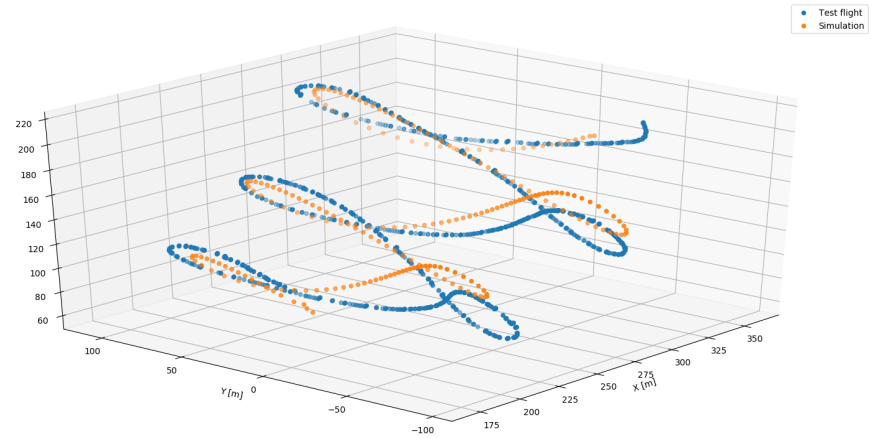

Figure 4.7: Experimental flight cycle 3 comparison

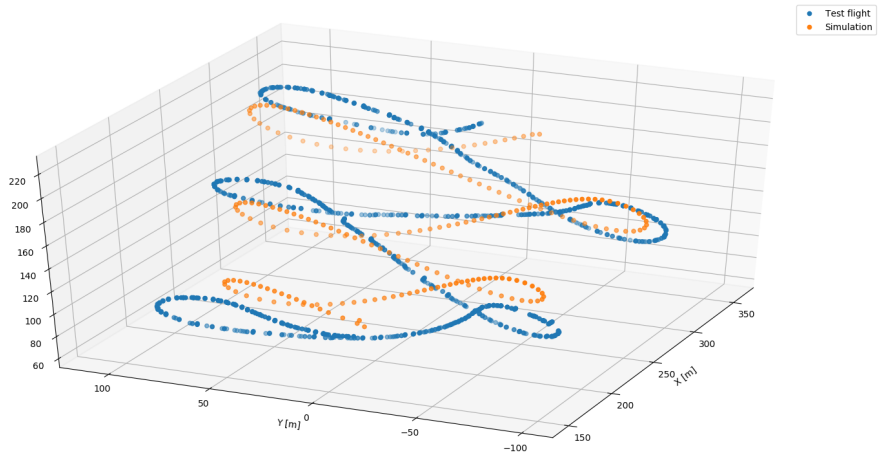

Figure 4.8: Experimental flight cycle 4 comparison

As seen in the above figures, mainly in Figure 4.5, the experimental flight paths are slightly rotated upwards towards one side, in plane with the figure-eight shape, so an ideal Lissajous curve representation is too low on one side and too high on the other. For this case, the Lissajous path is a bit higher

than the experimental path on the right hand side of the loop, and slightly lower on the left hand side. The difference is, however, small enough to utilize the simulated path. For the seemingly worst matched data set from above, cycle 4, the maximum deviation between the simulated and experimental flight paths in the traction phase is 52.8 meters. For the better seeming fit of cycle 1, shown in Figure 4.5, the maximum deviation is actually higher at 64.9 meters. However, the average path deviation in traction for cycle 1 is 28.9 meters, while the average deviation is 28.5 meters for cycle 4. So although some paths may not visually seem to be as good of a fit, the data shows reasonable path accuracy during the traction phase and these average deviations will be considered when addressing the factor of safety for the kite farm. The addition of a safety factor in the analysis will account for expected spatial deviations in the path, which are often common in flight tests, as seen from the several widely different flight paths within the same test set of data. This safety factor will be greatly needed, because the kites do not always fly an ideal path, and the path can vary greatly from one cycle to the next, especially if environmental conditions are changing. In the future a more in depth and computationally expensive model should be created to further improve the simulated kite path, but the current model is reasonable for kite farm modeling. Two of the experimental cycles were modeled well by the simulated path, and the remaining two selected cycles were approximately modeled by the simulated path. The large variation between experimental cycles is difficult to account for in a model, so the simulated path serves as a reasonable approximation of the average and ideal flight path.

In the following figure, the side view of the simulated path and experimental cycle 1 are shown, and it can be seen that the figure-eight curves align well and occur almost simultaneously. This means that the reel out speed is represented well, but it can be seen that there is a large variation in position during retraction from the ideal path. However, the ideal path does represent the approximate average of this irregular path seen in Figure 4.9. The transition phase is also represented reasonably well, but is more conservative than the experimental data, which should be taken into account for the farm analysis, as the transition phase is an important area to evaluate for out of phase collisions. Other experimental cycles, shown in Appendix A, provide a path that more closely follows the simulated path in the retraction and transition phases, however. Additionally, it can be seen in Figure 4.10 that the experimental flight path varies in azimuth, creating a less ideal path. But overall, the simulated path is a valid representation of the experimental flights. Since the transition between phases is assumed to be instantaneous in the simulated path, this should be accounted for in the kite farm analysis. In reality, the kite does not immediately change course angle and start the next phase, but there is a gradual change from one phase to the next. In future work, it would be a great improvement to add these gradual phases transitions, which will provide a smoother path as the phases change.

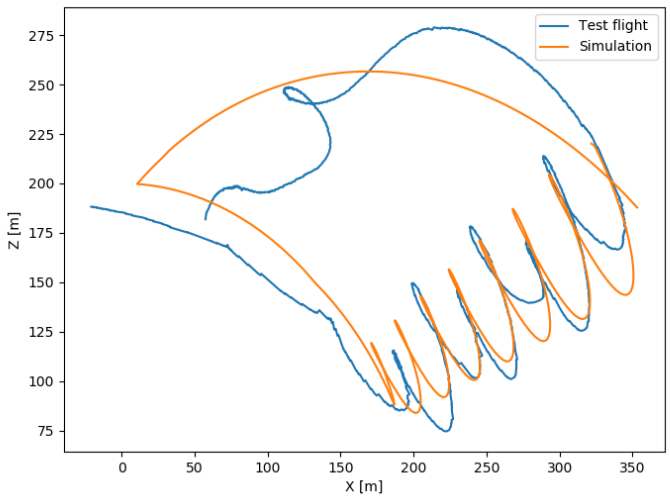

Figure 4.9: Side view path comparison for cycle 1

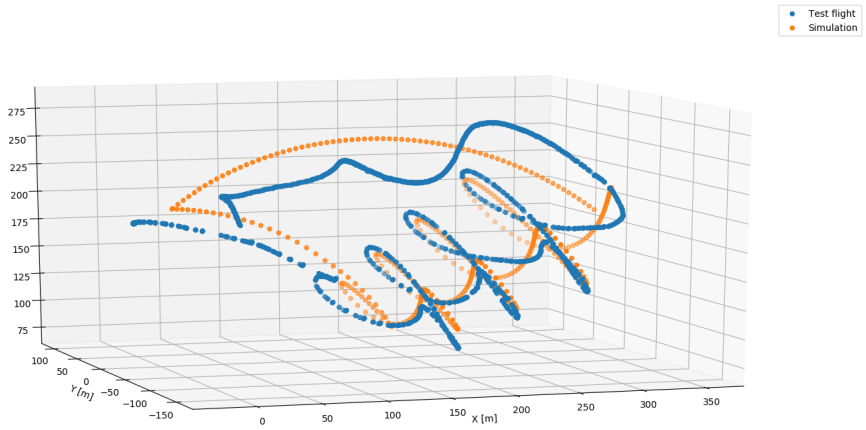

Figure 4.10: Full path comparison for cycle 1

Several 40 m^2 flight tests were analyzed as well, but a new, larger kite size is in the early stages of testing, so flight test data was unavailable. Additionally, the turn rate limits for each kite are difficult to determine exactly, since they are typically not flown in extreme maneuvers during normal operation. This allows for only a first approximation of the average or possible flight path for each kite size. It is assumed that larger kites will have slower handling, suggesting slower maximum turn rates, but this has not been experimentally verified with any in-depth testing. Several of the 40 m^2 kite flight tests flew figure-eight maneuvers which were similar in size to those of the 25 m^2 kite system, suggesting that the flight tests were not operating close to the maneuverability limits of either kite, which also makes it difficult to interpolate the limits for larger kites. With the currently available data, average Lissajous parameters were selected for each kite size to determine reasonable parameters for larger kites, as shown in Figure 4.11. This ensures that the kites are not flying close to the maneuverability limits, but may also be a conservative assumption. A logarithmic function seemed to match the data best, but this should be further verified with additional kite sizes and a more in depth analysis of potential flight paths with each kite. For the future, it is suggested that turn rate limits should be derived from experimental tests for each individual kite, and with information from three kite sizes, an improved interpolation can be used to determine the turn rate limits of larger kite sizes.

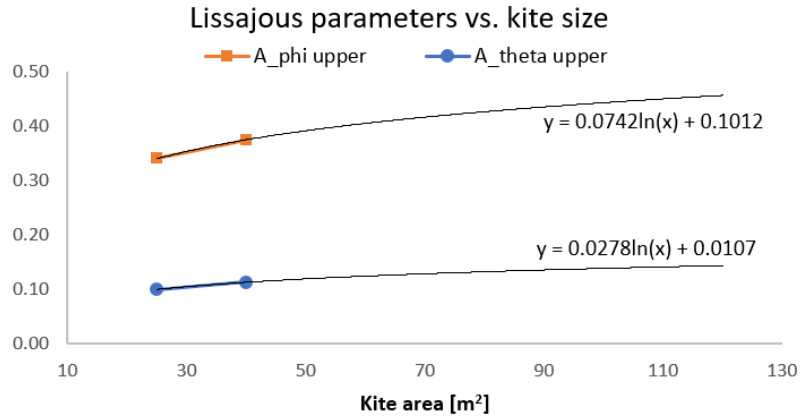

Figure 4.11: Lissajous parameter interpolation

4.4. 3D flight path evaluation

To provide a ”base case” for comparison in the kite farm simulation, an optimal single kite flight path was determined for the 3D flight path simulation. The optimal path will produce the highest power, since spacing is not a consideration for a single kite system. The focus will be on an 80 m^2 kite, since the current Kitepower trend is leading towards larger kite sizes and larger power production.

First, the effect of different Lissajous parameter variables was assessed, as it has not been previously evaluated in this simulation. The phi Lissajous parameter, corresponding to the figure-eight width, was evaluated from 0.1 to 0.45 and the theta Lissajous parameter, corresponding to the figure-eight height, was evaluated from 0.1-0.2, since these values produced reasonable flight paths which were within the limits of experimental flight data for smaller kite sizes. It was determined that increasing the theta Lissajous parameter generally decreased the power output, and a similar trend was found for the phi parameter. This correlates with results from previous path studies [21] which suggest shorter figure eight maneuvers produce more power, since they fly in the high power generation area (closest to the center of the figure-eight) more often. More time spent near the center of the figure-eight should produce a higher power, but would likely have high losses in turning, including sideslip and kite deformation. Including a loss factor for these situations would improve the traction phase simulation, but it is difficult to characterize and would require further research. However, the optimal phi Lissajous parameter had a value of approximately 0.15, and the optimal theta parameter had a value of 0.1, indicating that too narrow figure-eight maneuvers decrease power production as well without any turning penalty factors. The Lissajous parameter results for an 80 m^2 kite, with the input parameters defined in Table 4.4, can be seen in Figure 4.12.

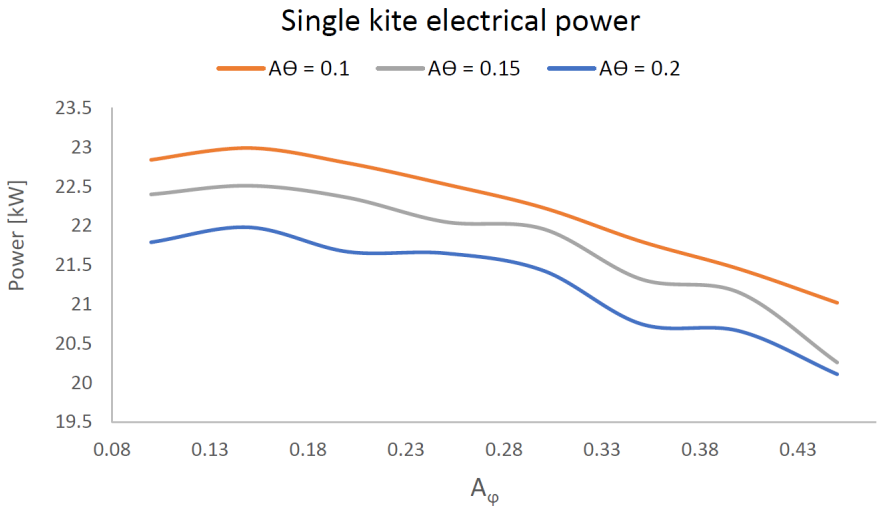

Figure 4.12: Lissajous parameter effects

If a small Lissajous variable is to be used in the kite farm simulation, especially for a larger kite size, the ability of the selected kites to produce this maneuver should be verified experimentally. Since this cannot yet be verified for an 80 m^2 kite, conservative values will be utilized to be consistent with experimental Lissajous values from smaller kites. Minimum Lissajous limits of slightly less than the average experimental Lissajous values, as estimated in Figure 4.11, will be utilized, with a lower theta parameter limit of 0.1 and a lower phi parameter limit of 0.35 for an 80 m^2 kite. The lower phi parameter limit was slightly more conservative than that of the theta parameter, since the phi parameter more strongly affects power output. Although a phi parameter value of 0.15 would be more optimal, a value of 0.35 is utilized to maintain a conservative estimate of turning capabilities for an 80 m^2 kite. As can be seen in the graph above, higher power outputs may be achieved with smaller figure-eight maneuvers, but the maneuverability of the kite should align with whichever parameters are selected. Although these smaller figure-eight shapes results in a higher power density, they could potentially add losses in traction, since quick turning maneuvers may deform the kite. Currently constant lift and drag coefficients are used during traction, but with quick turning maneuvers, this may not be the case in reality. Again, additional studies should be conducted in this area to evaluate and effect on the actual power output when flying shorter and narrower figure-eight maneuvers.

The operational angles were evaluated as well for an optimum with the 80 m^2 kite with a maximum power output at an azimuth angle of 1°. This is assumed to be the case since the kite paths begin towards the left side, in the positive azimuth angle, and therefore end with a slightly larger traction loop on the left side, slightly shifting the optimal azimuth towards the left as well. The complete results

are shown in Figure 4.13. There was a small deviation from the results of the simulation run with an azimuth of 0°, having little effect of the path flown or power output, with a change in power of less than half a kilowatt. Evaluations of the elevation angle revealed an optimal power production at an elevation angle of 19° for the system, and the average power results from different elevation angles are shown in Figure 4.14. From matching the simulated path to experimental data, a speed ratio of 5.5 and a maximum speed of 13 m/s was selected since it yielded the best match in paths. Therefore, these values were not evaluated for values which yield maximum power production. These values also have a small effect on the power production, yet a significant effect in matching the flight path spatially. Since these values are dependent upon the mechanism of the winch system, they can be altered and achieved with appropriate components.

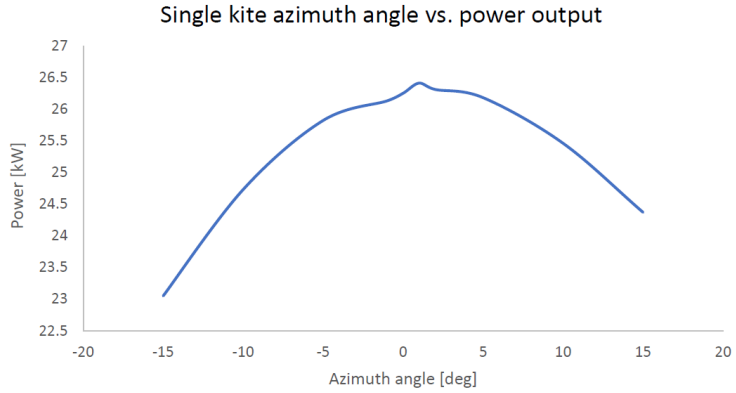

Figure 4.13: Single kite azimuth vs. average cycle electrical power

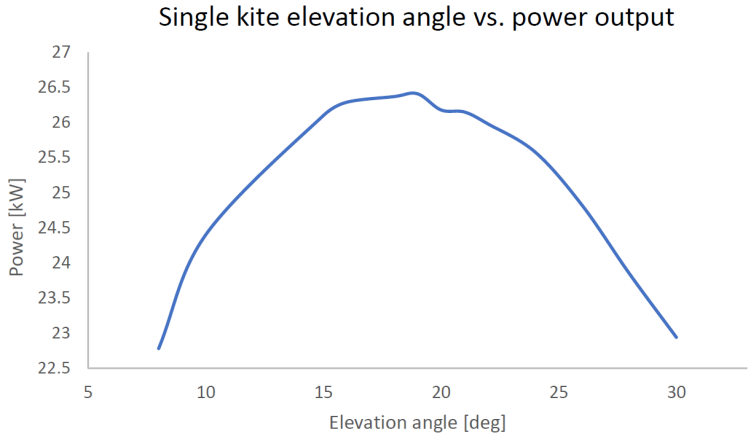

Figure 4.14: Single kite elevation vs. average cycle electrical power

The effect of the maximum and minimum tether lengths were also evaluated for the 80 m^2 kite. The maximum tether length was varied from 300-900 meters, and the minimum tether length was varied from 100-800 meters. It was determined that for the 80 m^2 kite, a difference of at least 100 meters between the maximum and minimum tether lengths would be needed to fly at least one complete figure-eight maneuver. Therefore, the larger the difference in maximum and minimum tether lengths, the more figure-eight maneuvers flown. A minimum tether length of 300 meters was found to produce the highest power for most or all maximum tether lengths. The maximum tether length seemingly had no optimal value and continuously increased the average cycle power as the maximum tether length increased. Because of this, and to create a more realistic flight path, the ”optimal” value for the maximum tether length was selected as 700 meters since it often yielded a high average cycle power, although it would not produce as much power as with the 900 meter maximum tether length. But, this

difference in power is less than 1 kilowatt, so it is seen as a reasonable selection. Flight paths with such a long traction phase have not been verified experimentally, so a more conservative path was utilized here.

For the 80 m^2 kite, the "base case" flight path is described as the single kite system which uses the optimal flight parameters described above. These are summarized in Table 4.4 and provides a path which produces an average electrical cycle power of 26.53 kW. Using the restricted area requirements (described in the following chapter) with a radius of 30 meters, the used land is taken as a 60 meter by 60 meter square, since the fencing would likely take this shape as opposed to a circular shape. This results in quite a high power density of 7.37 W/m^2 for a single kite. A single unit, however, will require a storage method or grid connection as well to supply energy for the retraction phase. The aerodynamic model of the kite features constant lift and drag coefficients in each phase and is the same for all kite sizes because limited data is available of actual values during flight, since it is difficult to measure directly. Additional analysis into these parameters could potentially improve the model's accuracy.

Table 4.4: Optimal 80 m^2 single kite parameters

Input Parameter	**Value**
r_{min}	300 m
r_{max}	700 m
β	19°
ϕ	1°
Speed ratio	5.5
v_{max}	13 m/s
F_{out}	21,554 N
F_{in}	3,212 N

All force and wing loading values are outlined in Table A.1 in Appendix A for several kite sizes. It can be seen that the traction and retraction forces increase linearly with increasing kite size. Additionally, based upon current experimental results, it is expected that larger kites can sustain a higher wing loading than smaller kites. Current tests with smaller kites provide a upper wing loading limit of about 400 N/m^2, whereas the estimated value for the larger kites is 800 N/m^2. These values are updated accordingly for increasing kite area, but it was found that the wing loading was typically not a limiting factor for a single kite operation within typical operating conditions. The retraction and traction forces, however, impact the system's flight significantly, causing incomplete path simulations when force values are too high or low. Additionally, if the traction force limit is to low, the kite will not fly optimally during traction, since it must be depowered to decrease the tether force.

5

Kite Farm Development

To move from a single kite system towards a farm configuration, a simple two kite farm was initially developed before expanding to larger triangular and rectangular configurations, based upon the simulated flight path described in the previous chapters. Since small scale farms are more realistic in the immediate future, only a few layout types were considered to keep the analysis simple. Specific cases were selected to analyze the results for each layout type in the following chapters, focusing on smaller systems initially. However, the created simulation can additionally be used to analyze larger kite farm systems.

5.1. Farm spacing considerations

Unlike the single kite simulation, a kite farm simulation quickly becomes complicated when adding unique flight envelopes for each kite. After a simple 2 kite system with similar flight paths was created, each kite's flight envelope was then manually defined with several input parameters. From there, systems with different flight envelopes were then evaluated. Several parameters were utilized to modify the flight paths such as varying azimuth or elevation angles, which could allow for closer ground station spacing. With many kites and therefore many operational envelopes, these kite farm systems can require complex individual control strategies if the spacing between units does not have a high factor of safety, as well as an overall farm control system. A farm control software would monitor the distances between kites in real time and implement collision avoidance maneuvers in extreme cases or adjustments for unplanned path deviations. This development of this control system would be a lengthy process, so is assumed that no farm control is implemented for this simulation, and that each kite will be simulated without a real time controller.

A kite collision or tether entanglement in a kite farm system can cause safety issues while also damaging the system components, so it is crucial to keep the kites within a safe operating distance from other nearby kites. This will be done by adjusting the kite flight paths and evaluating the distances between adjacent kites and tethers. Since safety and reliability are the main focuses of creating a farm system, the total power output and stabilization will come as secondary parameters, as these values define the economic viability of the system.

Starting with a simple 2 kite farm system provides a starting point for the analysis. With just two kites, there are two extreme operational cases which depend on the angle of alignment with the wind: wind-aligned and wind-perpendicular. These two orientations are illustrated in Figure 5.1, which show a top and side view of a two-kite system, respectively. The grey triangular areas mainly represent the traction flight envelope, since in retraction the kite flies upwards towards the zenith, which is not explicitly depicted here. The wind-perpendicular orientation generally allows for closer spacing, because the only overlap between operational envelopes occurs during the traction phase when the figure-eight maneuvers are flown. If the kites are in phase, or not phase shifted, the ground station spacing can be relatively small since the flight paths should maintain a near constant distance between the kites as long as wind conditions are not extreme. For the highest factor of safety, one would want the operational envelopes to be completely separate with no overlap, and maybe even additional spacing, as seen in the figures below which represent the methods used in the previous kite farm spacing analysis

in [13]. With the previous analysis methods, the in-line, or wind aligned, configuration was analyzed, as this represents the worst case scenario. For this orientation, there is a higher chance of collision or tether entanglement due to close positioning during all phases. For example, when both kites are nearing the end of the traction phase, the kites may still be quite far apart, but the upwind kite could be near the tether of the downwind kite, and a strong gust could cause safety issues if the spacing is not sufficient. With an effective control system, the kites can possibly be placed closer together without entangling, but this is yet to be developed. It is assumed that the ground stations will not be moved once implemented, so all wind directions should be considered for each layout type. Designing for the worst case scenario will ensure maximum system functionality during typical environmental conditions, and will result in a higher performance for the best case scenario conditions.

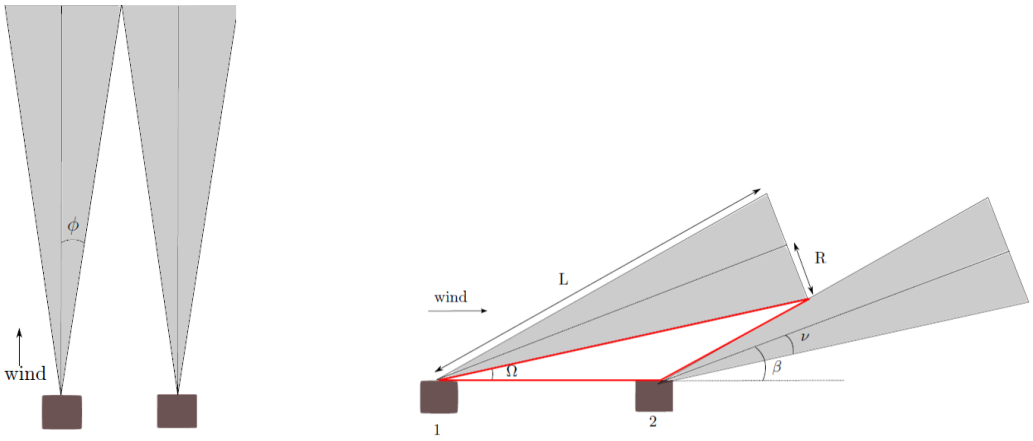

(a) Wind-perpendicular [13] (b) Wind aligned [13]

Figure 5.1: Kite farm wind alignments

In the previous kite farm spacing analysis, two minimum spacing distance equations, Equation 5.1 and 5.2, were utilized to calculate the minimum required spacing between kite ground stations for a wind-perpendicular and wind-aligned system, respectively. This minimum distance required between kite ground stations, d, was derived for two similar kite systems which would operate with the same flight path and envelope, as seen in Figure 5.1, assuming no overlap between adjacent flight envelopes.

$$d = 2r_{max}\sin(\phi) \tag{5.1}$$

$$d = \frac{r_{max}}{\sin(\beta - \upsilon_1)\left(\frac{1}{\tan(\beta-\upsilon_1)} + \frac{1}{tan(\upsilon_1+\upsilon_2)}\right)} \tag{5.2}$$

where r_{max} is the maximum tether length, ϕ is half of the operational envelope in the azimuth direction, β is the average elevation angle for traction, υ_1 is half of the operational envelope angle in the beta direction of the upwind kite, and υ_2 is half of the operational envelope angle in the beta direction of the downwind kite. These angles and lengths are illustrated in Figure 5.1 and it is assumed that both kites operate at the same elevation angle. If both systems are assumed to have the same operational envelopes, υ_1 and υ_2 are the same.

In Figure 5.1a, the grey area represents a top view of the area utilized by the kites in the azimuthal direction over one complete cycle. It can be seen that this wind alignment could be beneficial for smaller kite spacing as long as the azimuth angles are not too large. In Figure 5.1b, the grey area represents the area utilized during traction, but the kites will reach much higher elevation angles during retraction and will create larger flight envelopes. Only the traction flight envelope is analyzed because the corresponding distance equation assumes no phase shifts for wind-aligned systems, and the retraction and transition paths are less complex and pose less risk of collision. These distance equations are valid as long as the kites fly approximately the same flight path, but no longer hold true if staggered or overlapping flight envelopes are utilized. Additionally, these equations may not

apply properly if a phase shift is utilized. These equations were updated for use with dissimilar flight envelopes, as shown in Equations 5.3 and 5.4, and used to compare the results from the previous kite farm model to the simulated results from this analysis.

$$d = r_{max,1}\sin(\phi_1) + r_{max,2}\sin(\phi_2) \tag{5.3}$$

$$d = \frac{r_{max,1}}{\sin(\beta_1 - \upsilon_1)\left(\frac{1}{\tan(\beta_1-\upsilon_1)} + \frac{1}{tan(\beta_2+\upsilon_2-\beta_1-\upsilon_1)}\right)} \tag{5.4}$$

where $r_{max,1}$ is the maximum tether length of the upwind or leftmost kite, ϕ_1 is the half azimuth envelope of the upwind kite, $r_{max,2}$ is the maximum tether length of the downwind kite, ϕ_2 is the half azimuth envelope of the downwind kite, β_1 is the average traction elevation angle of the upwind kite, and β_2 is the average traction elevation angle of the downwind kite.

With the previous methods, it is assumed that the systems' operational envelopes do not overlap, making the safety factor quite high. While a wind gust could potentially decrease the distance between the kites, it is assumed that the distances calculated with the model below should provide a sufficient safety margin. This will be considered when comparing the distances from the newly created simulation. In this analysis, the elevation and azimuth angles will be greatly varied to see the effect of staggering or overlapping kite operational envelopes. While this could allow closer spacing, it could also decrease the power output of one or both kites if it deviates from the optimal operational conditions. Additionally, the operational envelopes can overlap significantly more if there is a phase shift, but this is not ideal for kites aligned with the wind, since there is a higher possibility of entanglement. For kites arranged perpendicularly to the wind direction, a phase shift has less impact, since there is less opportunity to fly in the same airspace. [13]

5.2. Analysis Parameters

In a simple, idealistic kite farm operation, all kites would utilize roughly the same operational envelope during operation to fly a similar path. Modifying this operational envelope for each kite could allow closer kite spacing in a farm layout, since the envelopes can be staggered, or even overlap each other with the introduction of a phase shift or a farm control system. However, in actual flight events, the path flown can vary significantly even when the same control system is used, as seen from experimental data. This means that each kite, as well as the farm system, should have sufficient control to ensure that each kite flies within a certain tolerance of its prescribed path. Alternatively, the kites within a farm should have more than sufficient spacing to ensure that all units will not fly too closely to other units. Developing control systems is a computationally intense process, so the focus will be on modifying individual kite paths through their operational parameters in order to achieve sufficient spacing between units. The impact on the power production will additionally be assessed to see the effects on total power production and power stabilization for different flight path arrangements. All parameters that will be modified for this analysis are outlined in Table 5.1. Each kite's operational envelope will be designed uniquely for each system to evaluate all possibilities with different layout types.

Table 5.1: Variables modified in kite farm analysis

Parameter
Kite area (A_{kite})
Phase shift (C)
Azimuth angle (ϕ)
Elevation angle (β)
Min. tether length (r_{min})
Max. tether length (r_{max})

As previously mentioned, for a kite farm, the highest collision risk occurs when the kites are aligned with the wind, since there is not longer a constant distance between adjacent kites and tethers. This is

illustrated in Figure 5.2, where a two kite system without a phase shift is used to highlight the situation of interest. In the figure below, the variable x represents the minimum distance from one kite and its tether to the adjacent kite and its tether. For maximum safety, this value should be high, but allowing it to be within a certain range can decrease kite farm spacing requirements. When using the same flight path for two in-phase kites, the distance between the kites stays the same, equivalent to the distance between the ground stations, but the value of x is not constant. Unlike with the wind-perpendicular alignment, the distance between the tethers and the kites is not always the same as the distance between ground stations. While both kites are in the traction phase, the distance between the upwind kite and the downwind tether can be quite close. The closer to the ground that the kites fly, or the lower the elevation angle, the smaller the distance between the upwind kite and downwind tether during traction.

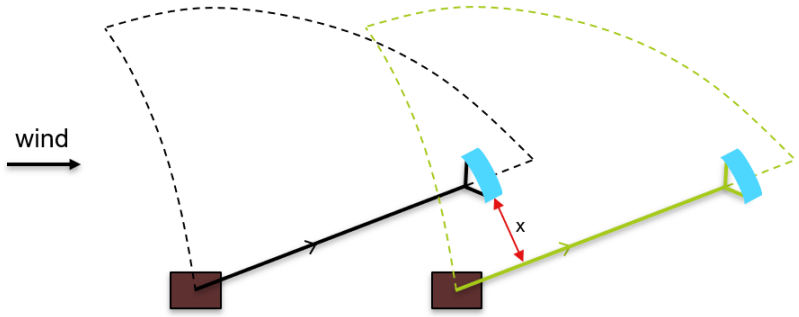

Figure 5.2: In-phase wind-aligned kite complications

Including a phase shift in adjacent kites introduces additional complications. With phase shifts for wind-aligned systems, there are several time periods which would be of high importance for collision avoidance. One significant period of interest would be when an upwind kite is in traction or the beginning of retraction and the downwind kite is in transition or nearing the end of retraction. Figure 5.3 illustrates this issue, showing that there could be a tether entanglement if a phase shift causes this situation to occur. For this reason, any applied phase shift should carefully consider the phase durations of each kite system. As demonstrated in the previous chapter, not all phases of the cycle have the same duration. The transition phase is typically the quickest phase, only a fraction of the traction duration, and the retraction phase is also typically shorter than the traction phase. With such a relatively long traction phase, the phase shift should be carefully evaluated as to avoid potentially dangerous situations.

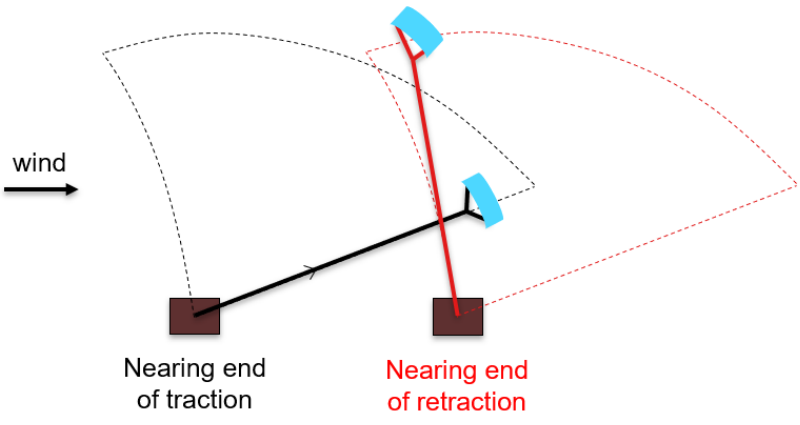

Figure 5.3: Phase shifted wind-aligned kite complications

For kites aligned perpendicularly to the wind, the spacing is mainly dependent on the width of the figure-eight flown during traction. If the two kites are in phase, they should be spaced sufficiently to

maintain a relatively constant distance between the kites during all phases, which is simple if the flight envelopes are similar. But, kites flown with a phase shift in this wind alignment are predicted to be less prone to collision risks. It is also predicted that for systems of any wind alignment, the operational envelopes can be adjusted to allow for potentially closer ground station spacing. A few conceptual ideas to shift the flight envelope are illustrated below. Figure 5.4 illustrates the operation of kites at different elevation angles, with a slight overlap of the flight envelopes. This allows the upwind kite to maintain further distance from the downwind system, but could potentially require one of the two kites to operate at a sub-optimal elevation angle, therefore decreasing the power output of that kite. Figure 5.5 shows an azimuthal shift in the flight envelopes, operating two kites at azimuth angles which are directed away from each other to allow for relatively close ground station spacing. Again, this could cause one or both kites to operate with a sub-optimal flight path and decrease power output. Therefore, the effect of each operational envelope parameter will be evaluated. In this simulation, all phases of the cycle are flown at the same azimuth angle, but in future simulations it would be interesting to add systems with a flight path that features different or changing azimuth angles for different phases.

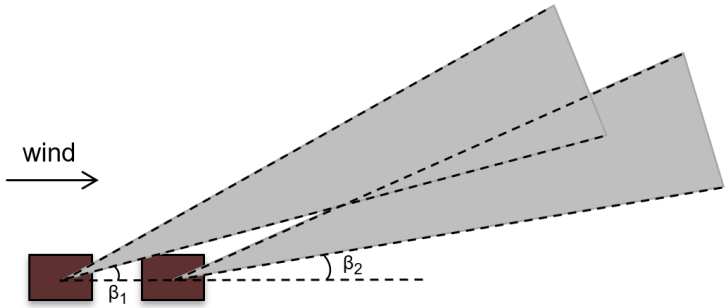

Figure 5.4: Elevation shift concept for wind-aligned kites

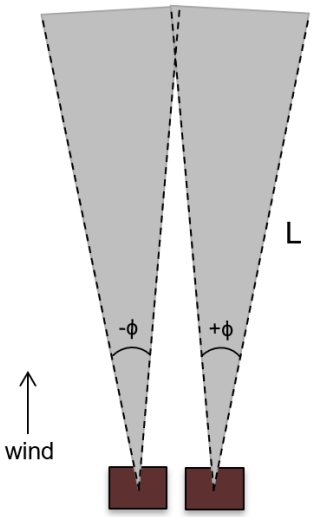

Figure 5.5: Azimuth shift concept for wind-perpendicular kite alignment

5.3. Kite farm layout and simulation

Before creating the kite farm simulation itself, an input module was developed to create the layout of each farm as a function of user input. Several parameters are specified to define the layout of the entire system, including the number of rows and columns, the alignment with respect to the wind direction, and if a phase shift is to be included. This module gives a basic visualization of the kite farm ground stations, and indicates the wind direction as well, and provides the utilized land area, which is used to

calculate the farm's power density. The kite farm power density is calculated slightly differently than it would be for a wind turbine farm, since the actual AWE area in use is difficult to define. It would be quite conservative to only use the area defined by the ground stations since the kites operate outside of these boundaries. For the Kitepower system, a fence will be placed around the limit of the "danger zone", or the restricted area, which signifies the boundary in which moving objects can still be during kite operation, including people or livestock. This is illustrated below in Figure 5.6 which shows the system's spacing guidelines. Using the fenced in area as the total utilized land area serves as a more appropriate estimate, although the airspace used above still exceeds these limits. Since these systems will not be placed near (within 300 meters of) permanent infrastructure, this limit is reasonable since the airspace would be unused otherwise and is only temporarily occupied by the AWE system. Using the radius of the complete operational area would yield quite low power density values, and would likely be an under-approximation of the system when comparing to traditional wind turbines, especially since the Kitepower system is expected to land within the danger zone during all flight conditions. Although, using the entire operational area radius would likely show that systems of more kites are more beneficial, since the kites can have overlapping operational areas if spacing is close enough. As kite sizes increase, though, the restricted and operational areas should be reevaluated since they could potentially require larger areas. Other analyses on AWE power density use the kite area as the utilized area, which provides a much higher power density, especially for smaller kites [5]. To be consistent with wind turbine power density calculations, the area used was selected instead to provide a concept of the land requirement instead of the airspace occupied with the kite.

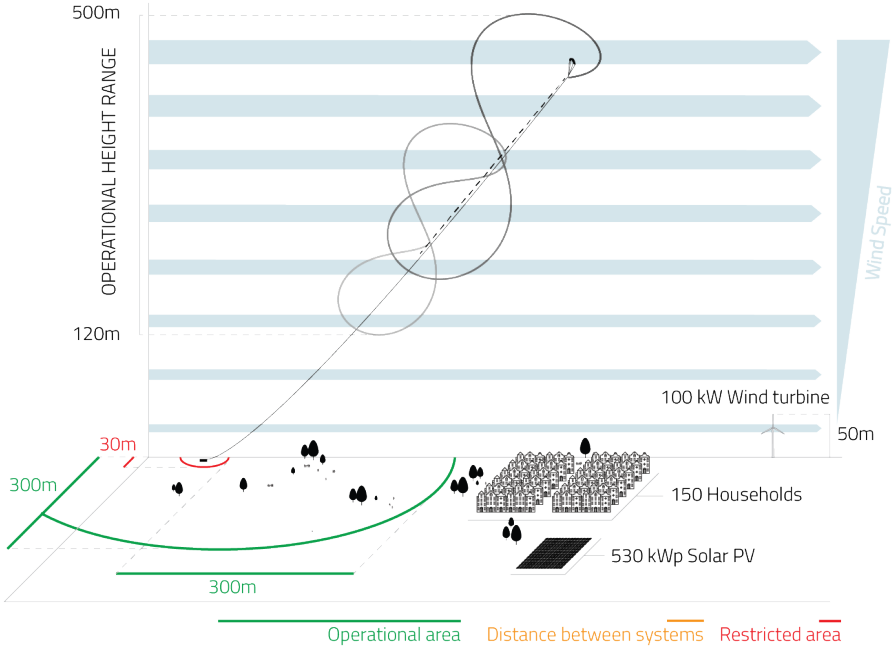

Figure 5.6: Kitepower surrounding area zoning [31]

Utilizing the kite farm layout module and the single kite simulation model as inputs, the kite farm simulation was developed. This module defines all individual kite flight paths, as specified by the user, and runs the single kite simulation for each kite at its own ground station. Once all kites in the farm have been individually simulated, the minimum spacing between units is calculated. The initial spacing values are taken as a function of tether width, requiring a distance of at least 2.5 times the kite width between all adjacent kites and their tethers. Since the simulation is a point mass model, represented at the center of gravity of the kite, half of the width of the kite actually extends past this point. To account for the worst case scenario, at least 1.5 times the kite width is expected to be needed between two airborne kites. Adding this to the two half kite widths provides a value of 2.5 times the kite width. A tether sag margin is also applied to account for the non-ideal tether in the simulated path. If the tether force is above half of the maximum force, as it typically is in traction and transition, the tether is assumed to be nearly straight. For this case, the tether sag margin is also set to require 1.5 kite widths between tethers at all points along each tether. When tether force is low (under half of the traction

force), as is typical with the retraction phase, a larger tether sag margin is applied which requires 3 kite widths between all points on each tether. This is to account for possible sag on both tethers, which could be significant and is not included in the simulated path. Without accounting for tether sag, the analysis results may be inaccurate, since an ideal straight tether is an acceptable approximation for times of high tether force, but would not be such a good representation during low tether force periods such as during retraction. Because of this, a higher fidelity tether model would increase kite farm simulation accuracy, but would also increase computational time.

A phase shift was implemented using the methods of [13], where the phase shift is a function of the total number of columns which are in the wind-aligned direction, as shown in Equation 5.5. Here C represents the phase shift in seconds, T is the cycle duration of a single kite unit, and N_c is the number of wind-aligned columns or rows. This equation is based upon kite farm operation in which all kites fly a similar path, and therefore have the same cycle duration. Utilizing different flight paths for kites in the same farm could result in a unique cycle duration for each kite, making it difficult to characterize a phase shift between kites. The time difference between cycles of phase shifted units would be continually changing. To account for these irregular patterns, the kite farm simulation runs three cycles for each kite, as it was determined that the patterns typically repeat for most flight path combinations within three cycles.

$$C = \frac{T}{N_c} \tag{5.5}$$

Utilizing the safety values based upon kite size, the kite farm simulation evaluates for any interaction between the kites or tethers at all time steps. For the kites, the distance between any two adjacent kites can be directly calculated. To evaluate for tether collision, linear functions are created to represent the tethers as straight lines from the ground station to the kite position, as shown in the equations below. The ground station location is represented with p_1 for the first unit and p_2 for the adjacent unit. The direction vector, $\vec{u}$, is calculated from the kite position to the ground station for each unit. The variable λ corresponds to specific positions along the line function. For each time step in the simulation, if the minimum distance between the two units, including the tethers, falls within an acceptable range, the simulation continues until a complete cycle is completed. If the distance between two units is below the safety ratio values previously described, the spacing between the ground stations is increased until all units comply with the safety ratio values. The results of this analysis strongly depend on these tether sag factors, so these can be adjusted to increase or decrease ground spacing, but precise control and modeling of the systems should also be used.

$$\vec{L_1} = \vec{p_1} + \lambda_1 \vec{u_1} \tag{5.6}$$

$$\vec{L_2} = \vec{p_2} + \lambda_2 \vec{u_2} \tag{5.7}$$

The minimum distance between any two lines occurs when the dot product of a certain vector between the two lines, $\vec{PQ}$, with both directional vectors is equal to 0, i.e. the vector is perpendicular to both lines. The λ values for each line can then be solved for from these two calculations, and then substituted into the following function for a vector between the two lines [32].

$$\vec{PQ} = \vec{L_2} - \vec{L_1} = p_2 - p_1 + \lambda_2 \vec{u_2} - \lambda_1 \vec{u_1} \tag{5.8}$$

For each farm system, the average cycle farm power is calculated from the sum of the power of all individual kites over one average cycle duration. If the cycle durations of the kites are dissimilar, the average of all cycle times is utilized. The power density is calculated by dividing the average cycle farm power by the utilized land area. The instantaneous power is shown over one average cycle duration, and sums all instantaneous power values to provide one system power at each time step.

For an applied use of the kite farm simulation, two specific case studies will be conducted to evaluate for the optimal operational envelopes and power generation values. These cases include a two and three kite system to allow for an in depth analysis on the direct effects of each kite's flight envelope on instantaneous power and power density. These cases evaluate small scale AWE farm systems which would produce power similar to that of small to medium scale wind turbines [33]. Additional results for larger kite farm simulations will also be discussed later. The simulation tool can be used for even larger scale systems, and also with larger kite sizes, to compare large scale kite farms to larger scale

wind turbines or utility scale wind generation. The kite farm systems will be compared to a single kite system, and to current renewable energy technologies to evaluate the technical potential. The goal of these case studies is to find the minimum spacing between the kites for each combination of flight envelopes, and then to find the combination of flight paths which produces the maximum power density, while also considering power stability.

6

Case A: 2 kite system

Analyzing a two kite farm system allows an in depth analysis of a basic system before continuing with more complex analyses. Figure 6.1 illustrates the complete cycle paths for two wind aligned kites, with similar flight paths. With just two kites, the flight path parameters can be extensively modified to model unlikely flight paths for single kite systems and to evaluate for any unexpected yet beneficial operational points. These systems will include kite paths which deviate from the optimal single kite flight path in order to avoid collisions in a tightly packed area. This case will focus mainly on wind aligned and wind perpendicular systems to analyze the least and most ideal wind direction situations. The simulation verified that wind directions between these extremes yield intermediate results, so they are not analyzed further, but can be useful for determining performance of an installed system with wind direction changes.

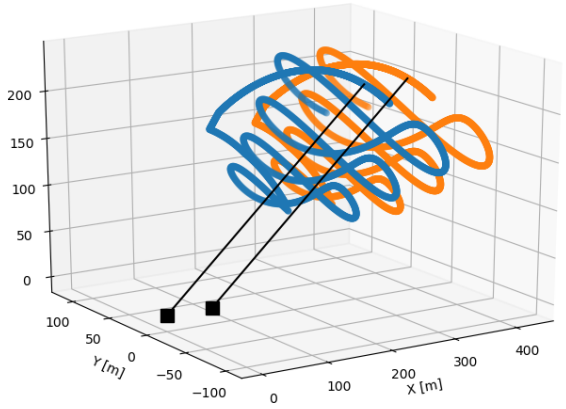

Figure 6.1: Two kite wind aligned system

To provide a baseline for comparison with all results, the two kite system was initially run with the ”base case” flight path for both kites. This resulted in a power density of 3.75 W/m^2 for a two kite, wind aligned system with a ground station spacing of 175 meters. With the same wind alignment, and an added phase shift, these values change to 1.51 W/m^2 and 525 meters. For a wind perpendicular system, the power density is 7.34 W/m^2, which is the same as the single kite system. For this two kite system, the required spacing between units is 60 meters, which is equivalent to having two single kite systems with a 30 meter restricted area radius. For this wind alignment with the phase shift, the values are 3.15 W/m^2 and 220 meters.

6.1. Kite area effects

A range of kite areas were assessed with the two kite farm, utilizing the base case flight paths, to see the kite area effect on power, power density, required ground station spacing. Since the spacing between ground stations is related to a safety factor which is dependent upon kite size, larger kites should have a larger distance between ground stations. If this safety factor was to be kept as a constant value instead, the increase in the power density would become even larger with increasing kite area. The results of these simulations are shown in the figures below. In Figure 6.2, the average single cycle power and power density values are shown, and the results are further detailed in Table B.1 in Appendix B. The power produced is independent of the wind alignment if the flight envelopes are the same, so just one power result is shown and it is clear that the average cycle power increases linearly with increasing kite size. It can also be seen that a wind aligned system has a significantly lower power density than that of the wind perpendicular system for each kite size. This difference grows larger for larger sized kites, indicating that smaller kite farm systems may have better applications for locations in which the wind rose is less concentrated in one direction. The wind aligned power density values seem to raise more slowly at larger kite sizes, suggesting a possible power density limit at at larger kite sizes. The wind perpendicular power densities indicate that there may be a power density limit as well, but at a much larger kite size. Therefore, a wind perpendicular system with a large kite area would be greatly beneficial for a location with a strong wind direction probability in a certain direction. Since power is a function of the number of kites and the flight path, it is assumed that there is no area limitation to this, but larger kites may need to fly larger traction paths, utilizing longer tether lengths to provide longer traction durations.

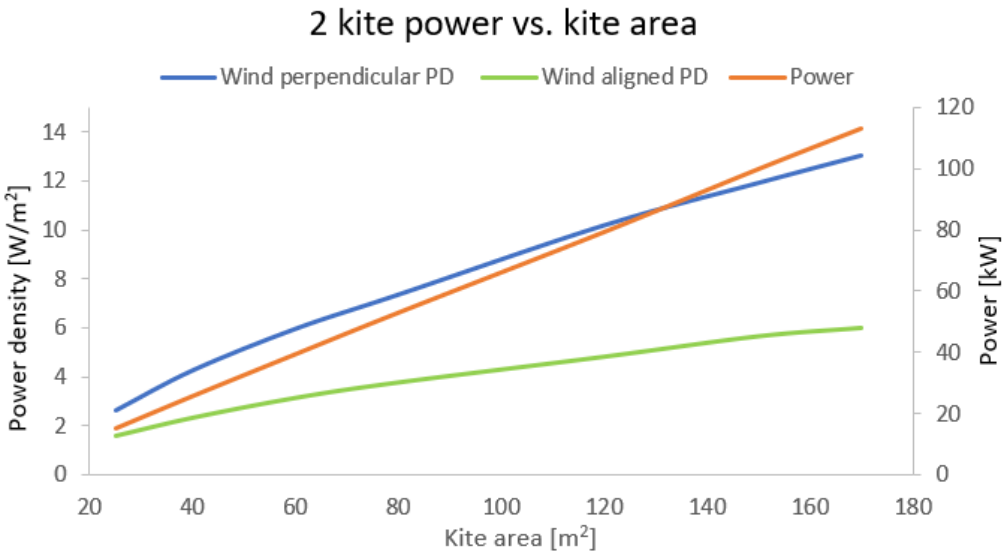

Figure 6.2: Two kite power and power density vs. kite area

As previously discussed, smaller kite sizes can allow closer ground station spacing. Both wind aligned and wind perpendicular systems produce a the same average cycle power, but the wind aligned system has a lower power density due to closer ground station spacing. Therefore, the power density curves show the great difference in ground station spacing requirements. The required ground station spacing exhibits almost logarithmic behavior for the wind aligned system and a slightly more linear behavior for the wind perpendicular system. Additionally, the shortest distance reached between airborne components of the two units was analyzed as well. This indicates how close the two tethers or kites were to each other in the air during any point of operation throughout one complete cycle. The shortest distances which were reached for each system type are shown in Figure 6.3. The ”spacing” refers to the required ground station spacing, while the ”minimum distance reached” refers to the shortest distance achieved between airborne components during operation. Wind aligned systems require much larger spacing between units, but the distances reached between airborne components is quite similar for both wind alignments.

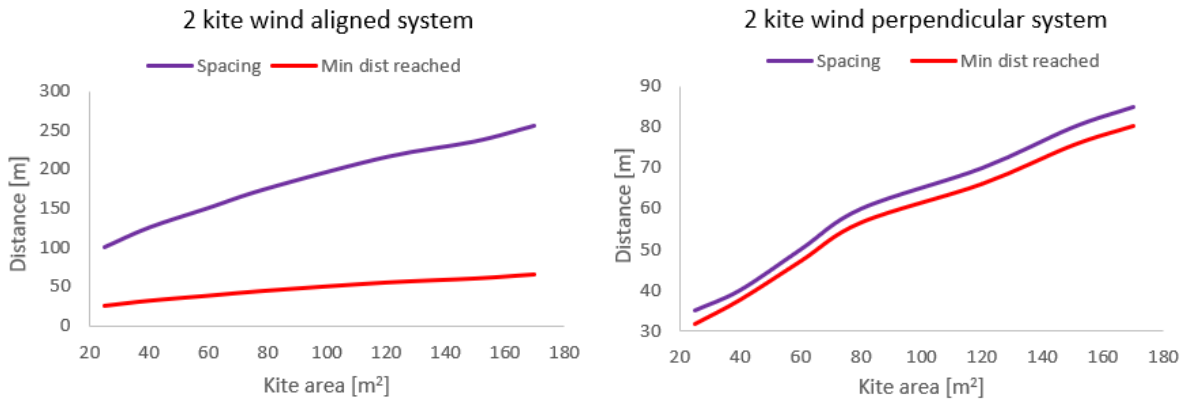

(a) Wind aligned (b) Wind perpendicular

Figure 6.3: Two kite shortest distance between all airborne components vs. kite area

6.2. Phase shift effects

With the introduction of a phase shift, the ground station spacing increased significantly for any wind alignment. With a wind aligned, two kite base case system, the spacing requirement goes from 175 to 525 meters with wind aligned units. For the wind perpendicular systems the change is less drastic, but still significant, with the required spacing requirements going from 60 to 220 meters with the introduction of a phase shift. It is assumed that this results from a high power density with kites of the same flight path, and any deviation in this path actually introduces additional spacing requirements for a multi-kite system. Even a small phase shift makes the kite farm less space efficient, indicating that a phase shifted system may require additional kite control and path planning for optimization. However, the main benefit of phase shifted systems is the potential to levelize the instantaneous power. Since the retraction phase requires energy input, systems without a phase shift may have a higher power density but will also require costly storage units or grid energy to meet the demand during the retraction phase. A phase shift would allow the system to be entirely independent, with the exception of any startup energy that might be required.

Figure 6.4a shows the instantaneous power of the two kite base case simulation with no phase shift, while Figure 6.4b includes a phase shift. These results are the same for either wind alignment since wind alignment does not affect the power output, just the spacing requirements. Since the two kites have the same flight envelopes, they have the same cycle duration and maintain a constant phase shift over time. It can be seen that the phase shift improves the instantaneous power output, decreasing the difference in power output when compared to the non-phase shifted case. There are also two periods of time when both kites are in traction, which produces a higher power output for approximately 20 seconds. This can be smoothed out and tuned by adjusting the flight path and system parameters to modify the phase durations. This could produce a more constant power value if the two kites are never in traction simultaneously, but will likely decrease the total average cycle power. The large, quick spikes in power are caused by the lack of a simulated ground station. In reality, there would be a reeling limit determined by the selected components, but this is not modeled in the simulation, and a rapid change in reeling speed causes a power spike. This could be mitigated with the implementation of a controller in the kite farm simulation, but due to time constraints, this will be left for further improvements. Further phase shifted results are shown in Figures 6.5 and 6.6 for the wind aligned and wind perpendicular systems, respectively. These figures show the distance between the kites over a single cycle as well as the closest distance along each tether reached between the two base case units. For comparison, the distances between the units for the base case two kite system with no phase shift are shown in Figure 6.7. Using the phase shift formula previously described, the two kite system features a phase shift of half of its original cycle duration, placing the downwind kite in traction while the upwind kite begins retraction. Initially, this allows for an increasing distance between the airborne components, but becomes a concern at a time of about 200 seconds, as the upwind kite enters the traction phase and the downwind kite is in retraction. A smaller phase shift could potentially mitigate this issue, but still produces a smaller power density than a system with no phase shift.

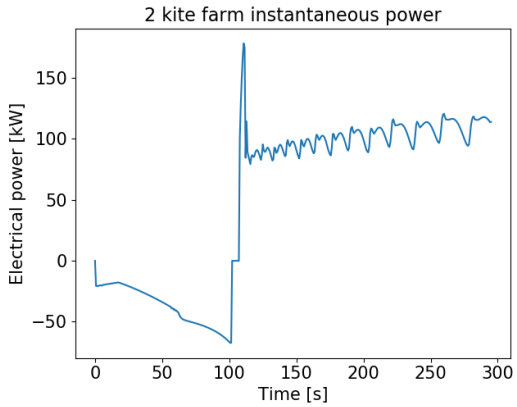

(a) No phase shift

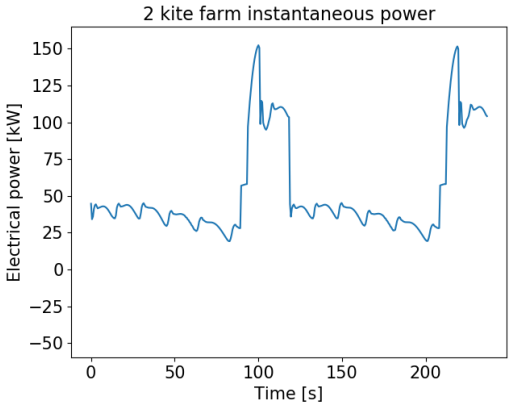

(b) Phase shift

Figure 6.4: Phase shift effect on instantaneous power

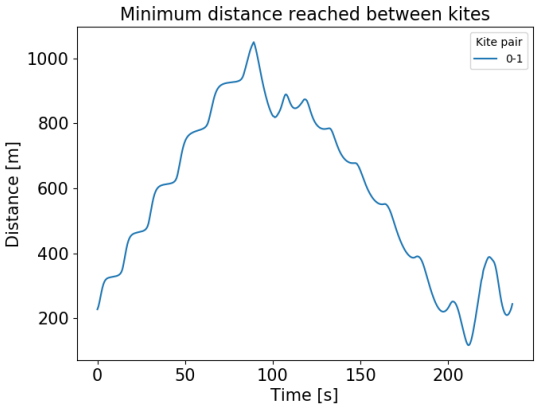

(a) Distances between kites

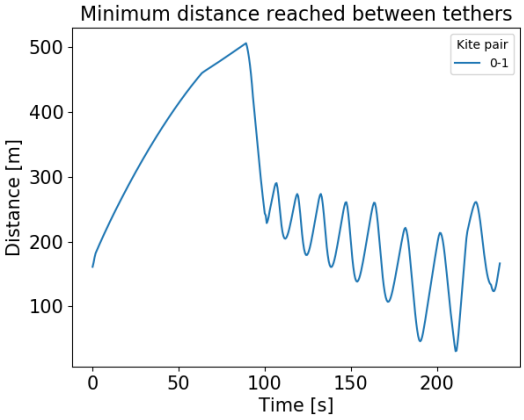

(b) Distances between tethers

Figure 6.5: Two kite (wind aligned) phase shift effects on distances over one cycle

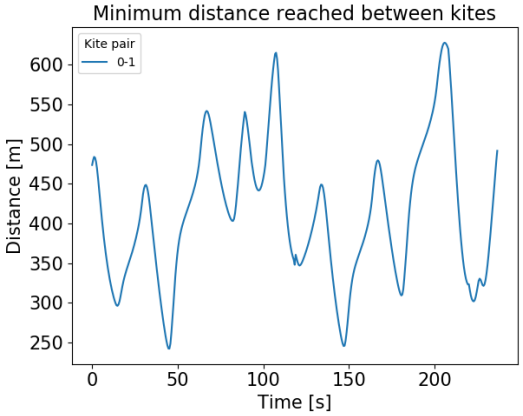

(a) Distances between kites

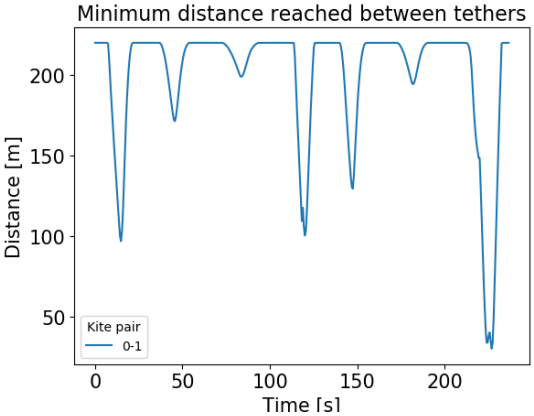

(b) Distances between tethers

Figure 6.6: Two kite (wind perpendicular) phase shift effects on distances over one cycle

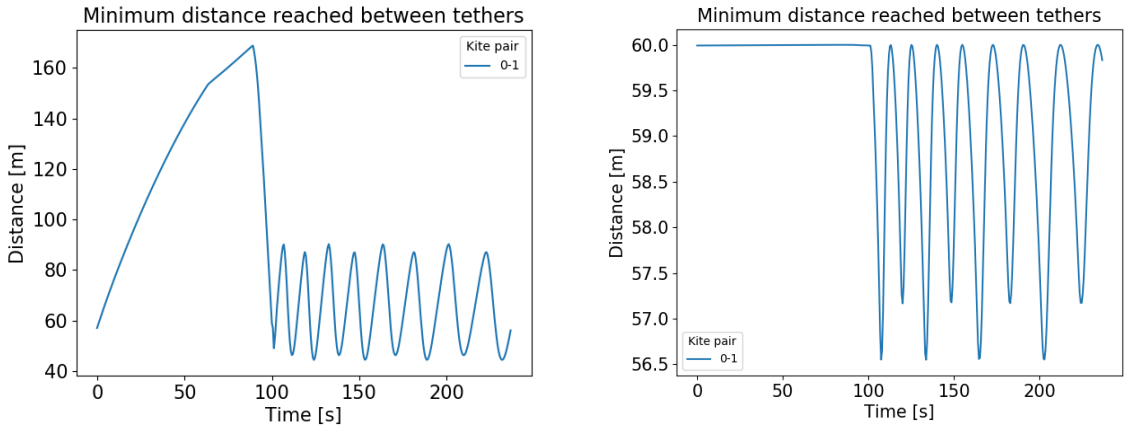

(a) Wind aligned

(b) Wind perpendicular

Figure 6.7: Two kite base case tether distances over one cycle

For the non-phase shifted system, the distance between kites remains constant, with the same value as the distance between ground stations, over the entire cycle, so it is not plotted here. These values are 60 meters for the wind perpendicular system, and 175 meters for the wind aligned system. The distances between phase shifted kites are often greatly larger than without a phase shift, indicating an extremely high probability of non-collision for times with such great distances between kites. Similarly, with the distances between any point along either tether for the wind aligned systems, in Figures 6.5b and 6.7a, the graphs show a similar shape, but the range of the phase-shifted system is much larger. The phase shifted system reaches much closer and farther tether positioning as well. This shows some promise for a phase shifted system if this lower extreme distance could potentially be mitigated with a control system or constant width figure-eight maneuvers, which is not the case with this simulation, since the experimental flights exhibit constant angle flight envelopes more clearly. Constant width figure-eight maneuvers could, however, potentially increase variation in power when both kites are in traction, since the power output is often cyclical throughout traction, and would be amplified with additional synchronized kites. Additionally, narrower figure-eight maneuvers would potentially decrease the distance between tethers as well, since the tethers are farther from the other unit's ground station. But, the large distance between the tethers in the phase shifted system, until about 190 seconds into the cycle, indicates a higher factor of safety when compared to the non phase shifted system. Overall, the phase shifted system shows larger distances between units, however, this is mostly due to a much larger ground spacing, which decreases the power density. No change in the phase shift value showed a solution to this issue. This would be an interesting area of interest for future research, especially in combination with a farm control system.

6.3. Azimuth angle effects

From the single kite flight path, it was found the the operational azimuth angle for the base case was limited within the range of -36° to 29°, since the kites cannot operate at too high of a deviation from the wind direction. Here, a negative azimuth angle indicates a shift towards the right of the wind direction, while a positive azimuth angle indicates a shift towards the left of the wind direction. The asymmetry in this azimuth range likely occurs because the traction path begins towards the positive azimuth direction and the maximum tether length results in the largest and final traction loop to be in the positive azimuth direction. Therefore, it seems that the path flies further in one azimuthal direction than the other, so the kite should operate more towards the negative azimuth for this path. The opposite of this azimuth range should apply if the traction path were to start towards the negative direction instead. When the kites operate far from the wind direction, the power output generally decreases, sometimes using more power than is produced at wide angles. However, this creates a large distance between azimuth shifted systems, potentially allowing closer ground station spacing.

The two wind aligned systems showed quite different, yet slightly overlapping results, as displayed in Figures 6.8a and 6.8b below. To visualize the azimuth angle evaluation results, the upwind or

leftmost kite variable is plotted on the x axis, while the downwind or rightmost kite variable is plotted on the y axis, and the power density values are shown for each combination of these variables. A larger, bluer dot represents a high power density while a small red dot represents a low power density, as seen in the color bar in each figure. The maximum power density of the wind aligned, non phase shifted system resulted from an upwind kite azimuth of -26° and a downwind kite azimuth of 4°, with a power density of 4.78 W/m^2. The data shows that systems utilizing the same azimuth angle have reasonable power densities, but there are also higher values with larger differences between azimuth angles. However, if one or both kites fly close to the maximum azimuth angle limits, the power density decreases greatly because the power output decreases when the kite has an azimuth angle further from the wind direction. There highest power densities seem to results form moderate azimuth angles for each kite, with a reasonable difference between the two kite's azimuth angles. For the wind aligned phase shifted system, the maximum power density, with a value of 3.60 W/m^2, resulted from an upwind azimuth angle of -26° and a downwind angle of 19°. This is quite a bit lower than the highest power density of the system without a phase shift, but the spacing requirement only increases from 110 meters to 135 meters with the inclusion of a phase shift. The phase shifted results produce two areas of higher power density in the figure below, showing few azimuthal combinations which result in a high power density for this system type. The in-phase system shows many more azimuth angle combinations for higher power densities. The diagonal from the bottom left corner to the top right corner represents flight paths with the same azimuth angle, showing reasonably high values for the non phase shifted system, but quite low values for the phase shifted system. This means that wind aligned, phase shifted systems benefit more from dissimilar flight paths. The phase shifted results show more of a symmetric pattern than the non phase shifted system, showing an interesting asymmetry for the non phase shifted system. The asymmetry of the non phase shifted system indicates a strong effect of the individual flight path which is flown. It is assumed that certain azimuth angle combinations create flight paths which result in a phase shift-like effect, causing the kites to fly close together with certain flight paths. This could potentially be mitigated with alternate elevation angles or tether lengths as well to ensure adequate spacing between units. Some slight symmetry in this system indicates that a certain azimuth delta results in the optimal system. This delta is around 30° without a phase shift. The symmetry of the phase shifted system indicates that an optimal power density results from a delta in azimuth angles of about 45°, with the upwind kite azimuth around +26° and the downwind azimuth around -26°, or the upwind kite azimuth around -26° with the downwind kite azimuth around 19°. A slight difference in these optimal values shows that there is likely an improved power density from an azimuth value between 19-26° in the positive or negative direction. Due to computational time, intervals of 5° were used for this analysis, but the difference in the power density results near the optimal areas differ by no more than a few tenths in value for a difference of 1°, showing reasonable accuracy.

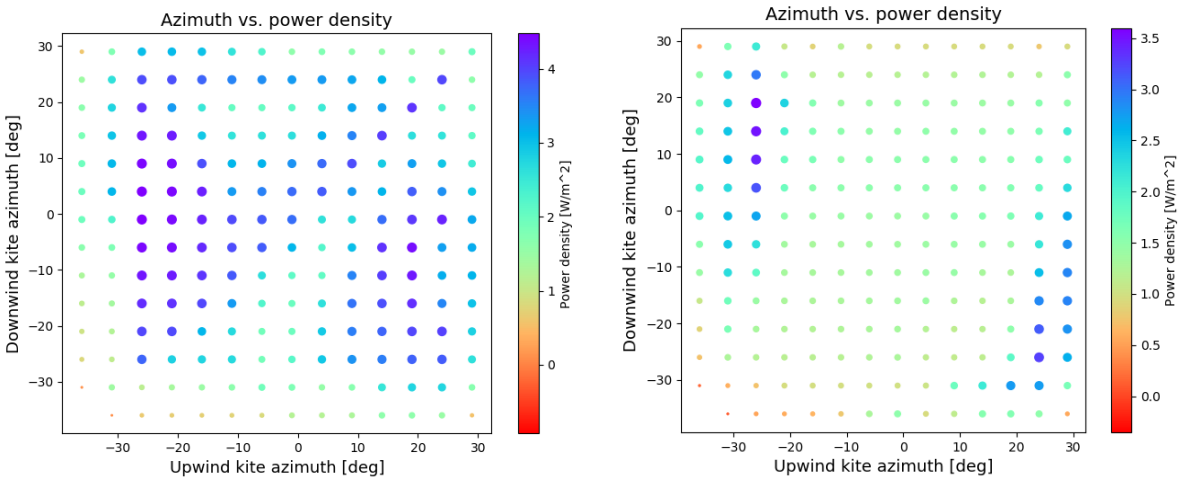

(a) No phase shift (b) Phase shift

Figure 6.8: Wind aligned system azimuth shift effects

For the wind perpendicular systems, the azimuth change results are visualized in Figure 6.9. These systems show much different trends, with higher power densities in a distinctly asymmetric way, indicating the presence of a single optimal azimuth pair. The wind perpendicular results also produce generally higher power density values, slightly less than twice as large as the wind aligned results. With the non phase shifted system, the maximum power density of 7.33 W/m^2 resulted from with both kites having an azimuth angle of 4°. Additionally, similar azimuth angles generally produced high power densities, until the angle was quite far from the wind direction, at about 25°. For the phase shifted system the maximum power density was at a left kite azimuth of 9° and a right kite azimuth of 11°, yielding a 7.06 W/m^2 power density. The power density difference between the phase shifted and non-phase shifted systems in this wind alignment is significantly smaller than with the wind aligned systems, further showing the benefit of wind perpendicular systems. The patterns for the power densities are also quite similar between both wind perpendicular systems, showing more ideal systems with the left kite at an azimuth around roughly -10°-20° and with a right kite azimuth angle between approximately -25°-0°. Several dissimilar azimuth systems also produced high power densities, but the phase shift-like effects of dissimilar envelopes seems to have a strong impact on the power density, therefore showing the benefit of little to no azimuth shift between kites for wind perpendicular systems. As the leftmost kite increases in azimuth angle, and the rightmost kite azimuth angle decreases, the power density values are still reasonably high until the azimuth difference gets to be quite large. However, higher rightmost kite azimuth angles seem to be unideal for higher power density. This is reasonable because this means that if the rightmost kite is directed more towards the right, with a negative azimuth angle, the spacing between kites is likely lower. Similarly, the further left that the leftmost kite is oriented, with a more positive angle, the higher the likelihood that it will not collide with the rightmost kite. So, for the wind perpendicular systems, the leftmost kite should likely have a positive azimuth while the rightmost kite has a negative azimuth, as confirmed with the results. As mentioned with the wind aligned results, too high of an azimuth actually causes a decrease in power since there is a large deviation from the wind direction, and power is needed to pull the kite back towards the ground station. This results in an optimal azimuth pair with angles lower than that of the azimuthal limits.

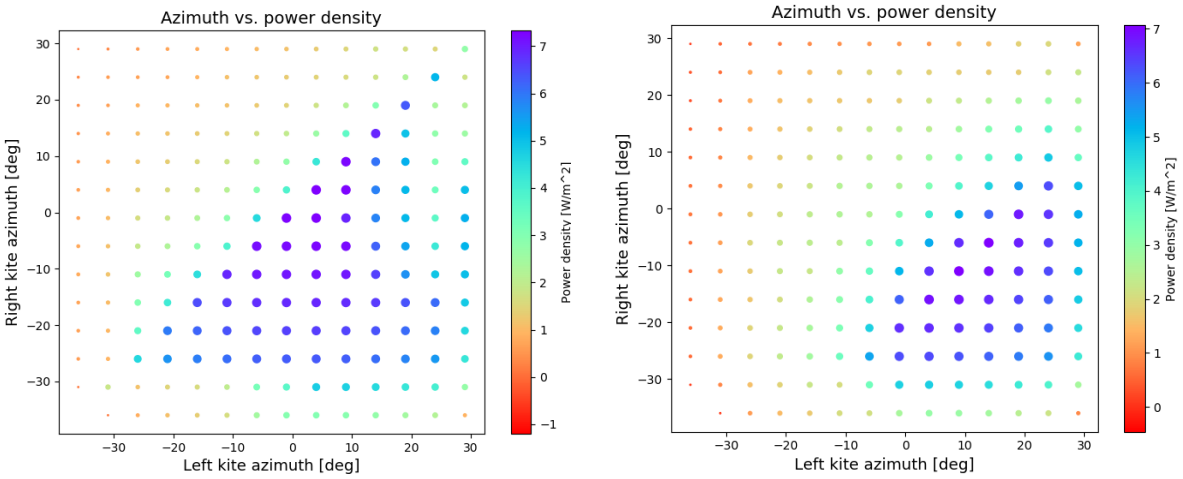

(a) No phase shift (b) Phase shift

Figure 6.9: Wind perpendicular system azimuth effect

Ultimately, the wind aligned systems provided significantly higher power density values, but the levelization of both optimal wind aligned systems is not greatly improved over the base case simulations. There may be a slight smoothing of the peaks for the phase shifted system, but there are still large jumps in the power output, and seemingly worse levilization when the power output is lower, i.e. when one kite is in traction and the other is in retraction. The instantaneous power of both phase shifted systems which produced the highest power densities can be seen in Figure B.3 in Appendix B.

6.4. Elevation angle effects

The operational elevation angle range for the base case system are between 7-44°, so this range will be considered for this analysis. While varying the elevation angles, all other flight variables remained the same to strictly evaluate the effect of the elevation angle. Having a elevation angle higher than the optimal value of 19° can potentially increase the power density by decreasing the spacing between kites, but decreases the average cycle power as well. The effects, however, are different for wind aligned and wind perpendicular systems, since wind aligned systems are more directly impacted. The effect of the elevation angle for a two kite base case system was evaluated over a range of elevation values for both wind alignments, as seen in Figures 6.10 and 6.11. Similar elevation angle results are further detailed in Appendix B in Figures B.5 and B.6.

The results of the wind aligned systems are shown below. The two systems show quite different trends with the elevation angles and power density values. With no phase shift, the similar elevation angle systems seem to produce the lowest ground station spacing values, and highest power densities. This is most likely due to the phase shift-like effect which results from having different elevation angles. This can result in one kite starting or ending the traction phase before the other, causing a greater distance requirement between ground stations. Additionally, with non phase shifted systems, it can be seen that having a downwind kite of a higher elevation angle additionally increases the spacing between ground stations, since if either kite should fly higher, it should be the upwind kite. But according to the simulations, a higher flying upwind kite does not produce higher power densities than similar elevation angle systems. For the non-phase shifted system, there is a relatively clear optimal elevation angle (for both kites) around 27°, which is confirmed with a more in depth analysis as shown in Figure B.5 to have a value of 28°. This results in a power density of 4.49 W/m^2. With the phase shifted systems, the results favor the similar elevation angle systems much less. There seems to be an optimal operational pair of 37° for the upwind kite and 17° for the downwind kite, resulting in a power density of 1.87 W/m^2. With a phase shift, generally higher elevation angles seem to be better for power density. This is likely due to the large space which is required if both systems are in traction, but in a different part of traction, causing potentially small distances between kites. A higher elevation angle allows the systems to be placed closer together then when compared to low elevation angle systems.

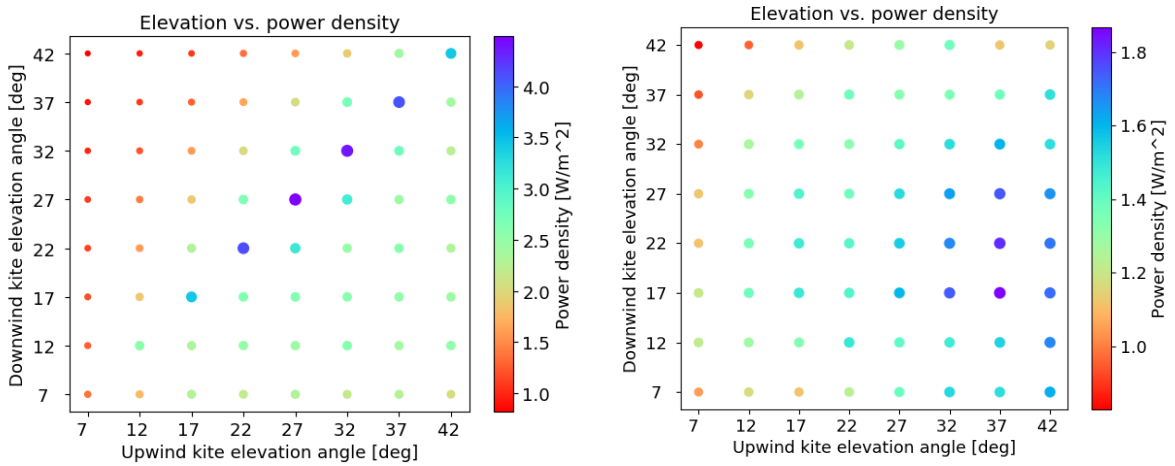

(a) No phase shift

(b) Phase shift

Figure 6.10: Wind aligned elevation effects

The wind perpendicular results are seen in Figure 6.11, with significantly different trends than that of the wind aligned systems. The non phase shifted system shows an interesting trend in which the similar elevation angle systems produce significantly higher power densities, but a slight deviation from a similar envelope decreases the power density due to the kites flying asynchronously. The highest power density, 7.30 W/m^2, was produced with azimuth of 17° for both kites. The optimal elevation angle was confirmed as 16° with the more in depth, similar envelope results of B.6a, but the power density remains relatively high in the range of 8°-31°, showing a low sensitivity to power density. Using

the same elevation angle for both kites without a phase shift allows relatively close spacing, since the kites will fly in the same pattern at the same time, which will not introduce any periods of time where the kites will be flying towards each other. When a phase shift is introduced, the kites can be closer together while one kite is flying a figure-eight maneuver towards the other kite, since they will not both be flying the same maneuver, introducing a smaller spacing between kites during this time period. However, the difference in phases should also indicate a larger distance between the kites. Ultimately, this results in a significantly lower overall power density for phase shifted systems with similar flight envelopes. The phase shifted systems show no distinct trends, but have slightly higher power densities in the elevation range of 17-37° of the leftmost kite, and 7-22° of the rightmost kite. The best result came from a left kite azimuth of 17° and a right kite azimuth of 12°, producing 4.93 W/m^2, which is significantly smaller than that of the phase aligned system, but still higher than the larger power density produced with a wind aligned system.

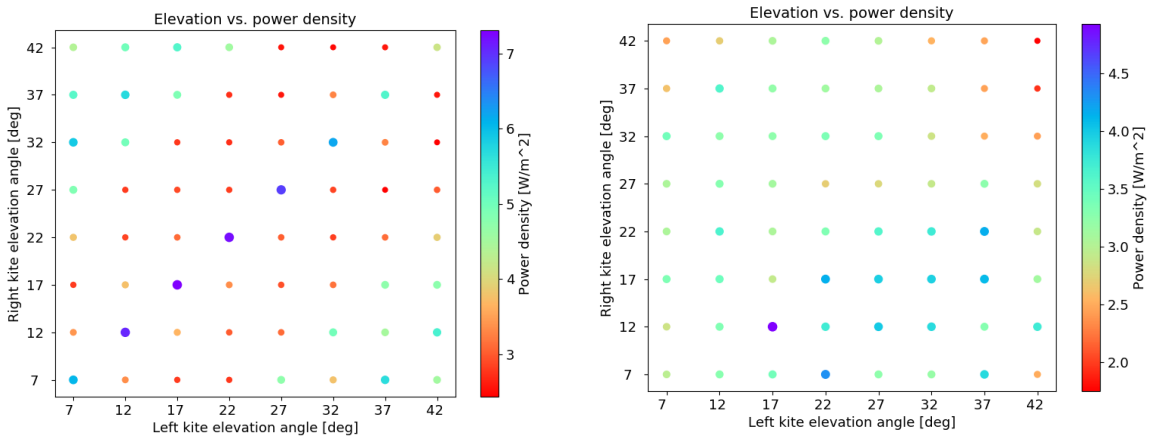

(a) No phase shift

(b) Phase shift

Figure 6.11: Wind perpendicular elevation effects

Similar to the azimuth angle results, the elevation angle effects on the instantaneous power levelization were not significant with the phase shifted systems that produced the highest power density. These instantaneous power curves are seen in Figure B.4 in Appendix B. The wind perpendicular system does exhibit a lower overall peak, and one longer region where both kites are in traction, providing a slightly improved power stabilization in that time period. However, these systems do not exhibit great power stabilization.

6.5. Maximum tether length effects

To fully analyze the two kite system and identify the effects of the minimum and maximum tether lengths individually, these variables were evaluated separately from each other while using the values from the base case flight path for the other flight path variables. For the maximum tether length, as well as with the minimum tether length, the wind profile has a significant impact. These variables change the operational height range more directly than the azimuth and elevation angles do, and they create much larger changes in altitude as well. In addition, these variables create kite farm systems with the largest difference in cycle durations. For example, if one kite has a significantly smaller tether length range, the cycle duration will also be significantly shorter. This impacts the average cycle time of the kite farm more distinctly than with azimuth or elevation angle changes, and should therefore be considered when comparing the power density values.

Figures 6.12a and 6.12b show the wind aligned maximum tether length evaluation results of the two kite systems with and without phase shifts. For the system with no phase shift, it is shown that the power density results are best when the tether lengths are similar for both systems. The highest power density, 3.88 W/m^2, occurs when both maximum tether lengths being 900 meters. This indicates that longer maximum tether lengths may produce even higher power densities because of the longer traction phase duration. Additionally, this means that the systems benefit from the higher wind speeds at higher altitudes, even though the tether drag increases from additional tether being

reeled out. However, the lowest power density, 1.69 W/m^2, resulted from the system with an upwind kite maximum tether length of 900 meters, and a downwind maximum tether length of 500 meters. This is quite a large difference for the same upwind kite maximum tether length, and a downwind maximum tether length difference of 400 meters. This shows that if the upwind kite maximum tether length is considerably larger than that of the downwind kite, a greater spacing will be required between units. If the downwind kite maximum tether length is longer than that of the upwind kite, it is not as much of an issue, since during its traction phase, it will be moving away from the upwind kite. For the phase shifted system, there is a more gradual trend. Generally, as the upwind kite maximum tether length decreases, and the downwind maximum tether length increases, the power density increases. The maximum power density occurs with maximum tether length values of 400 and 700 meters for the upwind and downwind kites, respectively, producing 2.41 W/m^2. The lowest power density for the phase shifted system resulted from maximum tether lengths of 900 and 600 meters respectively, with a power density of 1.11 W/m^2. These value are slightly lower than those of the non phase shifted systems, but might prove economically beneficial when including the costs of storage systems needed for in phase systems. Both analyses generally show negative results when the upwind kite has a longer tether length, but the non phase shifted systems with similar tether length values benefit from having the same flight path, greatly decreasing the required spacing between units.

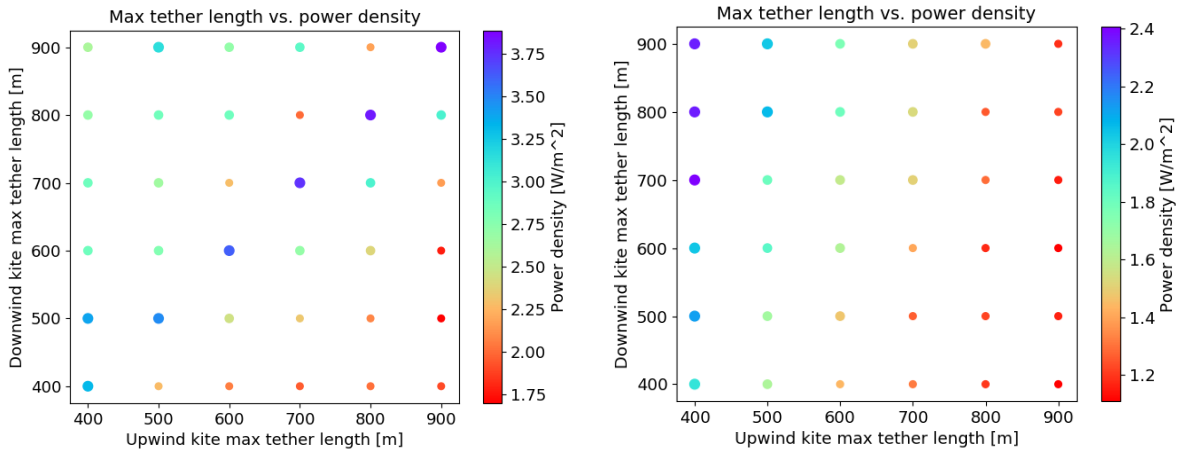

(a) No phase shift (b) Phase shift

Figure 6.12: Wind aligned system maximum tether length shift effects

The wind perpendicular results are displayed in Figures 6.13a and 6.13b. The results of the non phase shifted system are similar to those of the wind aligned system, but the wind aligned, phase shifted results are quite different than those of the wind perpendicular system. With no phase shift, there is a clear benefit for systems with the same maximum tether lengths, with any deviation resulting in a large decrease in power density. Additionally, as the maximum tether lengths increase, the power density increases slightly as well, which is similar to the results of the wind aligned case. The highest power density, 7.61 W/m^2, results from a system with both maximum tether lengths being 900 meters. This further shows the benefit of longer maximum tether length systems. If the tether length values are not the same, the power density values are more similar to those of the wind aligned systems. For the phase shifted system, there is no distinct trend to be seen and it is difficult to identify specific areas of high power density. This likely means that this system type is highly dependent on the exact path which is flown, and even a slight tether length change could significantly change this. However, the power density values are slightly higher than those of the wind aligned systems. The highest power density, 4.15 W/m^2, occurs at maximum tether lengths of 600 meters for both kites, showing that similar kite paths work well for this phase shifted system as well. This results in no improvement in the power stabilization over the base case results shown in Figure 6.4b since the highest power density here also occurs with similar flight path systems.

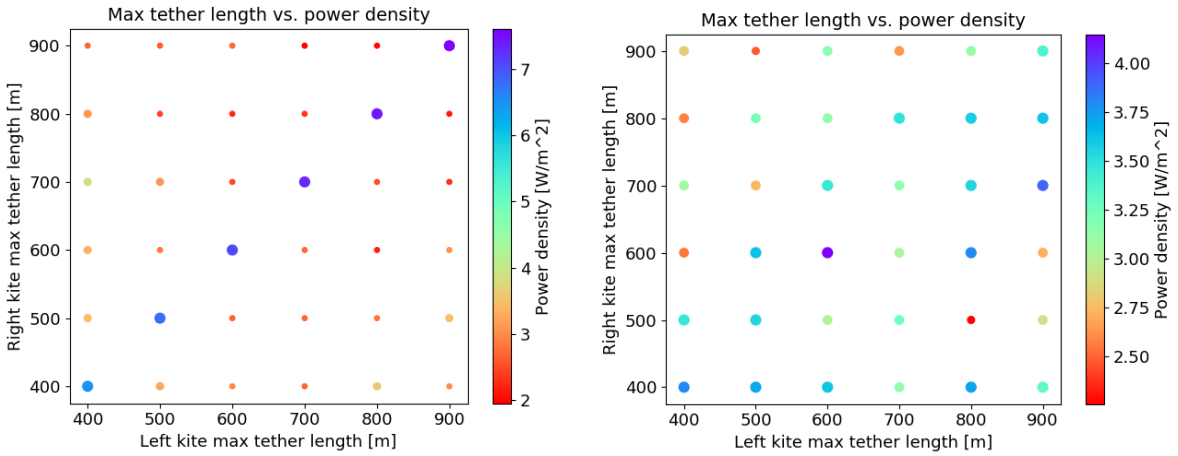

(a) No phase shift

(b) Phase shift

Figure 6.13: Wind perpendicular system maximum tether length shift effects

6.6. Minimum tether length effects

The minimum tether length results for a two kite system, visualized in Figure 6.14, showed some similar patterns to the maximum tether length evaluation, but also some deviating results as well. The wind aligned system with no phase shift featured a trend where similar minimum tether lengths produced the highest power density, as was the case for the maximum tether length in this system configuration. With no phase shift, a minimum tether length of 300 meters for each kite produced the highest power density, 3.75 W/m^2. This is interesting, since a minimum tether length of 300 meters does not create the largest traction range. Based upon the maximum tether length results, one may assume that the lowest minimum tether length would result in the greatest power density, creating a system with the longest possible traction phase, and therefore the highest average cycle power. But, these results show that with a tether length of 300 meters, the increased wind speed produces considerably more power than it does at lower altitudes which are reached with shorter minimum tether lengths. Additionally, it can be seen that greater upwind minimum tether lengths generally cause increase spacing requirements and lower power densities. This is similar to the results of the maximum tether length, since it increases the overlap of the upwind kite's flight path with the downwind kite's. Slightly larger downwind kite minimum tether lengths do not cause as great of a negative impact, and should also increase the traction duration time, possibly resulting a higher average cycle power. There was also no specific trend for the wind aligned phase shifted system, which is different than the clear, gradual trend of the maximum tether length results for this scenario. For the phase shifted system, the highest power density resulted from minimum tether lengths of 600 meters for the upwind kite and 100 meters for the downwind kite, with a power density of 1.80 W/m^2, which is a strange result given the clear trends of the non phase shifted system which show a negative performance for this tether length combination. However, the upwind kite has quite a small flight path in comparison to the downwind kite's path, and can operate quite independently as the downwind kite spends a considerable time far away from the upwind kite. Only during the end of the retraction phase are the airborne systems near each other. This allows for one kite (the downwind kite) to produce a large amount of power while the upwind kite completes many quick cycles of lower power generation. The difference between the maximum and minimum power density for this system is not so large, only 0.6 W/m^2. This shows that this factor does not have quite a significant impact on this system type, and that a phase shift will produce quite low power densities with this system configuration.

The two kite wind perpendicular results, displayed in Figure 6.15, are also similar to those of the maximum tether length. Without a phase shift, there is again a great benefit for similar minimum tether length systems. The best power density, 7.34 W/m^2, is with both minimum tether length values being 300 meters, just as with the wind aligned, no phase shift system. Here, the power density values of similar path system are much higher than the power densities at other minimum tether length combinations, showing that similar envelopes require considerably less spacing between units if there is no phase shift. The wind perpendicular, phase shifted system again shows no distinct trend, but

has higher power density values than the wind aligned systems in general. With a phase shift, the highest power density results from the leftmost kite minimum tether length of 500 meters, with the rightmost value being 600 meters, producing 5.45 W/m^2. This result is quite a bit higher than that of other minimum tether length combinations for this system, which could show that the exact flight path, particularly the traction movements, greatly affect the required spacing between units. If there is just a small period of time where the airborne components are near each other, this causes a great impact to the spacing requirements, even though the systems may be quite distant outside of this time period. Again, a farm control system would be of great benefit for this issue.

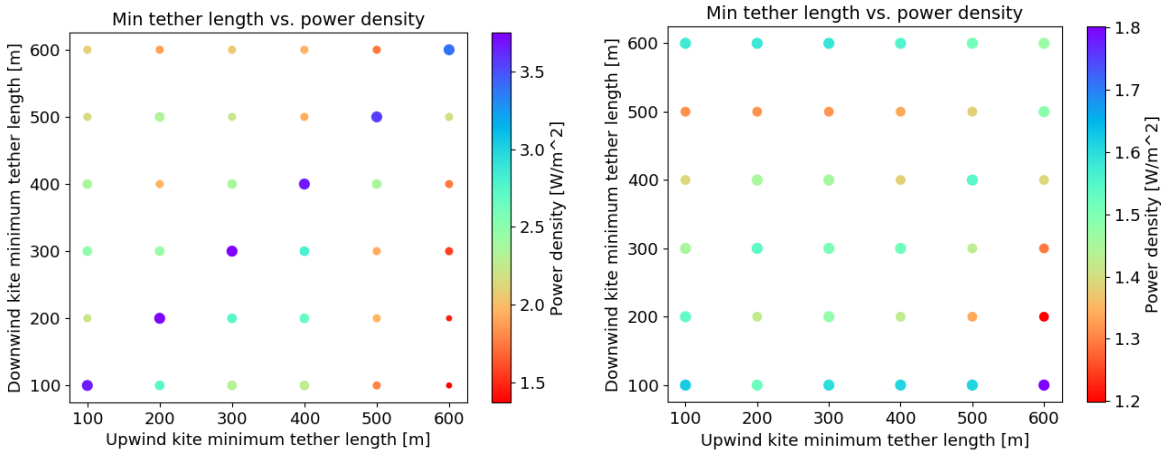

(a) No phase shift (b) Phase shift

Figure 6.14: Wind aligned system minimum tether length shift effects

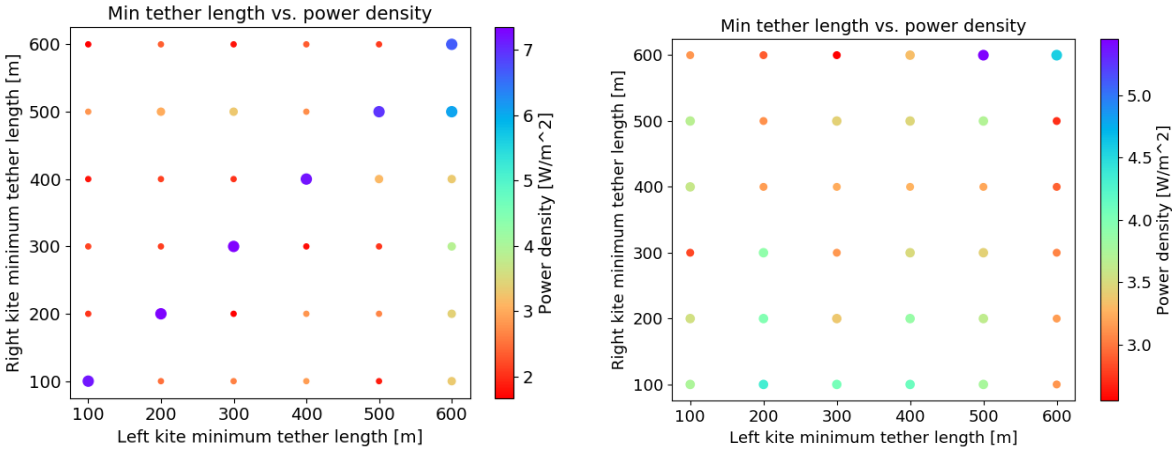

(a) No phase shift (b) Phase shift

Figure 6.15: Wind perpendicular system minimum tether length shift effects

7

Case B: 3 kite system

To evaluate the effects of an additional kite, a three kite system is analyzed as well. It is expected that three kites will better levelize the instantaneous power, while also providing a higher overall average cycle power. With this case study, the same flight path variables will be evaluated as with the two kite system, but there will be a focus on layouts specific to a three kite system, including a triangle layout. For reference, a three kite farm with the base case flight paths produces an average cycle power of 79.82 kilowatts. A three kite wind aligned system has a power density of 3.22 W/m^2, with a required ground station spacing of 175 meters between all kites, while the wind perpendicular system has a power density of 7.34 W/m^2 and a ground station spacing of 60 meters between all kites. One additional benefit of a 3 kite system is dissimilar spacing between units, which could potentially combine the benefits of different flight path with different ground station spacing arrangements.

7.1. Kite area effects

The power and power density results over a range of kite areas for the base case three kite system are shown in Figure 7.1. The trends for required unit spacing and shortest distance reached between airborne components were similar to the results of the two kite line system, so they are omitted here. Additionally, since similar flight paths were used, similar spacing between ground stations was used as well. Overall though, similar results are achieved for this system when compared to the two kite systems. The main difference is that the overall power output is higher as a result of having an additional kite. But the change in the power density values over increasing kite size remains relatively similar, showing lower values for the wind aligned system, and power densities nearly twice as large or greater for the wind perpendicular systems. Additionally, the triangle layout shows an intermediate system which produces results between those of the single row wind aligned or wind perpendicular systems, since the triangle system is essentially one wind aligned column in combination with one wind aligned row. This creates a system which can perform better with more wind direction changes than a single line system could, but will perform worse if there is often wind in the perpendicular direction. The triangle kite layout, however, will have the same power density for each wind orientation. For all layouts, though, there is a clear trend of higher power densities with larger kite sizes, indicating that the optimal system may be with a kite size larger than 170 m^2, since a power density limit is not clearly approached in these results.

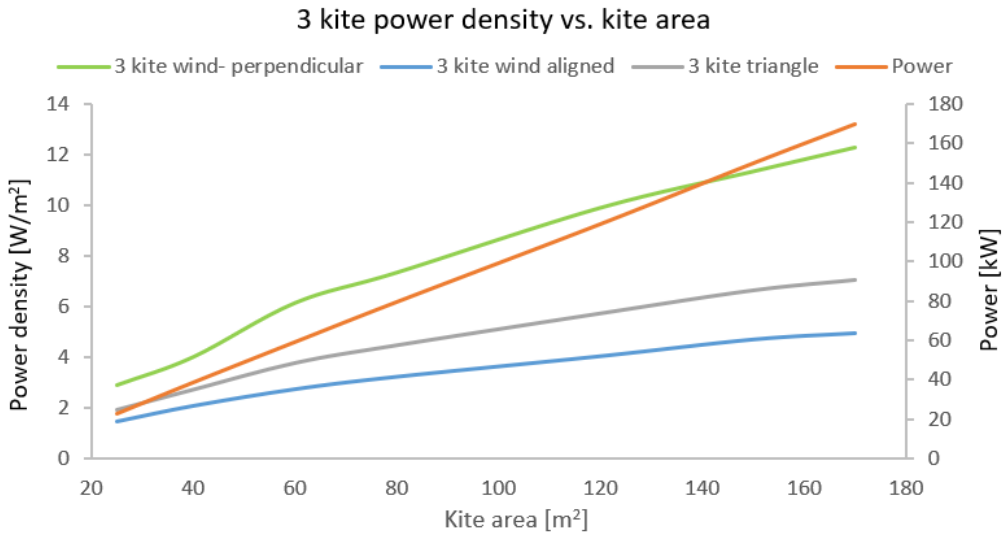

Figure 7.1: Three kite power and power density vs. kite area

7.2. Phase shift effects

Because the instantaneous power fluctuation of a two kite system is relatively high due to a misalignment of phase durations, a three kite system is expected to have greater power stability possibilities. The results of a three kite wind aligned system are shown in Figure 7.2a which displays the results of the base case system where all units are phase shifted. Again, the short spikes in power are from the lack of a ground station controller, but these should be mitigated with further simulation developments. The slightly larger drop in instantaneous power results from a slight difference in the traction and transition phase durations when compared with the retraction phase duration. With this system, two kites are ideally always in traction at any given time, but the slight power drops occur when there is just one kite in traction. This could also be mitigated with a flight path planner which is based upon phase duration instead of a pre-defined path. If these areas of concern can be mitigated, this three kite phase shifted system shows great promise for power levelization. Still, the variation in the power output decreases greatly when compared to the two kite system. With the triangular system, two units are in phase, while one unit is phase shifted. The results are displayed in Figure 7.2b, and it seems to have a much lower power stabilization, demonstrating behaviors of both the phase shifted and non phase shifted systems, and even requiring additional power input when only one kite is in traction.

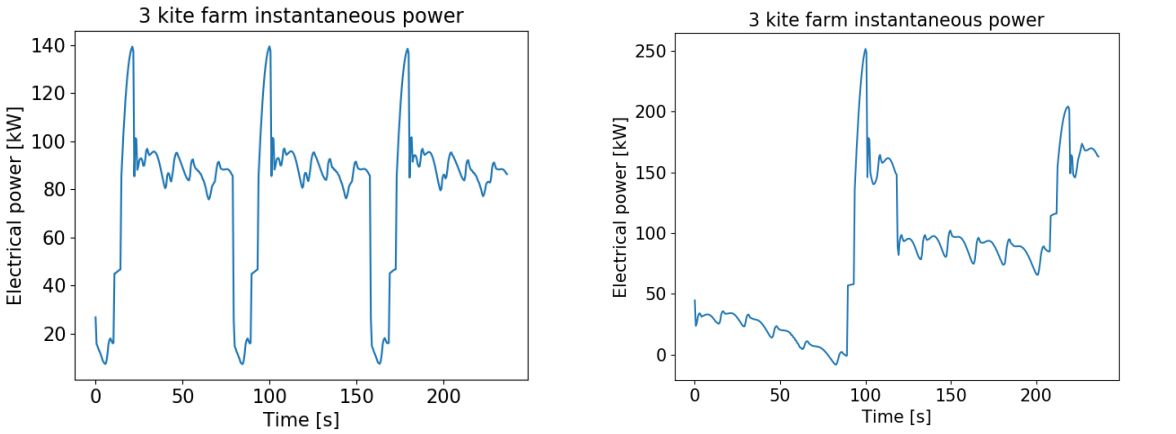

(a) 3 kite linear farm cycle power with phase shift (b) 3 kite triangular farm cycle power with phase shift

Figure 7.2: Three kite phase shift effects on power

The trends in the distances between kites and tethers can be seen in Figures B.1 and B.2 in Appendix B. These curves are similar to those of the two kite system results, with an additional phase shifted curve which represents the distances between the second and third kite or tether. Only the single line systems are evaluated here, with parallel and perpendicular wind alignments, since the triangular system results will fall between the two. Again, the wind perpendicular system requires considerably less spacing between units for these single line systems. This results in large distances between the wind aligned systems at times, with the kites reaching over 1000 meters apart at times.

7.3. Azimuth angle effects

With three kites, the power density results are more difficult to visualize, so the highest and lowest power density results for each system type are shown in Table 7.1. The first kite azimuth refers to the most upwind kite for wind aligned systems, or the leftmost kite for wind perpendicular systems. The second kite is the center kite, and the third kite is either the most downwind kite or the rightmost kite of the system. Both the wind aligned and perpendicular orientations were analyzed, so the triangular layout was omitted, as the results would fall in between.

With the wind aligned, no phase shift results it can be seen that adjusted azimuth angles present a great benefit to the power density for this system layout. Shifting the first and second kites allows the spacing to decrease more than the power output, which increases the power density when compared to a similar envelope system such as the base case system. The spacing for this system is 130 meters between each kite. When all three kites are flown near the optimal single kite azimuth, the required spacing is 180 meters between all kites, so this is a significant improvement. For the wind aligned phase shifted system, even more azimuth shifts result in the highest power density. This provides an increased area for each kite to operate in throughout their entire cycle. While the deviation from the optimal single kite azimuth does slightly decrease power production, the spacing is decreased when compared to a system of no azimuth shifts. For the wind perpendicular direction, the spacing between units with the optimal single kite azimuth is already relatively small, so using a similar azimuth system for this layout produces the largest power density if there is no phase shift. With this layout type, adjusting the azimuth for decreased ground station spacing apparently significantly decreases the power output to the point where the power density is lowered. With the phase shifted, wind perpendicular system there is, however, a benefit from shifted azimuth angles. In this case, all azimuth angles are 20° apart, with the outermost kites pointed away from the center kite, allowing a decent amount of space for each kite to fly in separately. This allows the center kite to fly with the optimal single kite azimuth angle, and results in decreased spacing between the units.

Table 7.1: Three kite system azimuth effects overview

Wind	**Phase shift**	**1st kite azimuth** [°]	**2nd kite azimuth** [°]	**3rd kite azimuth** [°]	**Power density** [W/m^2]
Align	No	20	-20	0	3.66
Align	Yes	20	-20	-20	2.35
Perp.	No	0	0	0	7.30
Perp.	Yes	20	0	-20	4.69

While the systems with no phase shift had the higher power densities, they also had the lowest stability in power output, with results similar to those seen in 6.4a. The power is more constant during the traction phase, but it will always require energy during the retraction phase if there are no phase shifted units. The instantaneous power results for the phase shifted cases described in the table above are displayed in Figure 7.3. The phase shifted systems show a slightly more consistent power output, typically not requiring power input during steady state flight. The large, short spikes in the phase shifted system can be mitigated with a control system, but the smaller variations would need to be changed with an alternative flight path or phase shift value. The variation in power output is a result of different cycle durations at different azimuth angles, and is most likely the reason for the larger power

drop with the wind perpendicular system, which also has negative power for a small amount of time. Smaller azimuthal shifts would decrease the difference in cycle durations, therefore lessening larger drops in power, but the power density would then decrease since required spacing would increase.

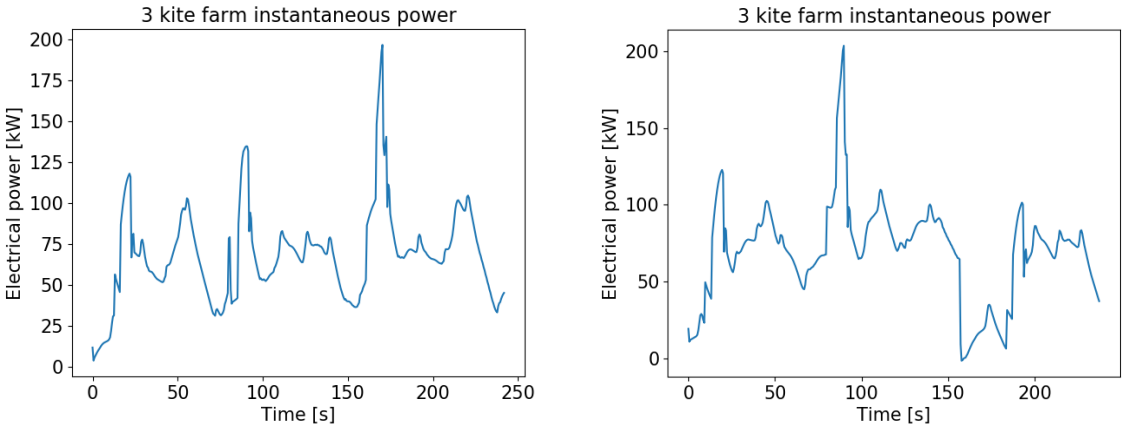

(a) Wind aligned, phase shifted

(b) Wind perpendicular, phase shifted

Figure 7.3: Three kite azimuth effects on instantaneous power

7.4. Elevation angle effects

The elevation angle effects for a three kite single line system are displayed in Table 7.2. Several of the systems have elevation angles which deviate considerably from the optimal angle of 19°, yet many also feature one or more kites which operate with an elevation angle close to 19°. This indicates that even though an elevation shift could decrease the spacing requirement between units, as with the wind aligned systems, the elevation angle of each kite strongly impacts the power produced. A large deviation from 19° causes quite a large decrease in power, which can only be compensated for if the ground station spacing is significantly lower that is required with an elevation angle of 19°. For the wind aligned system with no phase shift, this is the case, and all kites operate at an elevation angle of 30°, which requires a ground station spacing of 120 meters. This is a significant improvement over the 175 meters required between units which utilize an elevation angle of 19°, and thus the power density is improved, even though each kite produces slightly less power. However, if the height which is reached during the retraction phase can be decreased, such as with a change in angle of attack, shifted elevation envelopes could potentially have an additional improvement in power density. The limitation here would be the reeling speed of the selected component for use in the ground station, since if the kite flies towards the ground station or the ground too quickly, there will be a large amount of tether sag, which causes safety issues. With a phase shift in the wind aligned system, higher elevation angles produce a similar benefit to that of the non phase shifted system. For the wind perpendicular system with no phase shift, the highest power density resulted from kites of the same elevation angle, but with values closer to the optimal single kite elevation angle. This is because the spacing requirement between wind perpendicular units is relatively small, and operating at extreme elevation angles greatly decreases the power output without decreasing the ground station spacing as much. There is some benefit with this system type operating at more extreme elevation angles, but the power density values produced are not quite as high as with the similar elevation angle system. For wind perpendicular phase shifted systems, though, these shifted elevation angles are notably more beneficial. For this scenario, the highest power density results from a system where the outermost kites fly at a much higher angle than that of the center kite. This allows some additional space for each kite to operate in individually, since they are all phase shifted, by requiring each kite to deviate slight from the optimal elevation angle of 19° by about 10-20°. For this system, the elevation angle adjustment allows closer spacing than if all kites were operating at the optimal elevation angle. This phase shifted system does produce a lower power density than the non phase shifted system, but the value is still higher than that of either wind perpendicular system.

Table 7.2: Three kite system elevation effects overview

Wind	**Phase shift**	**1st kite elevation** [°]	**2nd kite elevation** [°]	**3rd kite elevation** [°]	**Power density** [W/m^2]
Align	No	30	30	30	3.94
Align	Yes	30	30	20	1.23
Perp.	No	20	20	20	7.30
Perp.	Yes	25	10	30	4.08

The power density of the wind aligned system with no phase shift is similar to results in 6.4a, since all flight envelopes are similar and synchronous. The same applies for the wind perpendicular system with no phase shift, as it also operates with similar flight envelopes. The results from the phase shifted systems with the highest power density are shown in Figure 7.4. The wind aligned system with a phase shift shows less variation in the power output, with only one period of time in which there is a power drop of concern. This power drop occurs because the cycle duration of the third kite is different from that of the other. A more levelized power output could be produced if all kites have the same phase durations, as is the case with similar flight path systems. This system shows potential for high power stability if slight path alterations are implemented. With the phase shifted wind perpendicular system, there is also some improvement in power stability, but the instantaneous power values show a much larger variation than with the wind aligned system with a phase shift, which is most likely due to the larger difference in elevation angles between kites.

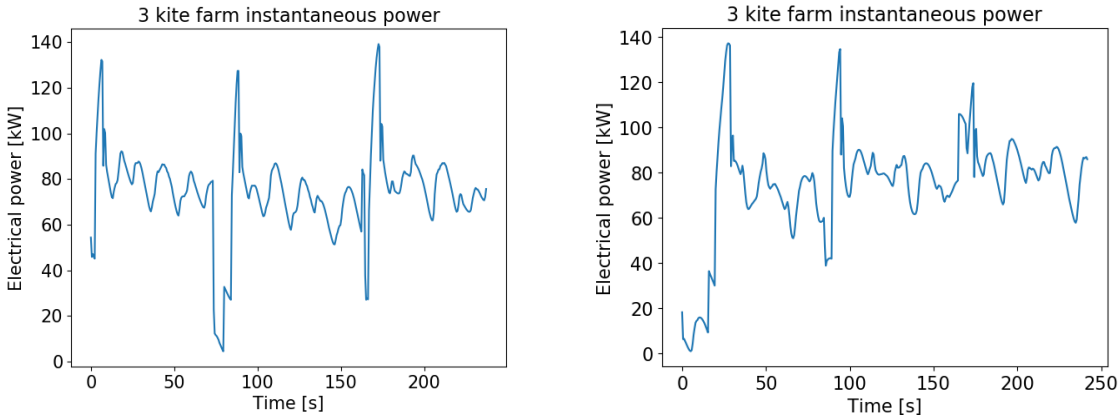

(a) Wind aligned, phase shifted

(b) Wind perpendicular, phase shifted

Figure 7.4: Three kite elevation effects on instantaneous power

7.5. Maximum tether length effects

The three kite maximum tether length effects are summarized in Table 7.3. For both non-phase shifted systems, irrespective of wind direction, the optimal maximum tether length for all kites was 900 meters. This reiterates the outcome from the two kite simulation where the longest possible maximum tether length also generally produced the highest power density values. While longer maximum tether lengths do utilize more airspace during operation, they also allow for a longer traction phase and access to greater wind speeds. Furthermore, at a high elevation angle, the spacing could potentially decrease further and even higher wind speeds would be reached. The spacing requirement of the best wind aligned system is more than twice as great as that of the best wind perpendicular system, since it has less than half the wind perpendicular system's power density but the same average cycle power. For the phase shifted systems, shorter maximum tether lengths of the same length for all kites were better for higher power density values. This keeps the duration of the traction phase quite short, minimizing time spent near other kites.

Table 7.3: Three kite system maximum tether length effects overview

Wind	Phase shift	1st kite max tether length [m]	2nd kite max tether length [m]	3rd kite max tether length [m]	Power density [W/m^2]
Align	No	900	900	900	3.26
Align	Yes	400	400	400	1.66
Perp.	No	900	900	900	7.61
Perp.	Yes	400	400	400	5.32

Since all systems which produced the maximum power density in the table above were similar flight envelope systems, the effect on power output was not as ideal as with the azimuth and elevation results. Figure 7.5 shows the instantaneous power results for the phase shifted cases, which is the same since the largest power densities occur with the same maximum tether length values. Large changes in the power values can be seen for these phase shifted systems, which are due to the phase durations of the flight paths. The highest power output occurs when several kites are in the traction phase, but these values drop when one kite exits the traction phase. It is clear that these flight paths are not optimal for power stabilization, but the power is almost always at 20 kilowatts or higher throughout the entire cycle.

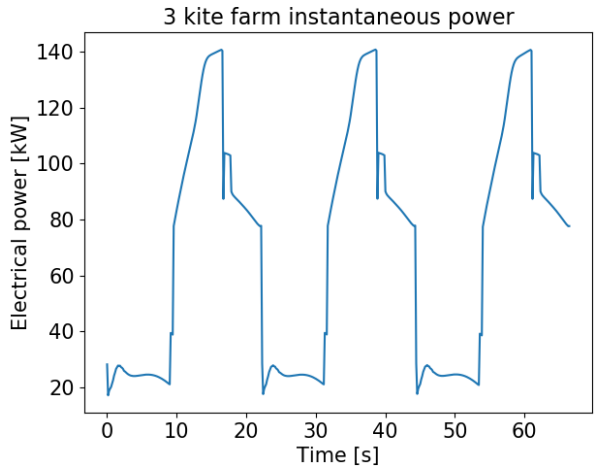

Figure 7.5: Three kite maximum tether length effects on instantaneous power

7.6. Minimum tether length effects

The minimum tether length results show trends similar to that of the maximum tether length results, as seen in Table 7.4 below. Both non phase shifted systems had the same results for the highest power density, as was the case with the maximum tether length evaluation, with all kites having a minimum tether length of 300 meters. Again, the wind perpendicular power density was about twice that of the wind aligned system, but the difference is slightly less for the minimum tether length results. However, the phase shifted systems have slightly differing results when compared to the maximum tether length results. The wind aligned, phase shifted system had the highest power density when the upwind kite had the largest traction range, while the two downwind kites had quite small tether length ranges. This allowed for the upwind kite to produce a large amount of power with the single kite optimal path while the downwind kites produced power in more frequent cycles. This ultimately resulted in quite a low power density though. The wind perpendicular system with a phase shift had the highest power density from the opposite minimum tether length setup. This featured the two leftmost kites with short traction ranges, and the rightmost kite with the longest possible traction range. Again, this allows for two kites to operate in quicker cycles while one kite flies a much longer traction phase, providing some spacing for the units. Additionally, the instantaneous power for the phase shifted systems from the

table above can be seen in Figure 7.6. The difference in tether lengths between the kites causes an interesting effect on power output, with a considerable amount of variation. This is because of the large differences in cycle duration between the kites, so it is not recommended to have systems with large differences in minimum or maximum tether lengths. For the phase shifted wind perpendicular system, though, the power density was still quite high, especially compared to the wind aligned results.

Table 7.4: Three kite system minimum tether length effects overview

Wind	**Phase shift**	**1st kite min tether length** [m]	**2nd kite min tether length** [m]	**3rd kite min tether length** [m]	**Power density** [W/m^2]
Align	No	300	300	300	3.14
Align	Yes	300	600	600	1.41
Perp.	No	300	300	300	7.34
Perp.	Yes	500	500	100	5.06

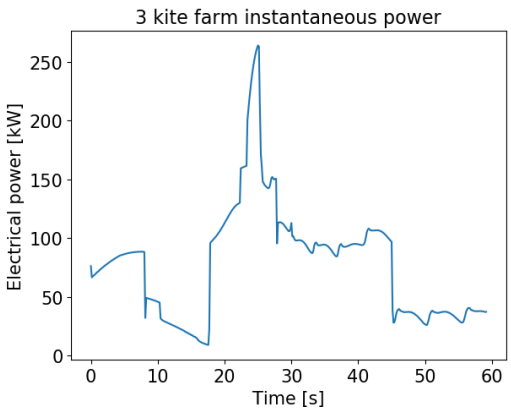

(a) Wind aligned, phase shifted

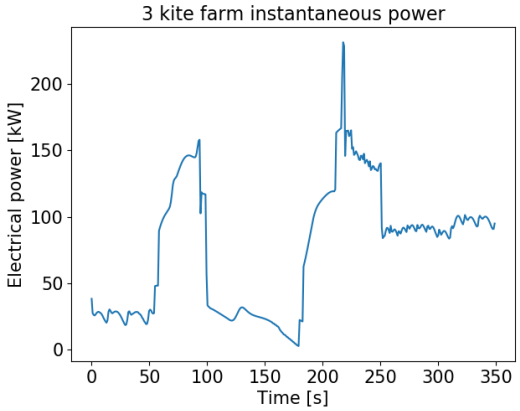

(b) Wind perpendicular, phase shifted

Figure 7.6: Three kite minimum tether length effects on instantaneous power

8

Results and discussion

In this chapter the case study results will be discussed and compared to an additional kite farm analysis and to simulation results from larger kite farm simulations. This includes results from larger kite layouts which were not discussed in the case studies and from previous kite farm research. Finally, the results of the case studies will be applied to a selected location to assess the viability of implementation.

8.1. Previous methods comparison

To evaluate the kite farm simulation, the results are compared with those a previous study. In [13], a kite farm was analyzed with more conservative spacing requirements and similar flight paths for all kites in each farm system. To decrease these ground station spacing requirements of the previous analysis, overlapping kite flight envelopes were evaluated, enabled with phase shifts or adjusted flight paths for each kite. Using the the updated spacing equation from the previous analysis, Equation 5.4, the ground station spacing of a two kite wind aligned system with the base case flight path requires a distance of 332 meters, while the farm simulation verifies a spacing of 175 meters to be sufficient if there is no phase shift. Equation 5.4 is not created to estimate spacing requirements with phase shifted systems since the author recommends to utilize only small phase shifts with wind aligned systems [13]. Therefore, there is quite a difference between the distances calculated with the equation of the previous methods, and for both the phase shifted and non-phase shifted systems in the simulation. This difference in spacing is quite significant, decreasing the required land by almost half with the non-phase shifted systems over many elevation angles. The ground station spacing requirement results of the 2 kite wind aligned, similar envelope systems are shown in Figure 8.1. These results utilize base case flight paths for all parameters except the elevation angle. The elevation angle is a main variable in the spacing equation, so it is utilized to show the difference in required spacing. It results that the farm simulation typically calculates a much smaller spacing requirement than is derived through the equation, showing that the earlier estimates were quite conservative. However, for phase shifted systems, the required spacing is relatively constant over different elevation angles, showing that spacing for this system type is more difficult to characterize than that of the non-phase shifted system. Moreover, for elevation angles above 35°, the equation of the previous method actually underestimates the required spacing between units, but this is outside of the applications of the equation. Additionally, the difference in results with the non phase shifted systems seem to be slightly higher at lower elevation angles, indicating a slightly better estimate of farm system spacing with the farm simulation over the equations. The figure below also leads one to believe that after a certain elevation angle, the required spacing is not decreased further if there is no phase shift, which is confirmed by both methods. However, these elevation angles would be quite extreme for regular operating conditions, and would likely decrease the power output greatly. Also, the angles which produced the highest power densities in the elevation angle evaluations were almost never above 30°, which implies that utilizing elevation angles above this provides only a small decrease in required unit spacing.

For a two kite wind perpendicular system with base case flight paths, Equation 5.3 yields a required ground station spacing value of 502.9 meters, while the kite farm simulation verifies a distance of 60 meters to be sufficient if there is no phase shift. With a phase shift, the simulation outputs a required

spacing of 175 meters. Equation 5.3, however, should be valid for phase shifted systems since both kite's flight paths should be completely independent, with no possibility of collision because of the perpendicular wind alignment. With this equation, the large spacing requirements result from the large width of each kite's path as it nears the end of traction, especially with longer maximum tether length values. Using conservative calculations and non-overlapping flight envelopes, the kites and tethers are often several hundred meters apart, providing a massive factor of safety, but unnecessarily large spacing between units. For the kite farm simulation, the spacing is not dependent upon the width of the figure-eight shape which is flown, but rather, the distance maintained between the two kites and their tethers. Therefore, it is quite difficult to estimate the required spacing between units without first running the simulation. With the simulation results for non-phase shifted systems which have the same flight path, the distance between the kites and tethers over time remains mainly the same despite any change in figure-eight width. This results in a constant spacing requirement between units even as the figure-eight width increases, as can be seen in Figure 8.2, which shows the ground station spacing results of both methods for wind perpendicular systems. For phase shifted systems in the kite farm simulation, the figure-eight width does have an impact. Still, the previous methods of spacing calculations were even more conservative than with the wind aligned results, becoming overly conservative with wider flight paths. With narrower flight paths, the difference in ground station spacing requirements is not as large, but still significant.

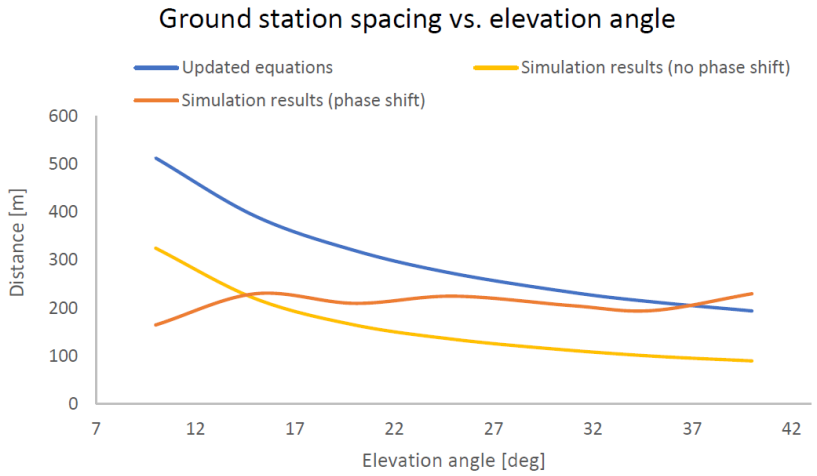

Figure 8.1: Wind aligned system ground station spacing comparison

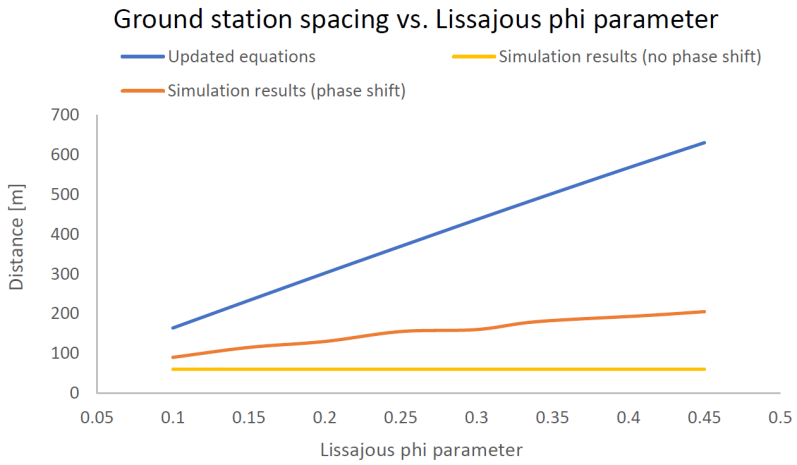

Figure 8.2: Wind perpendicular system ground station spacing comparison

8.2. Simulation results

To directly compare the two and three kite systems, as well as results from different kite farm layouts, their results will be analyzed together. The power density over kite area results for the case studies are shown in Figure 8.3 for non phase shifted systems, and it can be seen that the values are relatively similar. All phase shifted power density values are lower for each wind alignment, so they are omitted. Above kite areas of about 100 m^2, the two kite system performed slightly better for the wind perpendicular configuration. For the wind aligned systems, the two kite system performed generally a bit better than the three kite system. The benefit of the two kite system can be attributed to the required spacing between units. With larger spacing requirements between kites, as with larger kite areas, having spacing between two kites, instead of using one individual kite, increases the land used. Additionally, the benefit of a triangle system layout over the wind aligned systems can be seen, but they still have a significantly lower performance when compared to wind aligned systems, and poor power stabilization even with the addition of a phase shift. They are, however, a good option for locations with large and frequent changes in wind direction, although a square or rectangular system may be of additional benefit.

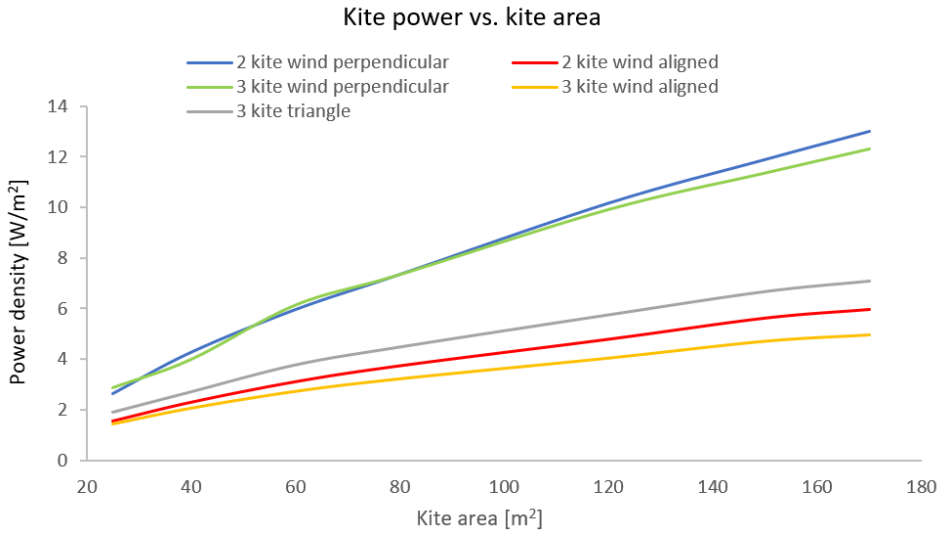

Figure 8.3: Power density vs. kite farm size

Additional layout configurations were considered as well, including four and twenty kite systems, and the power density values over increasing kite area results are in Figure 8.4. It should be noted that these systems do not include a phase shift and will require storage for the retraction phase power input, and the larger the system and power output, the larger the storage requirement. Although phase shifted systems should not require storage, they generally require larger spacing and therefore have lower power densities. The instantaneous power of the four and twenty kite systems can be seen in Figures B.7 and B.8 - B.11 in Appendix B, along with Tables B.2 and B.3 which detail the power and spacing results at different kite areas. It can be seen that having more kites does not necessarily mean improved power levelization, but, with several phase shifted kites it can be improved. In fact, quite a high power levelization occurs with the 20 kite system with all units in a phase shift with a wind perpendicular orientation. Although this is not so practical, it gives an indication of the potential for levelized power output from kite farms. In the figure below, the general trend is that smaller kite farm systems, or farms with fewer kites, produce higher power densities typically, with quite high values when using large kite sizes. The wind aligned systems seem to exhibit a logarithmic curve, indicating a power density limit at lower kite sizes. For the 20 kite system with four wind aligned columns, the power density curve becomes almost constant after a kite size of approximately 40 m^2. However, for the 2 kite wind perpendicular case, it seems that the power density limit would be at a slightly larger kite size. Interestingly, according to these results, the optimal power density would result from utilizing a 2 kite wind perpendicular layout with as large of a kite size as possible. This is however, excluding any flight envelope changes which could further improve spacing.

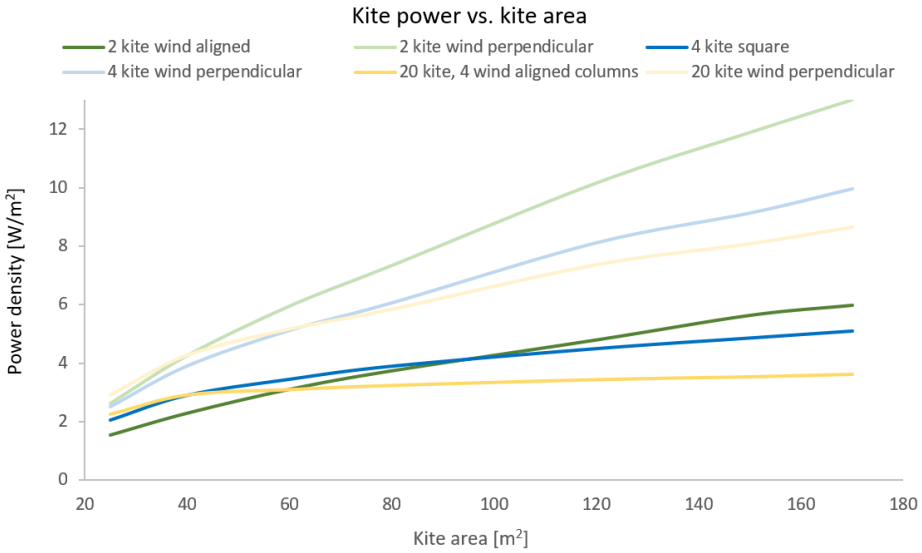

Figure 8.4: Power density vs. kite farm size

Since wind perpendicular rows of kites are preferred, as they can utilize smaller ground station spacing, an in depth analysis of the environmental conditions should be conducted for each site at which a kite farm is to be installed. Several long, wind perpendicular rows would be desirable if the wind is often in one particular direction. However, if the wind then changes to make the system wind aligned, the ground station spacing may be too close together. For this reason, square systems or systems with similar amounts of rows and columns are better for overall system operation. Additionally, the lift and drag coefficients have a significant impact on the kite flight path, and this is an area that could be greatly further researched. Adjusting the lift or drag to alter the angle of attack during retraction can produce a lower flying path, possibly allowing for improved spacing between units. Another point of further research would be to evaluate the effect of using the larger safety radius of each kite, which would decrease the power density values, but may show more of a benefit for larger kite systems.

It was also quickly apparent that having kites with different flight paths creates dissimilar cycle times. This would mean that the two kites would be continuously operating in different points of their cycle, with a constantly changing phase shift. Spatially, this causes issues with non phase shifted systems that have dissimilar flight paths, which are similar to those seen with the implementation of a phase shift. These issues are mitigated with increased spacing requirements, and this leads to higher performances from similar flight path systems. The importance of a farm control system is iterated here since thorough control of all kites could improve kite farm performance. Moreover, if a path planning or farm control system ensures that all kites perform synchronized figure-eight movements during traction, the spacing requirement between units could further decrease. This would need to be done with a constant width flight path, and the 3D flight path module utilizes a constant angle approach. Constant width flight envelopes would also ensure a constant maximum distance that the kites can fly to one side or another. This keeps the kite from flying wider maneuvers as they near the end of the traction phase.

8.3. Implementation applications

With AWE technology maturing quickly, progressing towards commercial installments within the next few years, it is reasonable to assume that a kite powered system with an 80 m^2 kite will be technologically possible. A single 80 m^2 kite with the base case flight path as described in Chapter 4 produces a power density of 7.34 W/m^2. As a reference to the current state of renewable energy technology, a typical wind park power density of 1-3 W/m^2 will be considered, as well as a typical power density of solar photo voltaic installations of 5-10 W/m^2 [34]. These results show promise that kite farms can be quite competitive in the current renewable energy market with power densities of an even larger scale than those of wind farms and PV installations. For regions where space is limited, this is a great benefit, and the simpler installation process makes these kite farm systems ideal for remote or more

inaccessible locations. While economics were not addressed in this report, the results, along with research from additional studies, indicate that reasonable LCOE values should be possible since a high power is produced from few materials in a small area.

Utilizing the results of the case studies for a practical application would suggest that the ideal system to implement would be a single line kite farm designed for a predominantly wind perpendicular direction. One location of interest was selected in Curacao based upon the location's wind resource, which features high wind speeds and a single predominant wind direction. The average wind speed graph, based on historical data at an altitude of 100 meters, is shown in Figure 8.5. The average wind speed of an location is 8.35 m/s at a height of 100 meters, which is in the lower range of the typical kite altitude range, and is almost the lowest height reached with the base case flight path. This average wind speed corresponds to a reference wind speed of about 6.1 m/s at the reference height of 6 meters. However, the case study results use a reference wind speed of 7 m/s, so the power density values as applied to this location will be slightly less than those reported results. However, an above average wind site would be preferable, and this could result in a slightly higher reference wind speed. The wind rose of Curacao, based upon wind data over several weeks, is displayed in Figure 8.6. The figure verifies that the wind direction is constant or similar for the majority of the time throughout an entire year, which is greatly beneficial for a kite farm system, as a wind perpendicular layout can be created for one predominant wind direction, leading to closer spacing. At this location, the wind is directly from the east for about 50 percent of the time, and is within a 10° deviation in the other 45 percent of the time, leaving just 5 percent of the time slightly further away from directly east winds. Additionally, the wind speeds at the reference height are within the range of 6.5-9.5 m/s and directly from the east for about 42 percent of the time [35]. The wind speed range, in addition to the wind direction trend, is good for a flexible AWE system as well, since the majority of the wind speeds typically remain within the range of 7-16 m/s that produces the highest power values, as seen in Figure 2.2. There may be a slight power drop when operating at the 80° or 100° wind directions, but the azimuth shift results still showed high power density results with azimuth shifts as large as 20°. Some of the highest power density values actually resulted from systems with one or more units with a 20° azimuth shift, which could be implemented in these times of wind direction deviation from the average wind direction.

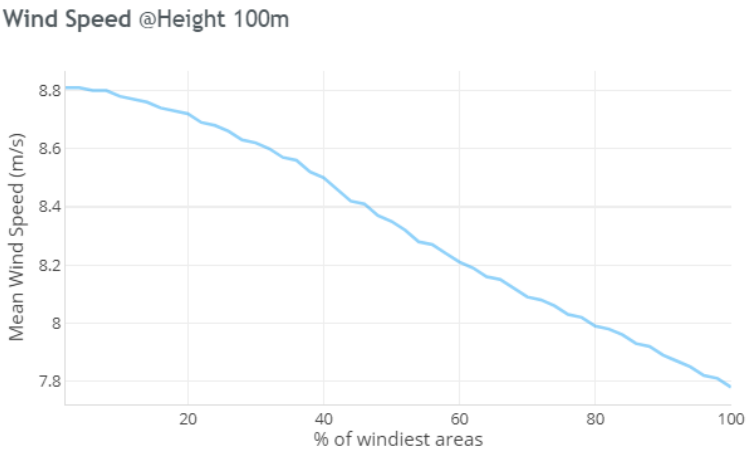

Figure 8.5: Curacao wind speeds [36]

Curacao also has typically few hours in the year in which the Kitepower system would not be able operate, so the capacity factor should be quite high, and would be dependent on the system rated power [35]. However, this excludes any operation and maintenance periods, which would ideally occur periods of sustained low wind speeds, where the kite farm would produce less energy anyways. Alternatively, this could be done during a period where wind speeds are too high and produce less power, but this is less likely at this location. For an environment with a more uniform wind rose, one would design a more triangle- or square-like kite farm layout so the power output does not change significantly with different wind directions. For locations with a predominant wind direction, such as with Curacao, the kite farm should be tailored to suit this direction, but would produce less energy

generally when wind speeds are in other directions. For small scale power needs, a kite farm of several wind aligned kites could be implemented and operated with relatively high reliability at this location. For a larger scale production, kite farms with a large amount of wind perpendicular units would be preferred, but several rows of these systems could provide a large power generation capability, with the likely benefit of improved levelization as well.

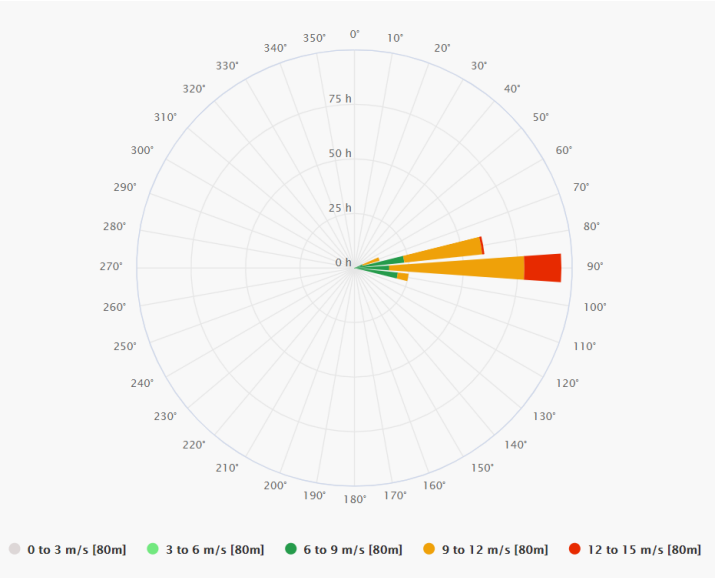

Figure 8.6: Curacao wind rose [35]

9

Conclusions and recommendations

With this thesis, several tools were developed to analyse single and multiple unit airborne wind energy generation systems. The 2D idealized kite flight path from Kitepower was expanded to a 3D model, incorporating Lissajous curves to represent the figure-eight maneuvers of an kite system in traction. This simulated path was validated with experimental data and was confirmed to improve spatial accuracy greatly as compared to the 2D simulation. The improvements in cycle duration and power matching with experimental results further confirm the improvements of the simulation. These improvements are key for accurate kite farm modeling, since the airborne location of each kite during operation affects the spacing between ground station units, and therefore the power density. With the 3D flight path, the kite farm simulation was developed, including a kite farm layout module to define the relative placement of ground station units and the angle of the wind. With the kite farm simulation, the flight path of each kite is created, and then all kites in the farm are assessed for collision or closeness to other kites throughout all points of operation. If two kites are within a certain distance of each other, a value based upon kite area, the distance between ground stations is increased until an adequate safety factor is reached.

From the results of the case studies and further simulations, it is clear that farm systems with fewer yet larger kite perform well. Wind perpendicular systems typically produce higher power density values, but if space is not a consideration, or the wind direction changes often, wind aligned or triangular systems can also perform well, especially when compared to the power densities of wind turbines. But, wind aligned systems, both with and without a phase shift, typically produced higher power density values than any of the wind aligned systems. Since the most levelized power outputs resulted from phase shifted systems, wind aligned systems with a phase shift show a decent combination of ideal farm characteristics. In summary from the case studies, a two kite farm system can produce power density values up to approximately 7.6 W/m^2 for an 80 m^2 kite, and larger kite sizes are expected to produce even higher values. This is quite competitive with the performance of currently implemented renewable energy technology, showing the technological capabilities of kite farm technology [34]. Furthermore, adding more kites increases the average cycle power, and allows for potentially improved power levelization as well. Having more phase shifted kites can better compensate for the difference in phase durations, as clearly seen between the results of the two and three kite systems. With the adjusted flight envelopes, several trends were observed. Naturally, having kites with azimuth angles facing away from each other was greatly beneficial for decreasing spacing between units, especially in the wind perpendicular orientation. Additionally, having an upwind kite elevation angle higher than that of the downwind units was similarly beneficial. It was also notable that several wind aligned systems compromised on the elevation angle, utilizing a value much greater than the optimal value, as it resulted in significantly closer spacing between units. As for tether lengths, generally the optimal power density resulted from having maximum or minimum tether lengths of the same size. Greater maximum tether lengths were usually most beneficial, while the minimum tether length had an optimal power density when its value was 300 meters, since it allows access to higher wind speeds. The minimum and maximum tether length values were also seen to most directly affect cycle durations, which can be useful in matching cycle durations of dissimilar flight paths.

With the AWE field still heavily in the research and development phases, there are many areas of

interest which can be further analyzed. As developments lead towards larger kites, additional flight data can be analyzed to further increase the accuracy of flight paths and turn rate limits for larger kites. This is crucial for kite farm analysis, because using flight paths which are too conservative can lead to low power densities and using a flight path which is not conservative enough could lead to collisions. Another area of interest would be in developing a real-time control strategy for each kite with an overall farm collision avoidance controller. This would evaluate the distance between each kite over time, as done in the simulation, but could implement avoidance maneuvers or update each kite's optimal path as needed. Another area of interest would be with incorporating wind data over time to model a realistic output of the system over a longer time period. This would be important for kite farm evaluation at each installation location, providing an estimate of the yearly production. While there is still a significant amount of research to be done before kite farms systems become commercially available, the results of this report show promise in kite farm technology and provide an initial insight into the benefits and capabilities of larger scale AWE systems.

Bibliography

[1] International Energy Agency, *World energy outlook 2017,* (2017), https://www.iea.org/weo2017/.

[2] S. Morel, *After a 3-year stagnation, CO2 emissions are on the rise again,* EnerDATA (2018), Tech. Rep.

[3] International Energy Agency, *Global energy and co2 status report 2017,* IEA (2018), Tech. Rep.

[4] C. Kost and T. Schlegl, *Studie: Stromgestehungskosten erneuerbare energien,* Fraunhofer ISE (2018), Tech. Rep.

[5] M. Diehl, *Airborne wind energy: Basic concepts and physical foundations,* in *Airborne Wind Energy*, edited by U. Ahrens, M. Diehl, R. Schmehl (Springer Verlag, Berlin Heidelberg, 2013) Chap. 1, pp. 3–21.

[6] K. Levin, *New global co2 emissions numbers are in. they're not good.* (2018), https://www.wri.org/blog/2018/12/new-global-co2-emissions-numbers-are-they-re-not-good.

[7] EIA, *Levelized cost and levelized avoided cost of new generation resources in the annual energy outlook 2018,* US Energy Information Administration (2018), Tech. Rep.

[8] S. Watson et. al., *Future emerging technologies in the wind power sector: A european perspective,* Renewable and Sustainable Energy Reviews **113** (2019).

[9] Makani, *Harnessing wind energy with kites to create renewable electricity,* (2018), https://x.company/projects/makani/.

[10] Danish Wind Industry Association, *Size of wind turbines,* (2003), http://xn–drmstrre-64ad.dk/wp-content/wind/miller/windpower%20web/en/tour/wtrb/size.htm.

[11] P. Faggiani and R. Schmehl, *Design and economics of a pumping kite wind park,* in *Airborne Wind Energy: Advances in Technology Development and Research*, edited by R. Schmehl (Springer Nature, Berlin Heidelberg, 2018) Chap. 16, pp. 391–409.

[12] K. Tweed, *World's highest wind turbine will hover above alaska,* (2014), https://spectrum.ieee.org/energywise/energy/renewables/first-commercial-floating-wind-turbine-hovers-above-alaska.

[13] P. Faggiani, *Pumping kites wind farm,* TU Delft (2014), MSc thesis.

[14] C. Grete, *Optimization, scaling and economics of pumping kite power systems,* TU Delft (2014), MSc thesis.

[15] AMPYX Power, *The sea-air-farm project,* (2018), https://www.ampyxpower.com/2018/04/far-offshore-floating-airborne-wind-energy-systems-possible-and-competitive.

[16] RVO Nederland, *Exploratory Research and LCoE of Airborne Offshore Wind Farm,* (2016), https://www.topsectorenergie.nl/tki-wind-op-zee/rd-projecten/exploratory-research-and-lcoe-airborne-offshore-wind-farm.

[17] A. Cherubini, A. Papini, R. Vertechy, and M. Fontana, *Airborne wind energy systems: A review of the technologies,* Renewable and Sustainable Energy Reviews **51**, 1461 (2015).

[18] R. Schmehl, *Airborne wind energy: Implemented concepts,* (2018), Presentation, Airborne Wind Energy course.

[19] R. van der Vlugt, A. Bley, M. Noom, and R. Schmehl, *Quasi-steady model of a pumping kite power system,* TU Delft (2017).

[20] R. Schmehl, *Airborne wind energy introduction,* (2018), Presentation, Airborne Wind Energy course.

[21] M. S. J. Venegas, *Path optimization of a pumping kite system,* TU Delft (2017), MSc thesis.

[22] Kitepower, *Tech,* (2018), https://kitepower.nl/tech/.

[23] Topsector Energie, *Far offshore floating airborne wind energy systems possible and competitive,* (2018), https://www.ampyxpower.com/2018/04/far-offshore-floating-airborne-wind-energy-systems-possible-and-competitive.

[24] F. Felker, *Makani takes to the ocean with shell,* (2019), https://blog.x.company/makani-takes-to-the-ocean-with-shell-5aa74551917a.

[25] R. Schmehl, *Kitepower concept physics of tethered flight i,* (2018), Presentation, Airborne Wind Energy course.

[26] M. Zaayer, *Wind climate and energy yield,* TU Delft (2018), Presentation, Introduction to wind turbines course.

[27] N. Hall, *Dynamic pressure,* (2015), https://www.grc.nasa.gov/www/k-12/airplane/dynpress.html.

[28] J. Shiver, *Lissajous curves,* (2003), http://jwilson.coe.uga.edu/EMT668/EMAT6680.2003.fall/Shiver/assignment10/assignment10.htm.

[29] M. van Reijen, *The turning of kites: A quantification of known theories,* TU Delft (2018), MSc thesis.

[30] J. Oehler, V. R. Marc, and R. Schmehl, *Experimental investigation of soft kite performance during turning maneuvers,* Journal of Physics: Conference Series **1037** (2018).

[31] M. Ghilardi, *Kitepower fact sheet,* Kitepower (2019), Tech. Rep.

[32] P. Bourke, *The shortest line between two lines in 3d,* (1998), http://paulbourke.net/geometry/pointlineplane/.

[33] IRENA, *Renewable energy technologies: Cost analysis series,* Renewable and Sustainable Energy Reviews **1** (2012).

[34] R. Wilson, *The future of energy: Why power density matters,* (2013), https://www.energycentral.com/c/ec/future-energy-why-power-density-matters.

[35] Meteo Blue, *Windrose curacao,* (2019), https://www.meteoblue.com/en/products/historyplus/windrose.

[36] Technical University of Denmark, *Global wind atlas 2.0,* (2017), https://globalwindatlas.info/.

A

Single kite path results

Figure A.1: Side view comparison cycle 3

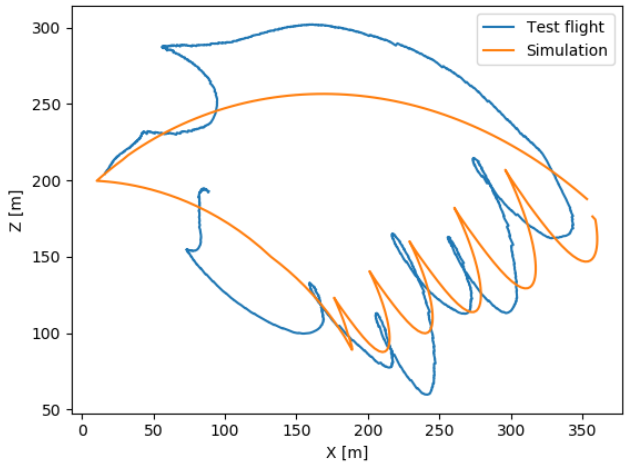

Figure A.2: Side view comparison cycle 4

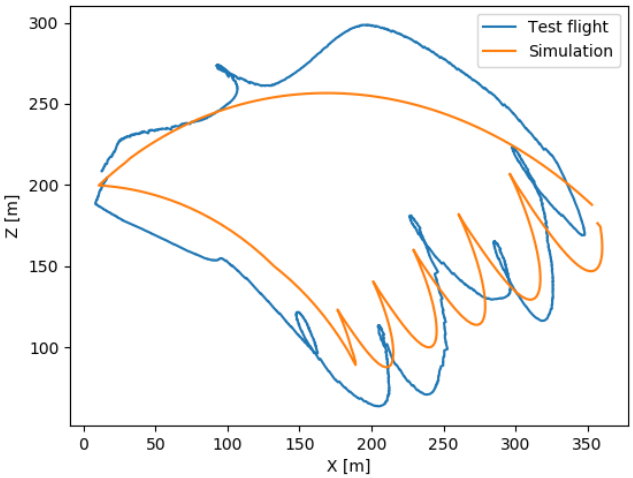

Figure A.3: Side view comparison cycle 12

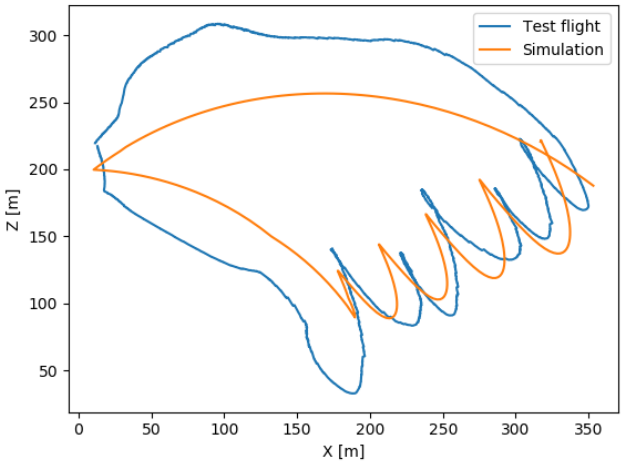

Table A.1: Force and wing loading parameters utilized for case studies

Kite size $[m^2]$	**Retraction Force** [N]	**Traction Force** [N]	**Wing Loading** $[N/m^2]$
25	1004	6736	400
40	1606	10777	500
60	2410	16166	800
80	3213	21555	800
120	4820	32332	800
150	6025	40415	800

B

Kite farm results

Table B.1: Two kite wind aligned system overview with base case parameters

Kite size $[m^2]$	**Power density** $[W/m^2]$	**Total power** [kW]	**Unit spacing** [m]	**Min. distance reached** [m]
25	1.56	14.97	100	25.38
40	2.30	25.56	125	31.72
60	3.12	39.27	150	38.07
80	3.75	52.85	175	44.42
120	4.80	79.25	215	54.57
150	5.64	99.85	255	59.65

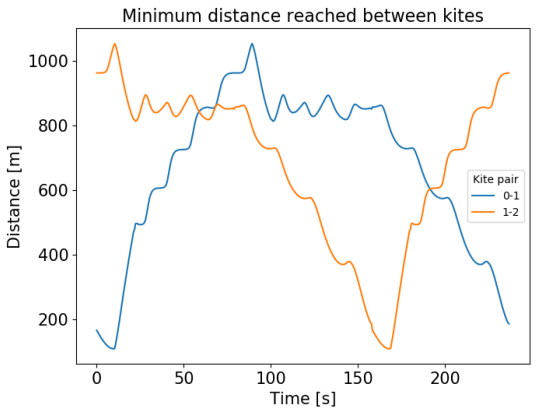

(a) Distances between kites

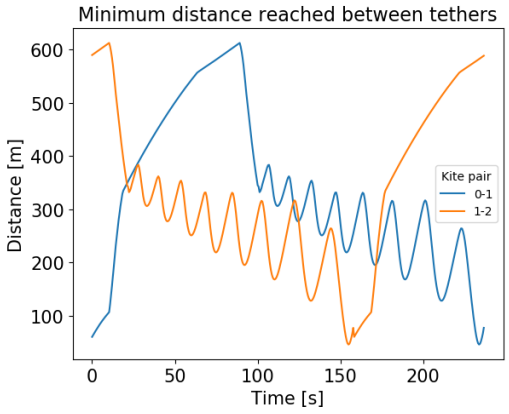

(b) Distances between tethers

Figure B.1: Three kite (wind aligned) phase shift effects on distances over one cycle

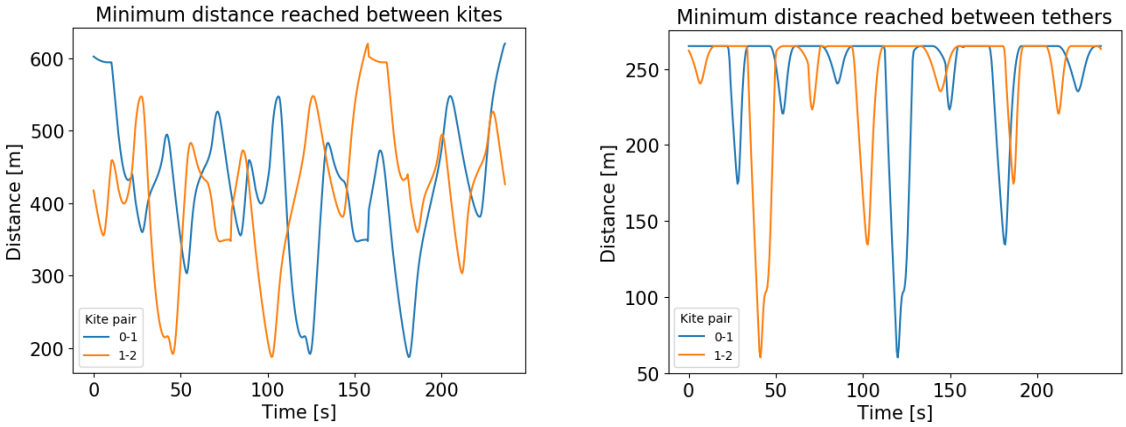

(a) Distances between kites (b) Distances between tethers

Figure B.2: Three kite (wind perpendicular) phase shift effects on distances over one cycle

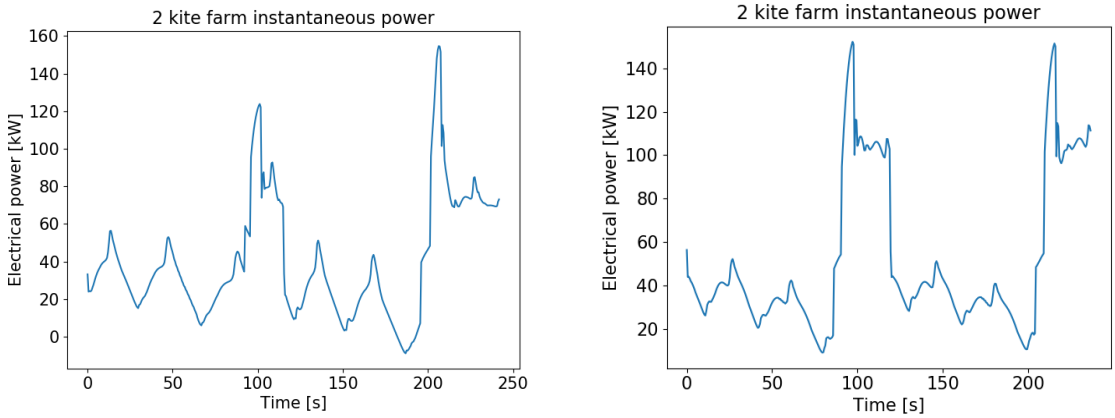

(a) Wind aligned, phase shifted (b) Wind perpendicular, phase shifted

Figure B.3: Two kite azimuth effects on instantaneous power

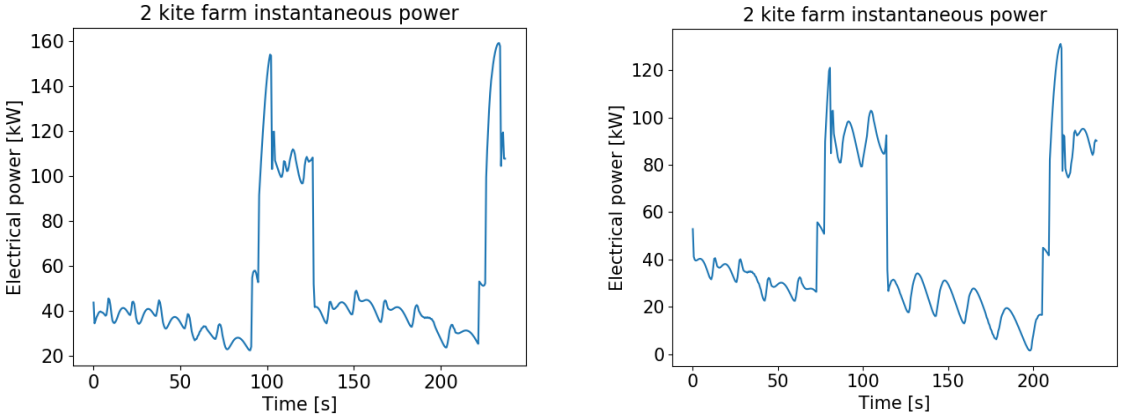

(a) Wind aligned, phase shifted (b) Wind perpendicular, phase shifted

Figure B.4: Two kite elevation effects on instantaneous power

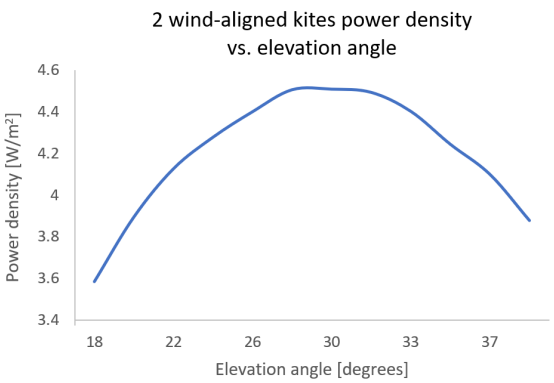

(a) No phase shift

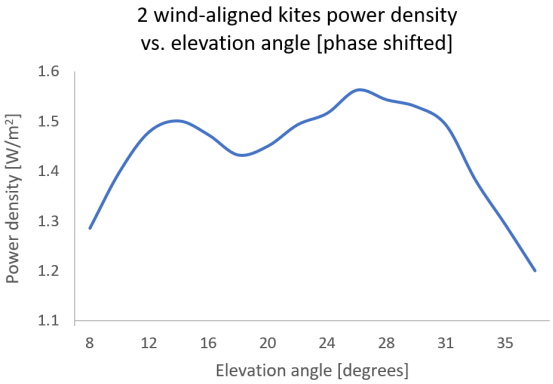

(b) Phase shifted system

Figure B.5: Wind aligned similar envelope elevation effects

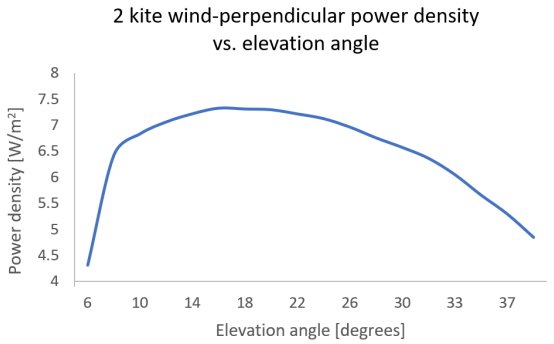

(a) No phase shift

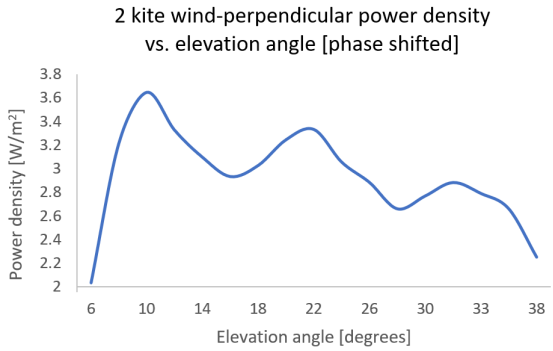

(b) Phase shifted system

Figure B.6: Wind perpendicular similar envelope elevation effects

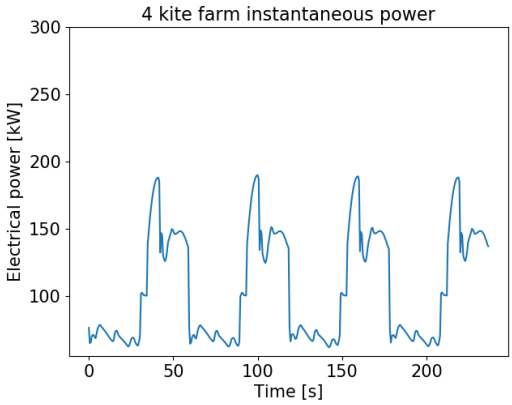

(a) 4 wind perpendicular kite farm

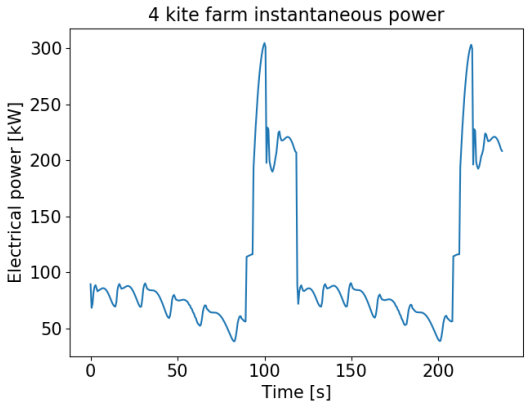

(b) 4 kite square farm

Figure B.7: 4 kite phase shift results

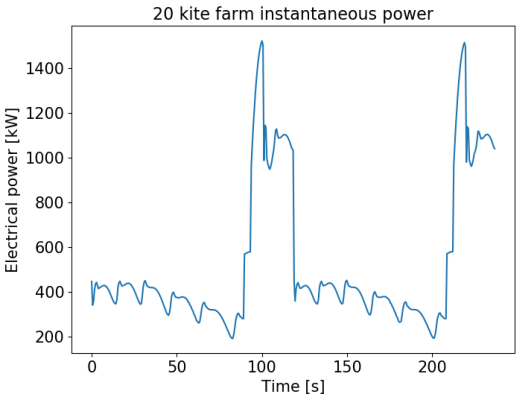

Figure B.8: 20 kite farm (2 wind aligned) with phase shift

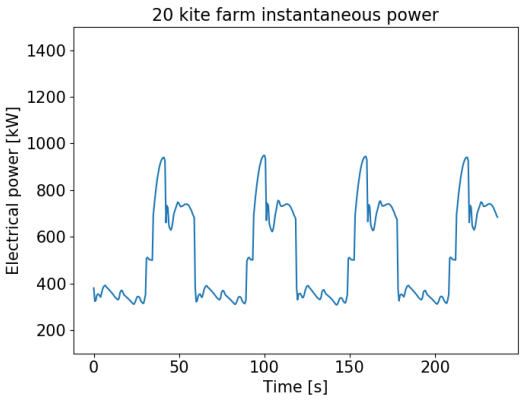

Figure B.9: 20 kite farm (4 wind aligned) with phase shift

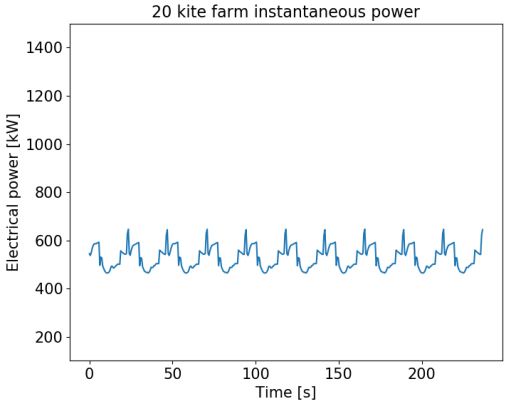

Figure B.10: 20 kite (10 wind aligned) farm with phase shift

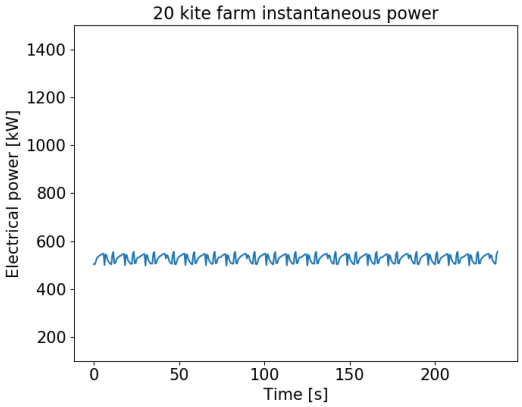

Figure B.11: 20 kite (20 wind aligned) farm with phase shift

Table B.2: Four kite square system overview with 7 m/s wind

Kite size [m^2]	**Power Density** [W/m^2]	**Total Power** [kW]	**X spacing** [m]	**Y spacing** [m]	**Min. distance reached** [m]
25	2.05	25.28	70	35	27.97
40	2.90	42.02	85	40	33.30
60	3.45	62.57	105	50	40.44
80	3.90	84.16	120	60	45.67
120	4.50	122.85	150	70	56.14
150	5.10	153.21	165	80	61.19

Table B.3: 20 kite system (4 columns wind aligned) overview with 7 m/s wind

Kite size $[m^2]$	**Power Density** $[W/m^2]$	**Total Power** [kW]	**X spacing** [m]	**Y spacing** [m]	**Min. distance reached** [m]
25	2.25	126.42	70	35	27.97
40	2.92	210.12	85	40	33.30
60	3.10	312.83	105	50	40.44
80	3.25	420.79	120	60	45.67
120	3.45	614.25	150	70	56.14
150	3.55	766.06	165	80	61.19